DYNAMICS AND STRUCTURE: FROM MICROTUBULE NETWORKS TO POPULATION NETWORKS

by

Heather Brooks

A dissertation submitted to the faculty of
The University of Utah
in partial fulfillment of the requirements for the degree of

Doctor of Philosophy

Department of Mathematics

The University of Utah

May 2018

The University of Utah Graduate School

STATEMENT OF DISSERTATION APPROVAL

The dissertation of **Heather Brooks**
has been approved by the following supervisory committee members:

Paul Bressloff ,	Chair(s)	**21 Feb 2018** Date Approved
James Keener ,	Member	**21 Feb 2018** Date Approved
Frederick Adler ,	Member	**21 Feb 2018** Date Approved
Sean Lawley ,	Member	**23 Feb 2018** Date Approved
Nina Fefferman ,	Member	**21 Feb 2018** Date Approved

by **Davar Khoshnevisan** , Chair/Dean of
the Department/College/School of **Mathematics**
and by **David B. Kieda** , Dean of The Graduate School.

ABSTRACT

The interplay of dynamics and structure is a common theme in both mathematics and biology. In this thesis, the author develops and analyzes mathematical models that give insight into the dynamics and structure of a variety of biological applications. The author presents a variety of contributions in applications of mathematics to explore biological systems across several scales. First, she analyzes pattern formation in a partial differential equation model based on two interacting proteins that are undergoing passive and active transport, respectively. This work is inspired by a longstanding problem in identifying a biophysical mechanism for the control of synaptic density in *C. elegans* and leads to a novel mathematical formulation of Turing-type patterns in intracellular transport. The author also demonstrates the persistence of these patterns on growing domains, and discusses extensions for a two-dimensional model. She then presents two models that explore how stochastic processes affect intracellular dynamics. First, the author and her collaborators derive effective stochastic differential equations that describe intermittent virus trafficking. Next, she shows how ion channel fluctuations lead to subthreshold oscillations in neuron models. In the final chapter, she discusses two projects for ongoing and future work: one on modeling parasite infection on dynamic social networks, and another on the bifurcation structure of localized patterns on lattices. All of these projects, presented together, chronicle the journey of the author through her mathematical development and attempts to identify, discover, create, and communicate mathematics that inspires and excites.

For all the women who inspire me and will continue to inspire me - past, present, and future

CONTENTS

ABSTRACT . . . . . **iii**

ACKNOWLEDGMENTS . . . . . **vii**

CHAPTERS

1. OVERVIEW OF THE THESIS **1**

1.1 Motivation 1
1.2 The problems 2
1.3 References 8

2. A MECHANISM FOR TURING PATTERN FORMATION WITH ACTIVE AND PASSIVE TRANSPORT **11**

2.1 Introduction 12
2.2 Three-component trafficking model 14
2.3 Conditions for Turing instability in trafficking model 16
2.3.1 Linear stability analysis 17
2.3.2 Dispersion curves 20
2.3.2.1 Parameter values 21
2.3.3 The reaction-diffusion limit 22
2.4 Biased active transport 25
2.5 Discussion 27
2.6 References 30

3. A TURING MECHANISM FOR HOMEOSTATIC CONTROL OF SYNAPSE DENSITY DURING *C. ELEGANS* GROWTH **33**

3.1 Introduction 34
3.2 Model 34
3.3 Pattern formation on a growing domain 36
3.4 Discussion 37
3.5 References 38

4. MATHEMATICAL ANALYSIS OF PATTERN FORMATION IN REACTION-TRANSPORT MECHANISMS **39**

4.1 Weakly nonlinear analysis for the one-dimensional reaction-transport mechanism 39
4.1.1 The one-dimensional model 39
4.1.2 Weakly nonlinear stability analysis 40
4.2 Pattern formation in two dimensions 46
4.2.1 The model 47
4.2.2 Future work: bifurcation analysis of two dimensional pattern formation 48

4.3 References 49

5. COARSE-GRAINING INTERMITTENT INTRACELLULAR TRANSPORT: TWO- AND THREE-DIMENSIONAL MODELS 50

5.1 Introduction 51
5.2 Two-dimensional cell – disk 51
5.2.1 Previous coarse-grained dynamics by Lagache and Holcman 52
5.2.2 New coarse-grained dynamics 53
5.2.3 Comparison 53
5.3 General method 53
5.4 Three-dimensional cell – sphere 54
5.4.1 Coarse-grained spherical dynamics 55
5.4.2 Comparison 56
5.5 Three-dimensional cell – cylinder 56
5.5.1 Coarse-grained cylindrical dynamics 57
5.5.2 Comparison 57
5.6 Summary and conclusions 57
5.7 Acknowledgments 58
5.8 References 58

6. QUASICYCLES IN THE STOCHASTIC HYBRID MORRIS-LECAR NEURAL MODEL 59

6.1 Introduction 60
6.2 Deterministic model 61
6.3 Stochastic model 62
6.4 System-size expansion of potassium 62
6.5 Quasi-steady-state diffusion approximation of sodium 64
6.6 Quasicycles in the stochastic model 65
6.7 Discussion 67
6.8 Acknowledgments 67
6.9 References 67

7. FUTURE DIRECTIONS 69

7.1 Parasite spread on dynamic social networks 69
7.1.1 Proposed problems for future work 76
7.2 Localized patterns on lattices 79
7.2.1 Proposed problems for future work 80
7.3 References 83

ACKNOWLEDGMENTS

All of the projects presented in this thesis exist because of hard work and discussions with amazing collaborators. I appreciate each of you and the richness you have brought to both my mathematics and my life. In particular, I am eternally grateful to my advisor, Paul Bressloff, for taking me as a student. You gave me freedom when I needed it and pushed me when I needed it. Most importantly, you've given me confidence when I needed it. I have become the mathematician I am today because of you.

I would like to express my deep appreciation for the members of my committee. They were each specially chosen because they played a critical role in various points in my graduate career. First, Fred Adler, who is responsible for introducing me to the Hodgkin-Huxley equations and mathematical biology. He was the first person to show me the exciting and creative nature of mathematics. Jim Keener has been an understanding and helpful leader of our mathematical biology group. Right after my first qualifying exam, when I was very stressed out, he convinced me that everything was going to be fine (yes, Dr. Keener, you were right!). I am grateful to Sean Lawley for convincing me in my third year that intracellular transport is cool, and for being a great example as an early career mathematician. Finally, Nina Fefferman has been a phenomenal mentor for me during the last year of graduate school. I met her at a time when I was really struggling, and she (unknowingly) convinced me that I could in fact be a successful research mathematician.

I have been so fortunate to have an amazing group of friends to help me through graduate school, both in and out of the math department. Thank you to James Brinkmann; your longtime friendship is absolutely foundational for my life. Kathy McNamara, thank you for keeping it real and making life fun. Thanks to my office mates Jenna Noll, Samantha Hill, and Hallie Elich for all the cups of tea and good conversation we shared. The strong community of women mathematicians I have been surrounded with has been a lifesaver. You're all so fierce. Girls' Brunch forever. Finally, I have to give a special shoutout to the two people that really defined my time in grad school. The first is Derrick Wigglesworth,

my constant lunch buddy and loyal friend. I still hope that we can find a way to write a paper together someday. The second is my soul sister Anna Romanov. Together we dreamt big, fought hard, and had a great time doing it. I think we will probably take over the world. Derrick and Anna, I'm so honored that I get to graduate with you and so lucky I got to do grad school alongside you.

There is no community more supportive than the University of Utah mathematical biology group, and I will always be grateful to have been a part of that. In particular, a special thanks to my academic siblings Bhargav Karamched, Bin Xu, Sam Carroll, Ethan Levien, Bridget Fan, Patrick Murphy, and our adopted brother Chris Miles for all of the feedback, advice, and friendship you've given me throughout the years.

My family has been incredibly supportive since day one, and they deserve all of the credit for teaching me how to work hard and play hard. I acknowledge my parents, Marci and Randall Brooks, for always encouraging me to chase my dreams and try hard things. To the world's greatest siblings, Iris, Rosemary, and John - life would be way less fun without you in it. I hope I make you all as proud as you make me.

Last, but far from least, I want to thank my husband Leif Zinn-Björkman. You have always believed in me, and you are the kindest and most generous partner I could ever ask for. I love you!

CHAPTER 1

OVERVIEW OF THE THESIS

This thesis and the work contained within is a reflection of two pieces of advice that I received during my graduate studies in math. The first came to me at the very beginning of my Ph.D. program from Paul Bressloff, the man who would eventually become my thesis advisor. He advised me that if I wanted to be successful in academia, the most important thing for me to do was work on problems that I was intrinsically driven and excited by. If and when Paul complains that my thesis has too many different pieces of work, I like to remind him that it's a direct result of this advice. During my years as a graduate student, I have been fortunate to encounter a variety of mathematics that has delighted me, and I am grateful that I was given the space to pursue all of these questions.

This year, as I was finishing up my Ph.D., I received a complementary piece of advice from my mentor and collaborator Nina Fefferman. Nina told me - or perhaps, reminded me - that when communicating your work, it is important to identify what it is that motivates you. These two pieces of advice sum up what this thesis represents: a journey to identify, discover, create, and communicate mathematics that inspires and excites me.

1.1 Motivation

I still vividly remember the first mathematical model I saw that really inspired me. It was the Hodgkin-Huxley equations, which are a system of differential equations that model the dynamics of ion channels and membrane potential of a neuron [8]. I was struck by the fact that, while neural dynamics are complicated, the mathematics was not. This model pointed to a profound concept – that neurons are subject to the same underlying physical principles as circuits, and mathematics is the language by which we can analyze these general physical principles. I decided I wanted to become a mathematician when I encountered models with this theme again and again in biological applications as diverse as the synchrony of fireflies (as presented in [22]) and pattern formation in

reaction-diffusion systems [23].

What has become clear to me during my mathematical development is that I am particularly motivated by problems where an underlying spatial structure contributes to the self-organization of a given system. This interest was originally born from a delight in beautiful patterns, but has developed into a desire to understand how the underlying interplay of structure and movement creates self-organization – often in surprising ways. During my graduate work, I have primarily pursued problems in biological applications because these systems are a fruitful source of inspiration where these mathematical motifs arise again and again, and in turn they lead to the development of new mathematics.

In this thesis, I present a variety of my contributions in applications of mathematics to explore the dynamics and structure of biological systems across several scales. On the molecular level, we use stochastic hybrid systems to understand the dynamics of ion channel fluctuations (Chapter 6). On the cellular level, we use linear and weakly nonlinear analysis on systems of partial differential equations to understand pattern formation (Chapters 2, 3, and 4) and derive stochastic differential equations for virus trafficking (Chapter 5). Finally, in Chapter 7, we look at how network structure affects the dynamics of parasite spread on the population level.

1.2 The problems

In this section, I outline the structure of this thesis chapter-by-chapter, explaining my personal motivation for each problem along the way.

In **Chapter 2,** we analyze pattern formation in a partial differential equation model based on two interacting proteins that are undergoing passive and active transport, respectively. I start with this project because it is the largest (in terms of page length and content) and longest (in terms of time I spent working on it). This work is motivated by a longstanding problem in identifying a biophysical mechanism for the control of synaptic density in *C. elegans* [19] and leads to a novel mathematical formulation of Turing-type patterns in intracellular transport [3]. This problem was exciting to me because Turing mechanisms provide an elegant biophysical explanation for the spatial organization of interacting particles, but existence of these pattern formation mechanisms has gone largely unexplored in the context of intracellular transport.

While the primary results are mathematical, the original inspiration for this problem is biological. The dynamical processes underlying the establishment of synaptic connections during neural development are thought to be critical in learning and memory. Since the proteins and transport mechanisms that regulate synaptic development are conserved across multiple species, considerable insights can be obtained by studying simpler organisms such as the nematode worm *Caenorhabditis elegans* (abbreviated *C. elegans*). During development, the density of synapses containing the glutamate receptor GLR-1 is maintained despite significant changes in length [19]. It is known that this maintenance also requires the protein kinase CaMKII, which regulates the active transport and delivery of GLR-1 to synapses [9, 10, 19]. However, a long outstanding problem has been identifying a possible physical mechanism involving diffusing CaMKII molecules and motor-driven GLR-1 that leads to the control of synaptic density [19]. Although the above problem arises within the context of neural development, it raises a more general issue regarding self-organization in systems of actively and passively transported particles. That is, the formation of a regularly spaced distribution of synapses at an early stage of development is suggestive of some form of Turing-like pattern formation. The traditional mechanism for spontaneous pattern formation due to Turing [23] is the interaction of two or more passively diffusing chemical species undergoing nonlinear reaction kinetics and having different rates of diffusion [13, 17]. In joint work with Paul Bressloff, I propose an alternative pattern-forming mechanism [3], involving the interaction between a slowly diffusing species (*e.g.*, CaMKII) and a rapidly advecting species (*e.g.*, GLR-1) switching between anterograde and retrograde motor-driven transport (bidirectional transport).

To investigate the proposed pattern formation mechanism, we develop a model of three partial differential equations on a one-dimensional domain with no flux boundary conditions. Our main results are as follows:

1. Using linear stability analysis, we derive the conditions for the emergence of patterns on a one-dimensional domain of fixed length. This allows us to derive analytic conditions on the parameter γ, which is the ratio of switching rate and diffusion coefficient to active transport velocity. We find an expression for the critical value of γ, below which instabilities arise. This is analogous to the previous results obtained in reaction-diffusion equations, where pattern formation requires fast (long-range)

inhibition.

2. Pattern formation arises outside of the fast switching parameter regime, that is, when bidirectional switching rate $\alpha = \mathcal{O}(\epsilon^{-1})$. It would be natural to suppose that patterns arise in this transport mechanism because the bidirectional switching in some sense "acts like" diffusion. However, this is not the case: in the adiabatic limit, this system reduces to a reaction-diffusion equation that does not satisfy the necessary conditions for pattern formation.

3. This pattern formation mechanism is robust to asymmetries in transport velocities. We have derived analytical conditions under which the biased version of our model supports patterns that persist in time.

With biologically relevant parameter values, our model produces ~ 4 evenly distributed peaks of GLR-1 in a 10 μm segment of ventral cord, which matches what is observed in the *in vivo* data for a ventral cord of fixed length.

Chapter 3 is a natural extension of Chapter 2. According to the observations in [19], synapse density is established early in larval development and is maintained as the worm grows. Thus, in order to convincingly apply our pattern formation model to the *C. elegans* system, we need to show that patterns can be maintained on a growing domain. In this chapter, we show that if the domain grows isotropically, this system can continue to self-organize and new synapses can be inserted to maintain patterns. Following the work of Crampin et al. [5], we derive evolution equations for the growing domain by rewriting spatial position using a Lagrangian coordinate description and applying Reynold's transport theorem. Under this transformation, the domain growth can be interpreted as time-dependent diffusion and velocity coefficients, representing dilution and local flow. In this formulation, we then show that this mechanism supports synapse insertion on the growing domain.

In **Chapter 4**, we present additional mathematical extensions of pattern formation in the reaction-transport model. Linear stability analysis allows us to derive conditions to understand when and how patterns arise in a particular system, but it does not give us any information about the selection and stability of these patterns. These features are determined by the nonlinearities of the system. In order to investigate the stability of the

periodic patterns that arise in the one-dimensional model, we perform a weakly nonlinear stability analysis. Using the method of multiple scales, we derive an amplitude equation to describe the slow timescale evolution of patterns. It is important to note that, since patterns do not arise in the fast switching limit, this analysis must be applied to the full model. In the second part of this chapter, I present the future work for this project, which involves developing a two-dimensional version of the reaction-transport model and performing bifurcation analysis on the resulting model. In the two-dimensional case, the underlying microtubule network structure will affect the resulting pattern dynamics.

Thinking about how the structure of microtubule networks influences intracellular transport leads us naturally to **Chapter 5**, in which I present a stochastic model of intracellular transport of viruses. The motivation for me to undertake this project was to explore the interesting dynamics introduced to intracellular transport by random switching. As a result of this randomness, careful mathematical analysis is required to capture how domain geometry affects stochastic processes.

Cells rely on their transport structures to ensure proper cell function. However, these transport mechanisms can also be exploited by viruses. Viruses lack cellular structure and metabolism, and thus are unable to replicate themselves; they rely on the infrastructure of infected host cells for this purpose. In order for a virus to replicate itself successfully within its host, it needs to navigate to the cell's nucleus, all without any of its own locomotion mechanisms [6]. Single particle tracking experiments [1, 20] show that viral motion alternates between passive diffusion in the cytosol and ballistic transport along microtubules. This erratic, alternating motion behavior makes quantitative analysis difficult.

Most of the existing mathematical work on this topic takes an effective stochastic differential equation as a starting point for study of these processes [11, 14]. There exists a previous reduction of the full process to a stochastic differential equation (SDE) due to Lagache and Holcman [15], but this method is only applicable for two-dimensional cell geometries. Furthermore, their method captures only the mean first passage time for the virus to reach the nucleus and not the mean first passage time distribution.

In this work, joint with Sean Lawley and Marie Tuft, we develop a method to derive an effective SDE that encapsulates the switching transport dynamics and captures several important features of the associated probability distributions when compared to Monte

Carlo simulations of the full process for an illustration of this process cell modeled by a two-dimensional disk. In order to write down an SDE with the correct drift and diffusion coefficients, we need to know the probability that the virus is on a microtubule given its radial position. By partitioning (or 'coarse-graining') the space between the microtubules and approximating diffusion as a Markov jump process on this partition, we are able to use the adiabatic limit to approximate the proportion of time spent on a microtubule.

Our primary results are as follows:

1. Our effective SDE matches the empirical first passage time distributions generated by numerical simulations of the full intermittent process. This is in contrast to previous work by other groups, which only matched mean first passage times. We also show that the distribution of viral position x at various times t corresponds well with the full process for all geometries that we explored.

2. Due to the generality, our coarse-graining method can be applied to a variety of cell geometries. In particular, we have derived an effective SDE for virus trafficking in a three-dimensional spherical cell as well as a three-dimensional cylindrical cell, in addition to the two-dimensional disk model described above.

In **Chapter 6**, I present another problem where random fluctuations affect the dynamics of the biological system – this time, on the molecular scale. In this work, we look at the effects of stochastic ion channel fluctuations on subthreshold voltage oscillations in neurons [2]. Intrinsic noise arising from the stochastic opening and closing of voltage-gated ion channels has been shown experimentally and mathematically to have important effects on a neuron's function. Study of classical neuron models with stochastic ion channels is becoming increasingly important, especially in understanding a cell's ability to produce subthreshold oscillations and a response to weak periodic stimuli. While it is known that stochastic models can produce oscillations (quasicycles) in parameter regimes where the corresponding deterministic model has only a stable fixed point, little work has been done previously to explore these connections to channel noise. Using a stochastic hybrid Morris-Lecar model [16, 21, 12, 18], we combined a system size expansion in potassium ions (K^+) and a quasi-steady-state diffusion approximation in persistent sodium (Na^+) in order to derive an effective SDE. By determining the corresponding power spectrum,

we establish that noise significantly extends the parameter regime in which subthreshold oscillations occur. Moreover, we found that under physiological conditions, the major contributor to the existence of quasicycles is persistent sodium channel noise.

Finally, I present two projects in **Chapter 7** that are currently in development: one that explores dynamics and structure in a new biological application, and one that formalizes new mathematics for patterns on lattices. First, I discuss a collaborative project with Nina Fefferman, Maryann Hohn, Candice Price, Ami Radunskaya, Suzanne Sindi, Nakeya Williams, and Shelby Wilson, where we examine dynamics and structure on the population level; in particular, we examine how parasites alter the optimal social strategies for a population's evolutionary fitness. A population's evolutionary fitness is inherently tied to its social structure. On one hand, social animals experience group fitness benefits such as predator protection or increased ability to locate resources. However, due to close contact, these social groups may be more susceptible to infection from pathogens or parasites. Previous work has shown that different social systems yield different epidemic burdens for pathogens, which raises the interesting question of whether pathogen spread is a result of complex social network structure or whether such structures evolved to mitigate the effects of pathogens [7]. Prior to the work of this collaboration group, no such studies have examined the results of parasite infection in dynamic social networks, despite the fact that parasite transmission and infection is deeply intertwined with social behaviors like allogrooming.

We will develop an agent-based simulation of a dynamic social network which organizes according to various social metrics. In particular, we focus on networks that self-organize based on degree (the number of nodes to which a node is connected), closeness (a measure of the average path length between nodes), and betweenness (the percentage of shortest paths from one node in the network to another node). We will use these simulations to explore how pathogen spread differs on networks for each particular measure. This agent-based model also allows us to explore how system parameters such as parasite reproduction and grooming effectiveness alter the infection burden of the population, and whether certain individuals are more influential in determining population risk because of their social standing.

In addition to working toward an agent-based model, we have developed a model of

ordinary differential equations to represent parasite infection load in a population. By subdividing the population into individuals that are infected and uninfected by parasites, we can analyze the steady-state behaviors and gain insight into the influence of model parameters such as grooming efficiency and individual fitness. Preliminary results in this continuous deterministic model suggest that a hub-periphery network structure may be beneficial in allowing a population to mitigate parasite infection.

In the second portion of Chapter 7, I discuss a set of proposed problems on bifurcations of localized patterns. This project is joint work with Jason Bramburger and Björn Sandstede, and will advance the study of applied dynamical systems through investigation of localized patterns on lattices. This project builds off of my previous analysis of pattern formation in biological systems (for example [2, 3, 4]) to develop a more rigorous general theory of pattern formation. First, we will prove the existence of snaking bifurcations (and thus localized patterns) in the analog of the Swift-Hohenberg equation on a one-dimensional lattice with no spatial coupling, and then extend this proof to the case of general one-dimensional lattice maps that exhibit snaking. We then seek to investigate the structure of bifurcation diagrams of localized patterns on two-dimensional lattices, where a greater variety of patterns are possible and depend on the underlying symmetries of the lattice. These problems provide opportunities for mastery of new bifurcation theory techniques and will help me further my understanding of the effects of spatial coupling on localized patterns in a variety of physical systems.

1.3 References

[1] N. Arhel, A. Genovesio, K.-A. Kim, S. Miko, E. Perret, J.-C. Olivo-Marin, S. Shorte, and P. Charneau, *Quantitative four-dimensional tracking of cytoplasmic and nuclear HIV-1 complexes*, Nat. Methods, 3 (2006), p. 817.

[2] H. A. Brooks and P. C. Bressloff, *Quasicycles in the stochastic hybrid Morris-Lecar neural model*, Phys. Rev. E, 92 (2015), p. 012704.

[3] ——, *A mechanism for Turing pattern formation with active and passive transport*, SIAM J. Appl. Dyn. Syst., 15 (2016), pp. 1823–1843.

[4] ——, *Turing mechanism for homeostatic control of synaptic density during C. elegans growth*, Phys. Rev. E, 96 (2017), p. 012413.

[5] E. J. Crampin, E. A. Gaffney, and P. K. Maini, *Reaction and diffusion on growing domains: Scenarios for robust pattern formation*, Bull. Math. Biol., 61 (1999), pp. 1093–1120.

[6] K. Döhner, C.-H. Nagel, and B. Sodeik, *Viral stop-and-go along microtubules: Taking a ride with dynein and kinesins*, Trends Microbiol., 13 (2005), pp. 320–327.

[7] K. Hock and N. H. Fefferman, *Social organization patterns can lower disease risk without associated disease avoidance or immunity*, Ecol. Complex., 12 (2012), pp. 34–42.

[8] A. L. Hodgkin and A. F. Huxley, *A quantitative description of membrane current and its application to conduction and excitation in nerve*, J. Physiol., 117 (1952), pp. 500–544.

[9] F. J. Hoerndli, D. A. Maxfield, P. J. Brockie, J. E. Mellem, E. Jensen, R. Wang, D. M. Madsen, and A. V. Maricq, *Kinesin-1 regulates synaptic strength by mediating the delivery, removal, and redistribution of AMPA receptors*, Neuron, 80 (2013), pp. 1421–1437.

[10] F. J. Hoerndli, R. Wang, J. E. Mellem, A. Kallarackal, P. J. Brockie, C. Thacker, D. M. Madsen, and A. V. Maricq, *Neuronal activity and CaMKII regulate kinesin-mediated transport of synaptic AMPARs*, Neuron, 86 (2015), pp. 457–474.

[11] D. Holcman, *Modeling DNA and virus trafficking in the cell cytoplasm*, J. Stat. Phys., 127 (2007), pp. 471–494.

[12] J. P. Keener and J. M. Newby, *Perturbation analysis of spontaneous action potential initiation by stochastic ion channels*, Phys. Rev. E, 84 (2011), p. 011918.

[13] A. Koch and H. Meinhardt, *Biological pattern formation: From basic mechanisms to complex structures*, Rev. Modern Phys., 66 (1994), p. 1481.

[14] T. Lagache, E. Dauty, and D. Holcman, *Quantitative analysis of virus and plasmid trafficking in cells*, Phys. Rev. E, 79 (2009), p. 011921.

[15] T. Lagache and D. Holcman, *Effective motion of a virus trafficking inside a biological cell*, SIAM J. Appl. Math., 68 (2008), pp. 1146–1167.

[16] C. Morris and H. Lecar, *Voltage oscillations in the barnacle giant muscle fiber*, Biophys. J., 35 (1981), pp. 193–213.

[17] J. D. Murray, *Mathematical Biology II. Spatial Models and Biomedical Applications*, vol. 18, Springer-Verlag New York Incorporated, 2001.

[18] J. M. Newby, P. C. Bressloff, and J. P. Keener, *Breakdown of fast-slow analysis in an excitable system with channel noise*, Phys. Rev. Lett., 111 (2013), p. 128101.

[19] C. Rongo and J. M. Kaplan, *CaMKII regulates the density of central glutamatergic synapses in vivo*, Nature, 402 (1999), p. 195.

[20] G. Seisenberger, M. U. Ried, T. Endress, H. Büning, M. Hallek, and C. Bräuchle, *Real-time single-molecule imaging of the infection pathway of an adeno-associated virus*, Science, 294 (2001), pp. 1929–1932.

[21] G. D. Smith, *Modeling the stochastic gating of ion channels*, in Computational Cell Biology, Springer, 2002, pp. 285–319.

[22] S. H. Strogatz, *Nonlinear dynamics and chaos: With applications to physics, biology, chemistry, and engineering*, Hachette UK, 2014.

[23] A. M. Turing, *The chemical basis of morphogenesis*, Philos. Trans. R. Soc. Lond. B Biol. Sci., 237 (1952), pp. 37–72.

CHAPTER 2

A MECHANISM FOR TURING PATTERN FORMATION WITH ACTIVE AND PASSIVE TRANSPORT

The article in this chapter was originally published in the SIAM Journal of Applied Dynamical Systems, Vol. 15, No. 4, pp 1823-1843.

SIAM J. Applied Dynamical Systems
Vol. 15, No. 4, pp. 1823–1843

A Mechanism for Turing Pattern Formation with Active and Passive Transport*

Heather A. Brooks† and Paul C. Bressloff†

Abstract. We propose a novel mechanism for Turing pattern formation that provides a possible explanation for the regular spacing of synaptic puncta along the ventral cord of *C. elegans* during development. The model consists of two interacting chemical species, where one is passively diffusing and the other is actively trafficked by molecular motors. We identify the former as the kinase CaMKII and the latter as the glutamate receptor GLR-1. We focus on a one-dimensional model in which the motor-driven chemical switches between forward and backward moving states with identical speeds. We use linear stability analysis to derive conditions on the associated nonlinear interaction functions for which a Turing instability can occur. We find that the dimensionless quantity $\gamma = \alpha d/v^2$ has to be sufficiently small for patterns to emerge, where α is the switching rate between motor states, v is the motor speed, and d is the passive diffusion coefficient. One consequence is that patterns emerge outside the parameter regime of fast switching where the model effectively reduces to a two-component reaction-diffusion system. Numerical simulations of the model using experimentally based parameter values generates patterns with a wavelength consistent with the synaptic spacing found in *C. elegans*. Finally, in the case of biased transport, we show that the system supports spatially periodic patterns in the presence of boundary forcing, analogous to flow distributed structures in reaction-diffusion-advection systems. Such forcing could represent the insertion of new motor-bound GLR-1 from the soma of ventral cord neurons.

Key words. pattern formation, Turing instability, motor-driven transport, switching dynamical systems, diffusion

AMS subject classifications. 92C15, 92C37, 92C20

DOI. 10.1137/16M1061205

1. Introduction.

Pattern formation and symmetry breaking is a question of great theoretical and experimental interest. While the study of morphogenesis has a rich history, perhaps the most well-known contribution is the 1952 paper of Alan Turing [34]. In this classical work, Turing suggested two necessary parts of pattern formation: two (or more) interacting chemical species, with different rates of diffusion for the participating species. Turing derived conditions such that the combination of nonlinear reaction kinetics and diffusion can lead to instability of the homogeneous steady state. These instabilities are known as Turing patterns. Gierer and Meinhardt [8] highlighted one important general example where these conditions hold, namely, that the system involves a short-range activator and a long-range inhibitor. Turing patterns in reaction-diffusion equations are well understood and have been studied in a variety of contexts, including biology, chemistry, and physics [20].

*Received by the editors February 12, 2016; accepted for publication (in revised form) by V. Sneyd August 19, 2016; published electronically October 6, 2016.
http://www.siam.org/journals/siads/15-4/M106120.html
Funding: The work of the first author was supported by National Science Foundation grant RTG-1148230. The work of the second author was supported by National Science Foundation grant DMS-1120327.

†Department of Mathematics, University of Utah, Salt Lake City, UT 84112-0090 (heather@math.utah.edu, bressloff@math.utah.edu).

While interest in Turing pattern formation was initially primarily theoretical, there is an ever expanding literature on applications and extensions. Reaction-diffusion mechanisms have been implicated in the development of feather patterns, vertebrate skin patterns, seashells [17], and zebrafish stripes [36], as well as limb development [1] and ocular dominance stripes [33]. In addition, there have been many efforts to expand the understanding of conditions beyond the traditional reaction-diffusion paradigm under which patterns may form. To give a few examples, Turing-type patterns have been shown to form on growing domains [5], via a signal transduction mechanism [25], and via mechanical instability [10]. In this paper, we further extend this literature by proposing a novel mechanism for Turing pattern formation, which is driven by two interacting chemical species, where one is passively diffusing and the other is being actively trafficked by molecular motors.

The biological motivation underlying our proposed active trafficking mechanism for Turing pattern formation comes from cellular biology, in particular, the observation that there is a regularly spaced distribution of ventral cord and dorsal cord synapses in *Caenorhabditis elegans*, as illustrated in Figure 1. There is growing experimental evidence that synaptogenesis involves the regulation of the active (kinesin-based) transport and delivery of glutamate receptors (GLR-1) to synapses by type II calcium- and calmodulin-dependent protein kinase (CaMKII) [26, 11, 12]; see Figure 2. First, the activation (autophosphorylation) of CaMKII via voltage-gated calcium channels induces the formation of new synapses by enhancing the active transport and delivery of GLR-1 to developing synaptic sites. On the other hand, the resulting increase in excitation arising from the increase in membrane-bound receptors leads to the synaptic delocalization of active CaMKII due to increased calcium levels. This is consistent with the observation that the synaptic localization of CaMKII changes in response to autophosphorylation [31]. In this paper, we show how a regular spacing of synapses can be established in *C. elegans* via an underlying Turing mechanism for synaptogenesis involving a short-range activator and a long-range inhibitor. We identify the former as slowly diffusing CaMKII and the latter as a rapidly advecting GLR-1, which switches between anterograde and retrograde motor-driven transport (bidirectional transport). Our Turing mechanism is novel, since the inhibitor does not diffuse.

The outline of this paper is as follows. In section 2 we formulate a three-component (two chemical species), one-dimensional (1D) model of synaptogenesis in *C. elegans*, with

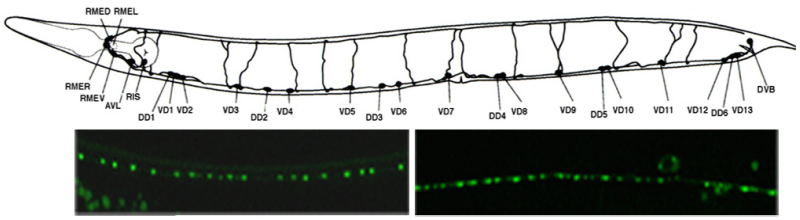

Figure 1. *Schematic figure showing distribution of synapses of the type D motor neurons. The D type neurons include six DD and* 13 *VD neurons. DD form synapses to the dorsal body muscles and VD form synapses to the ventral muscles. Blobs: synapses to muscles; arrows: synaptic inputs to the D neurons. Below are GFP images of synaptic puncta in the dorsal and ventral cords, respectively. (Public domain figure downloaded from WormBook/Synaptogenesis by Y. Jin, http://www.wormbook.org/.)*

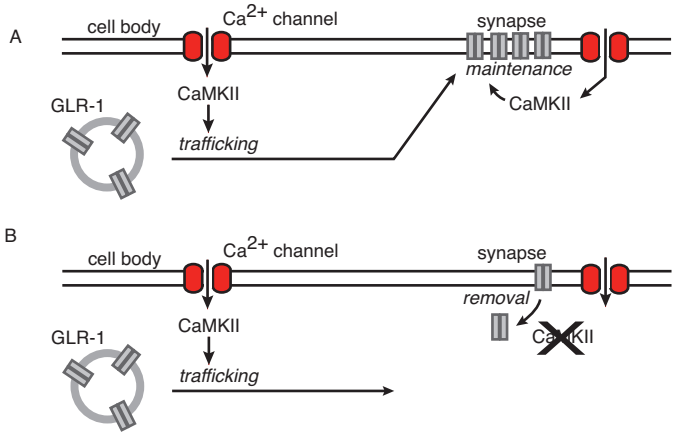

Figure 2. *Regulation of transport and delivery of GLR-1 to synapses by CaMKII.* (A) *Calcium influx through voltage-gated calcium channels activates CaMKII, which enhances the active transport and delivery of GLR-1 to synapses.* (B) *Under conditions of increased excitation, higher calcium levels result in active CaMKII which fails to localize at synapses, leading to the removal of GLR-1 from synapses.*

an activator CaMKII moving only via diffusion and an inhibitor GLR-1 traveling by active (motor-driven) transport in either the leftward or rightward direction. We take the reaction kinetics of the two chemical species to be based on a modified Gierer–Meinhardt model [8], since CaMKII exhibits autophosphorylation. We then use linear stability analysis to derive conditions for a Turing instability and construct dispersion curves (section 3). It could be argued that occurrence of patten formation in our transport model is not particularly surprising, since one might be inclined to interpret switching between left and right moving states as effectively equivalent to diffusion. However, this equivalence holds only in the limit of fast switching, and we show that this lies outside the pattern forming regime of our model. In section 4 we break the symmetry between the left- and right-moving active particles by taking their speeds to be different. This biased transport model reduces to a reaction-diffusion-advection (RDA) model in the fast switching limit. We show that the full system supports spatially periodic flow-distributed structures (FDS) on a semi-infinite domain with boundary forcing, analogous to what is found in RDAs [30]. Finally, in section 5 we highlight extensions to this work and future areas of research.

2. Three-component trafficking model. Consider a 1D domain of fixed length L, which represents a neurite in the ventral cord of *C. elegans* at a particular stage of larval development; see Figure 3. Let $R(x,t)$ denote the concentration of GLR-1 receptors at position x along the cell at time t and let $U(x,t)$ denote the corresponding concentration of active CaMKII. For simplicity, we do not distinguish between membrane-bound and cytoplasmic densities. Within the context of synaptogenesis, we will interpret steady-state regions of enhanced densities in GLR-1 and CaMKII as potential synaptic sites. This imposes one constraint on our model, namely, that spatially periodic distributions of CaMKII and GLR-1 are in-phase. (A more detailed model would explicitly take into account the Ca^{2+}-dependent localization of CaMKII

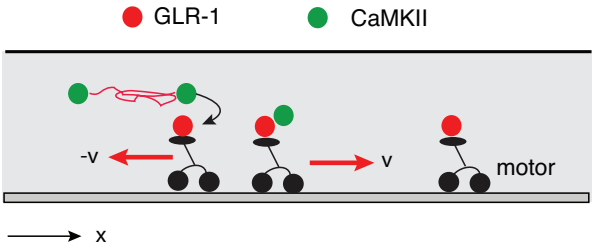

Figure 3. *One-dimensional, three-component trafficking model. Passively transported molecules of CaMKII (green) react with motor-driven actively transported molecules of GLR-1 (red). The latter can switch between forward and backward moving states (traveling with velocities $\pm v$). Interactions between motor-driven particles such as exclusion effects (hard-core repulsion) are ignored.*

at the membrane and the CaMKII-dependent delivery of GLR-1 to developing synaptic sites.) We partition GLR-1 into two subpopulations: those that undergo anterograde (rightward) transport with positive velocity v and density $R_+(x,t)$ and those that undergo retrograde (leftward) transport with negative velocity $-v$ and density $R_-(x,t)$:

$$R(x,t) = R_+(x,t) + R_-(x,t). \tag{2.1}$$

(The case of different speeds in the left and right directions will be considered in section 4.) Individual receptors randomly switch between the two advective states according to a two-state Markov process,

$$R_+ \underset{\alpha}{\overset{\alpha}{\rightleftharpoons}} R_-. \tag{2.2}$$

This is based on the assumption that actively transported particles (ATs) are transported bidirectionally along a microtubule or actin filament by some motor complex [3]. We take the various concentrations to evolve according to the system of equations

$$\frac{\partial U}{\partial t} = D\frac{\partial^2 U}{\partial x^2} + f(U,R_+,R_-), \tag{2.3a}$$

$$\frac{\partial R_+}{\partial t} = -v\frac{\partial R_+}{\partial x} - \alpha R_+ + \alpha R_- + g(U,R_+,R_-), \tag{2.3b}$$

$$\frac{\partial R_-}{\partial t} = v\frac{\partial R_-}{\partial x} + \alpha R_+ - \alpha R_- + g(U,R_+,R_-). \tag{2.3c}$$

The first term on the right-hand side of (2.3a) represents diffusive transport of CaMKII and the first term on the right-hand side of (2.3b) and (2.3c) represents ballistic transport of GLR-1 to the right or left, respectively. The terms $\pm\alpha(r-l)$ represent the effects of switching between the two advective states. The reaction term f represents both the autocatalysis of CaMKII and the inhibition of CaMKII by GLR-1, whereas the reaction terms g represent

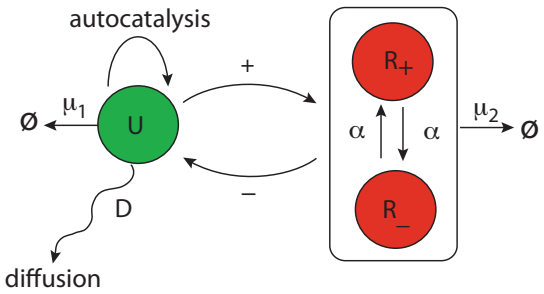

Figure 4. *Schematic diagram of modified Gierer and Meinhardt activator-inhibitor model with a passively diffusing activator (U) and an actively transported inhibitor switching between left (R_-) and right (R_+) moving states at a rate α.*

the increase in actively transported GLR-1 due to the action of CaMKII. Finally, (2.3) are supplemented by reflecting boundary conditions at the ends $x = 0, L$:

$$\left.\frac{\partial U(x,t)}{\partial x}\right|_{x=0,L} = 0, \quad vR_+(0,t) = vR_-(0,t), \quad vR_+(L,t) = vR_-(L,t). \tag{2.4}$$

It remains to specify the form of the nonlinear reaction functions f and g. Since the precise details of the interaction between CaMKII and GLR-1 are currently not known, we will adapt a classical model of autocatalysis in pattern forming systems due to Gierer and Meinhardt (GM model) [8]. The GM model consists of an activator-inhibitor system with bimolecular activation and monomolecular inhibition; see Figure 4. More specifically, we take

$$f(U, R_+, R_-) = \frac{\rho U^2}{R_+ + R_-} - \mu_1 U, \tag{2.5a}$$

$$g(U, R_+, R_-) = \rho U^2 - \mu_2(R_+ + R_-). \tag{2.5b}$$

Here, $\rho > 0$ represents the strength of interactions and μ_1, μ_2 represent the degradation rates of CaMKII and GLR-1, respectively. We are assuming that both left and right GLR-1 have an equal inhibitory effect on CaMKII, and for simplicity we have also taken g to be a symmetric function of $R_\pm$. (This can also be imposed by an appropriate shift in the switching rates; the basic results of the paper do not depend on imposing such a symmetry; see also the discussion of biased transport in section 4.) Another biologically based reason for choosing the GM model is that it generates in-phase patterns for two-component reaction-diffusion systems [20].

3. Conditions for Turing instability in trafficking model. In the following it will be convenient to rescale space and time such that $\hat{x} = \alpha x/v$ and $\hat{t} = \alpha t$, so that (2.3) become (after dropping the hat notation)

$$\frac{\partial U}{\partial t} = \gamma \frac{\partial^2 U}{\partial x^2} + \frac{1}{\alpha} f(U, R_+, R_-), \tag{3.1a}$$

$$\frac{\partial R_+}{\partial t} = -\frac{\partial R_+}{\partial x} + R_- - R_+ + \frac{1}{\alpha} g(U, R_+, R_-), \tag{3.1b}$$

$$\frac{\partial R_-}{\partial t} = \frac{\partial R_-}{\partial x} + R_+ - R_- + \frac{1}{\alpha} g(U, R_+, R_-), \tag{3.1c}$$

where

$$\gamma = \frac{\alpha D}{v^2} \tag{3.2}$$

is the nondimensional quantity relating the CaMKII diffusion coefficient, GLR-1 velocity, and motor switching rate. As we shall see, γ is the analogue of the ratio of diffusivities in classical reaction-diffusion systems [20].

3.1. Linear stability analysis. We are interested in deriving general conditions for a Turing instability in the system of equations (3.1) and then applying them to the modified GM model for synaptogenesis in *C. elegans*. We will proceed along lines analogous to the classical theory of diffusion-driven pattern formation [20, 7] by linearizing about a spatially uniform fixed point and studying the spectrum of the resulting linear operator. Since neurite length is relatively large compared to the synapse density pattern, the boundaries don't have a major effect on wavelength. Thus, we consider a homogeneous partial differential equation in the unbounded domain $\mathbb{R}$, and the associated spectrum is continuous. However, with a slight abuse of notation, we will still refer to elements $\lambda(k)$, $k \in \mathbb{R}$, of the continuous spectrum as eigenvalues and the associated Fourier components e^{ikx} as eigenfunctions. The goal is to determine conditions under which $\mathrm{Re}[\lambda(0)] < 0$ (stable with respect to homogeneous perturbations), whereas there exists a critical wavenumber k_c such that

$$\max_{k\in\mathbb{R}}\{\mathrm{Re}[\lambda(k)]\} = \mathrm{Re}[\lambda(k_c)] = \lambda(k_c) = 0.$$

Under these conditions, the fixed point is marginally stable with respect to excitation of a spatially periodic pattern of critical wavelength $2\pi/k_c$. Typically, varying one of the parameters of the underlying model can then push the associated dispersion curve $\lambda = \lambda(k)$ above zero in a neighborhood of k_c, resulting in a Turing instability. Whether a stable periodic pattern forms then depends on the nonlinearities of the system, which can be investigated numerically or by using weakly nonlinear analysis. In this paper, we shall treat the dimensionless parameter γ of (3.2) as the bifurcation parameter.

Suppose that there exists a spatially uniform fixed point $\boldsymbol{u}^* = (U^*, R_+^*, R_-^*)$ for which $f(U^*, R_+^*, R_-^*) = g(U^*, R_+^*, R_-^*) = 0$ and $R_+^* = R_-^*$. Linearizing about this fixed point by setting

$$U(x,t) = U^* + u(x,t), \quad R_+(x,t) = R_+^* + r(x,t), \quad R_-(x,t) = R_-^* + l(x,t)$$

yields the linear equation

$$\boldsymbol{u}_t = \mathbf{D}\boldsymbol{u}_{xx} + \mathbf{J}\boldsymbol{u}_x + \frac{1}{\alpha}\mathbf{A}\boldsymbol{u}, \tag{3.3}$$

where $\boldsymbol{u} = (u \quad r \quad l)^T$ and

$$\mathbf{D} = \begin{pmatrix} \gamma & 0 & 0 \\ 0 & 0 & 0 \\ 0 & 0 & 0 \end{pmatrix}, \quad \mathbf{J} = \begin{pmatrix} 0 & 0 & 0 \\ 0 & -1 & 0 \\ 0 & 0 & 1 \end{pmatrix}, \quad \mathbf{A} = \begin{pmatrix} f_u & f_r & f_r \\ g_u & -\alpha + g_r & \alpha + g_r \\ g_u & \alpha + g_r & -\alpha + g_r \end{pmatrix},$$

with all derivatives evaluated at the fixed point. We have used the fact that $f_r = f_l$ and $g_r = g_l$ at the fixed point. In the absence of spatial processes, the linearized system (3.3) reads

$$\boldsymbol{u}_t = \frac{1}{\alpha}\mathbf{A}\boldsymbol{u}, \tag{3.4}$$

where $\boldsymbol{u}$ has solutions of the form $\boldsymbol{u} \propto e^{\lambda t}$. The eigenvalues λ of this system satisfy

$$\begin{aligned} 0 = -\lambda^3 + \lambda^2 &\left(-2 + \frac{1}{\alpha}\left(f_u + 2g_r\right)\right) \\ &+\lambda\left(\frac{2}{\alpha^2}\left(-f_u g_r + f_r g_u\right) + \frac{2}{\alpha}\left(f_u + 2g_r\right)\right) + \frac{4}{\alpha^2}\left(-f_u g_r + f_r g_u\right). \end{aligned}$$

This has solutions

$$\lambda_1 = -2, \tag{3.5}$$

$$\lambda_{2,3} = \frac{1}{2\alpha}\left(f_u + 2g_r \pm \sqrt{\left(f_u + 2g_r\right)^2 - 8\left(f_u g_r - f_r g_u\right)}\right). \tag{3.6}$$

We require the steady state to be stable in the absence of spatial effects, i.e., $\mathrm{Re}(\lambda) < 0$ for all λ. Conditions for λ to be negative in the absence of spatial components are as follows:

$$f_u + 2g_r < 0, \tag{3.7a}$$

$$f_u g_r - f_r g_u > 0. \tag{3.7b}$$

Now we consider the stability of the full system with respect to spatially periodic perturbations. We assume (3.3) has a solution of the form $\boldsymbol{u}(x,t) = \boldsymbol{u}_k e^{\lambda t} e^{ikx}$, which gives the matrix equation

$$\lambda \boldsymbol{u}_k = \Delta(k)\boldsymbol{u}_k, \quad \Delta(k) = -k^2\gamma + ikJ + \frac{1}{\alpha}A. \tag{3.8}$$

Hence, λ satisfies the characteristic equation

$$\begin{aligned} 0 = \det[\Delta(k) - \lambda I_3] = -\lambda^3 &+ \lambda^2\left(-2 - \gamma k^2 + \frac{1}{\alpha}\left(f_u + 2g_r\right)\right) \\ &+ \lambda\left(\frac{2}{\alpha^2}\left(-f_u g_r + f_r g_u\right) + \frac{2}{\alpha}\left(f_u + 2g_r + \gamma g_r k^2\right) - k^2 - 2\gamma k^2\right) \\ &+ \frac{4}{\alpha^2}\left(-f_u g_r + f_r g_u\right) + \frac{k^2}{\alpha}\left(f_u + 4\gamma g_r\right) - \gamma k^4. \end{aligned}$$

This can be written in the more compact form

$$\lambda^3 + b(k)\lambda^2 + c(k)\lambda + h(k) = 0, \tag{3.9}$$

where

$$b(k) = 2 + \gamma k^2 - \frac{1}{\alpha}(f_u + 2g_r) > 0, \tag{3.10a}$$

$$c(k) = \frac{2}{\alpha^2}\left(f_u g_r - f_r g_u\right) - \frac{2}{\alpha}\left(f_u + 2g_r + \gamma g_r k^2\right) + k^2 + 2\gamma k^2, \tag{3.10b}$$

and

$$h(k) = \frac{4}{\alpha^2}\left(f_u g_r - f_r g_u\right) - \frac{k^2}{\alpha}\left(f_u + 4\gamma g_r\right) + \gamma k^4. \tag{3.10c}$$

In general, for each value of k there will be three eigenvalues $\lambda_j(k)$, $j = 1, 2, 3$, one of which will be real and the other two either are real or form a complex conjugate pair. There are thus three solution branches or dispersion curves. Note, in particular, that in the limit $|k| \to \infty$, the three roots behave as $\lambda_1(k) \sim -k^2\gamma, \lambda_{2,3}(k) \sim \pm ik$.

We now determine conditions for the fixed point to become unstable with respect to non-oscillatory spatially periodic patterns. This means that a single real dispersion curve crosses zero from below, while the other pair of (possibly complex conjugate) branches have negative real parts for all k. A necessary condition is that there exists a wavenumber k for which there is a single real root $\lambda(k) = 0$. In order for this to hold, the λ-independent term in (3.9) must vanish, $h(k) = 0$, which implies

$$k^2 = \frac{1}{2\alpha\gamma}\left(f_u + 4\gamma g_r \pm \sqrt{\left(f_u + 4\gamma g_r\right)^2 - 16\gamma\left(f_u g_r - f_r g_u\right)}\right). \tag{3.11}$$

There are then two conditions for (3.11) to have a real solution k: (1) the discriminant is positive, and (2) k^2 is positive. The first condition implies that

$$\left(f_u + 4\gamma g_r\right)^2 > 16\gamma\left(f_u g_r - f_r g_u\right), \tag{3.12}$$

which certainly holds for sufficiently small γ. Positivity of k^2 then requires

$$f_u + 4\gamma g_r > 0. \tag{3.13}$$

The condition (3.13) on γ depends on the sign of g_r, that is,

$$\begin{aligned} \gamma &> -\frac{f_u}{4g_r}, \quad g_r > 0, \\ \gamma &< -\frac{f_u}{4g_r} \quad g_r < 0. \end{aligned} \tag{3.14}$$

The first case, $g_r > 0$, implies that $f_u < 0$ due to condition (3.7a). On the other hand, if $g_r < 0$, then $f_u > 0$, since the condition $f_u < 0$ would imply that the positive quantity γ would be less than a negative quantity. We conclude that f_u and g_r must have opposite sign and, hence, f_r and g_u also have opposite sign; see (3.7b).

In general, there will be two positive roots k for which $\lambda(k) = 0$, suggesting that when the discriminant vanishes in (3.11) for some $\gamma = \gamma_c$ and $k = k_c$, the fixed point is marginally stable with respect to the Fourier mode $e^{ik_c x}$. However, in order to eliminate the possibility of a Turing–Hopf bifurcation, we must check that a pair of pure imaginary roots $\pm i\omega$ cannot

occur at some value of k. As we show below, this leads to the additional requirement that $g_r < 0$ and, hence, $f_u > 0$. Conditions (3.7a), (3.7b), and (3.14) then imply that

$$\gamma < -\frac{f_u}{4g_r} < \frac{1}{2}, \quad g_r < 0, \quad f_u > 0, \quad f_r g_u < 0. \tag{3.15}$$

Setting $\lambda(k) = i\omega(k)$ in (3.9) for real $\omega(k)$ and equating real and imaginary parts generates the pair of equations

$$c(k) - \omega^2 = 0, \quad h(k) - b(k)\omega^2 = 0 \Rightarrow c(k)b(k) = h(k) > 0.$$

Writing $c(k)b(k) = a_0 + a_1k^2 + a_2k^4$ and $h(k) = h_0 + h_1k^2 + h_2k^4$, we find from (3.7a), (3.7b), (3.13) and $g_r < 0$ that $a_0 > b_0$, $a_1 > 0$, $h_1 < 0$, and $a_2 > h_2$ so $c(k)b(k) > h(k)$ for all k. In other words, a pair of complex conjugate roots cannot cross the imaginary axis. This result is a special case of a more general theorem due to Guckenheimer, Myers, and Sturmfels [9]. For completeness, we state the theorem here.

THEOREM (Guckenheimer, Myers, and Sturmfels). *Let* $\mathbf{S}$ *by the Sylvester matrix for the characteristic polynomial* $p(\lambda)$ *of an* $n \times n$ *matrix* Δ. *Then,* Δ *has precisely one pair of pure imaginary eigenvalues if* $\det(\mathbf{S}) = 0$ *and* $\det(\mathbf{S}_0) \cdot (\mathbf{S}_1) > 0$, *where* $\mathbf{S}_{i=0,1}$ *denotes the matrices obtain from* $\mathbf{S}$ *by deleting row* 1 *and* $n/2$ *and columns* 1 *and* $i+2$. *If* $\det(\mathbf{S}) \neq 0$, *or* $\det(\mathbf{S}_0) \cdot \det(\mathbf{S}_1) < 0$, *then* $p(\lambda)$ *has no purely imaginary roots.*

For our $n = 3$ system the corresponding Sylvester matrix is

$$\mathbf{S}(k) = \begin{pmatrix} h(k) & b(k) \\ c(k) & 1 \end{pmatrix}, \tag{3.16}$$

and we have shown $\det(\mathbf{S}(k)) \neq 0$ for all k.

3.2. Dispersion curves. We now apply the above linear stability analysis to the modified GM reaction scheme given by (2.5). In the absence of spatial disturbances, the steady state for this model is

$$U^* = \frac{\mu_2}{\mu_1}, \quad R_+^* = R_-^* = \frac{\rho\mu_2}{2\mu_1^2},$$

so we have the following derivatives evaluated at steady state:

$$f_u = 2\mu_1, \quad f_r = -\frac{\mu_1^2}{\rho,} \quad g_u = \frac{2\rho\mu_2}{\mu_1}, \quad g_r = -\mu_2. \tag{3.17}$$

For this model, the condition that f_u and g_r have opposite signs at steady state is already satisfied for any positive values of μ_1 and μ_2. To satisfy the remaining conditions (3.15) for stability in the homogeneous steady state, we require

$$f_u + 2g_r < 0 \Rightarrow \mu_1 < \mu_2$$

from (3.7a). Second,

$$f_u g_r - f_r g_u = 0$$

which is a limiting case of (3.7b). Thus, we have a (marginally) stable homogeneous steady state in the absence of spatial disturbances, provided that the inhibitor GLR-1 decays more

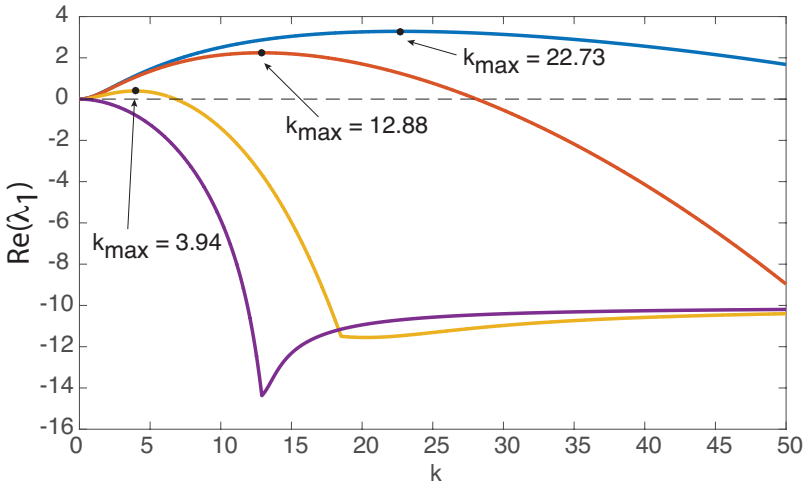

Figure 5. *Dispersion curves for the transport model (2.3) with modified GM kinetics (2.5). We choose* $\rho = 1, \mu_1 = 0.25, \mu_2 = 1, \alpha = 0.11$, *and* $v = 1$ *in order to match biophysical parameters and satisfy the spatially homogeneous stability conditions.* λ_1 *represents the eigenvalue of the system with largest real part for a given* k. *We look at dispersion curves for four different values of* D: $D = 0.01$ *(blue),* $D = 0.05$ *(red),* $D = 0.5$ *(yellow),* $D = 1.5$ *(purple). The maximum value of* λ_1 *occurs at some value* $k_{\max}$, *which gives the dominant mode for pattern formation.*

quickly than the activator CaMKII. It remains to consider the necessary condition (3.15) on γ for a Turing instability to occur. In this case of the Gierer–Meinhardt model, the condition reads

$$\gamma < \frac{\mu_1}{2\mu_2} < \frac{1}{2}.$$

In Figure 5, we show the dispersion curves for the trafficking system with Gierer–Meinhardt nonlinearities. That is, we plot $\mathrm{Re}[\lambda_1]$ against wavenumber k, where λ_1 is the eigenvalue with largest real part. One finds that in any region where $\mathrm{Re}[\lambda_1] > 0$, λ_1 is real, thus signaling the growth of nonoscillatory spatially periodic patterns, with the maximum of the curve representing the fastest growing mode. As γ increases (i.e., either D increases or v decreases), instabilities disappear as predicted by the theory. Figure 6 shows a numerically simulated example of pattern formation in the 1D trafficking system with Gierer–Meinhardt dynamics. The corresponding time evolution of the pattern is illustrated in Figure 7.

3.2.1. Parameter values. In order to justify the trafficking-based mechanism for pattern formation in *C. elegans*, the conditions for Turing instability must be satisfied for biophysically relevant parameters. Many of these parameters can be cited from the biological literature. First, we note that the conditions for stability in the homogeneous steady state are satisfied in this system because the decay rate of GLR-1 is approximately four times that of CaMKII [13, Table 1]. For our simulations, we take $\mu_1 = 0.25/s$ and $\mu_2 = 1/s$. Additionally, there exists data on the transport of GLR-1 via molecular motors. The average velocity of GLR-1

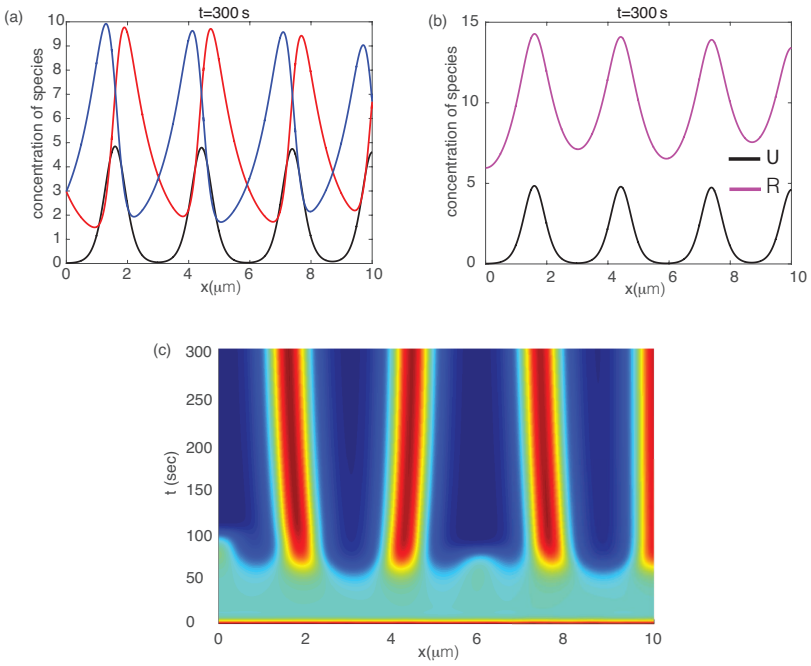

Figure 6. *Synapse site pattern formation in* C. elegans *active transport model.* (a) *Spatial profiles of the steady-state concentration of components* $U, R_\pm$. (b) *Another example of spatial profiles showing that* U *and* $R = R_+ + R_-$ *are in-phase. Initial data are generated from a uniform random distribution. Nonlinearity parameters are the same as in Figure* 5*, with* $D = 0.01\ \mu m^2/s$. (c) *Full solution in space and time. Colors represent concentrations of GLR-*1 $= R_+ + R_-$*, with red representing areas of highest concentration. Our simulation shows the emergence of* $\sim$4 *synapse sites in* 10 μm*. In this and subsequent figures, simulations were performed using a Crank–Nicolson scheme for* U *and a Lax–Wendroff scheme for* $R_\pm$ *with time step* $dt = 0.005$*, space step* $dx = 0.01$*, and no-flux boundary conditions.*

undergoing active transport along the ventral cord is 1 μm/s, with an average run length of 9.2 μm [19]. From this, we can infer that our switching rate should be $\alpha \approx 0.11/s$.

We begin with concentrations chosen from a uniform random distribution near fixed point values. As the system evolves, we initially observe growth of CAMKII concentrations, and then patterns emerge as the activator is eventually tempered by increase of the inhibitor GLR-1. In this case, the concentration of both activating and inhibiting species are in phase with each other. In order to test the validity of our mechanism, we seek to match data due to Rongo and Kaplan [26], which show that *C. elegans* synaptic density is fixed at 3.7 ± 0.1 per 10 μm. With the parameter values discussed here, our numerical simulations show good agreement with the biophysical system, with $\sim$4 potential synapse sites per 10 μm (see Figure 6).

3.3. The reaction-diffusion limit. At first sight it could be argued that the occurrence of a Turing instability in the active transport model (2.3) is not surprising since it is well known that in the fast switching limit $\alpha \to \infty$ the transport model reduces to a two-component reaction-diffusion system [21]. However, recall from (3.2) that three quantities make up the

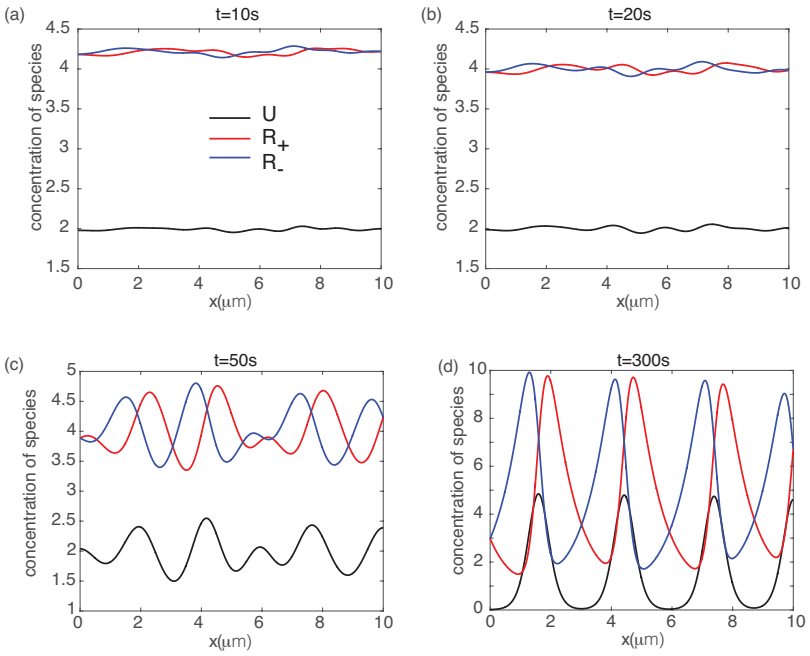

Figure 7. *Time evolution of synapse site pattern formation in* C. elegans *active transport model. Each plot shows the concentration of species* $U, R_{\pm}$ *as a function of* x *for a specific time* t*. Initial data are generated from a uniform random distribution. Nonlinearity parameters are the same as in Figure 5 with* $D = 0.01\ \mu m^2/s$*.*

dimensionless bifurcation parameter γ: v, D, and α. We have shown that γ has to be sufficiently small for pattern formation to occur in the active transport model. That is, in the limit of fast switching we have $v^2/D \ll \alpha$, which suggests that the effective diffusive transport of the inhibitor GLR-1 is much slower than the activator CaMKII. Since the occurrence of a Turing instability in a reaction-diffusion model with GM kinetics requires fast inhibition and slow activation [18, 20], we expect pattern formation to disappear in the fast switching limit, which is indeed found to be the case.

In order to explore this issue in a little more detail, we apply a quasi-steady-state diffusion approximation to the linearized version of (2.3) along the lines of [21]. First, we set $\alpha = \alpha_0/\epsilon$, where $\epsilon << 1$ is chosen so that $\alpha_0 = \mathcal{O}\left(v^2/D\right)$. We then rewrite the original system (2.3), linearized about the fixed point, as

$$\boldsymbol{u}_t = \mathbf{D}\boldsymbol{u}_{xx} + \mathbf{V}\boldsymbol{u}_x + \frac{\alpha_0}{\epsilon}\mathbf{A}\boldsymbol{u} + \mathbf{B}\boldsymbol{u}, \tag{3.18}$$

where $\boldsymbol{u} = (u \quad r \quad l)^T$ and

$$\mathbf{D} = \begin{pmatrix} D & 0 & 0 \\ 0 & 0 & 0 \\ 0 & 0 & 0 \end{pmatrix}, \quad \mathbf{V} = \begin{pmatrix} 0 & 0 & 0 \\ 0 & -v & 0 \\ 0 & 0 & v \end{pmatrix},$$

$$\mathbf{A} = \begin{pmatrix} 0 & 0 & 0 \\ 0 & -1 & 1 \\ 0 & 1 & -1 \end{pmatrix}, \quad \mathbf{B} = \begin{pmatrix} f_u & f_r & f_r \\ g_u & g_r & g_r \\ g_u & g_r & g_r \end{pmatrix}.$$

Note that the symmetric matrix $\mathbf{A}$ has a 2D nullspace ϕ spanned by

$$\left\{ \phi_1 = \begin{pmatrix} 1 \\ 0 \\ 0 \end{pmatrix}, \phi_2 = \frac{1}{\sqrt{2}} \begin{pmatrix} 0 \\ 1 \\ 1 \end{pmatrix} \right\},$$

with $\langle \phi_i, \phi_j \rangle = \delta_{ij}$ In order to separate the timescales and perform the quasi-steady-state reduction, we introduce the decomposition

$$\boldsymbol{u}(x,t) = \sum_{i=1,2} C_i(x,t)\phi_i(x,t) + \epsilon \boldsymbol{w}(x,t), \tag{3.19}$$

where $C_i(x,t) = \langle \phi_i, \boldsymbol{u} \rangle$. We observe two things about this decomposition: first, $C_i(x,t)$ is a projection, into the nullspace of $\mathbf{A}$, and second, w must be orthogonal to the nullspace of $\mathbf{A}$ so $\boldsymbol{w} = (w/\sqrt{2})\left((0,1,-1)^\top\right)$. Substituting (3.19) into (3.18) yields

$$\begin{aligned} \frac{\partial}{\partial t}\left[\sum_{i=1,2} C_i\phi_i\right] + \epsilon\frac{\partial \boldsymbol{w}}{\partial t} &= \alpha_0 \mathbf{A}\boldsymbol{w} + \sum_{i=1,2} C_i \mathbf{B}\phi_i + \frac{\partial C_2}{\partial x}\mathbf{V}\phi_2 + \frac{\partial^2 C_1}{\partial x^2}\mathbf{D}\phi_1 \\ &\quad + \epsilon\left(\mathbf{B}\boldsymbol{w} + \mathbf{V}\frac{\partial \boldsymbol{w}}{\partial x} + \mathbf{D}\frac{\partial^2 \boldsymbol{w}}{\partial x^2}\right). \end{aligned} \tag{3.20}$$

We project onto the slow manifold by multiplying by ϕ_i^T to give

$$\begin{aligned} \frac{\partial C_1}{\partial t} &= \sum_{i=1,2} C_i \phi_1^T \mathbf{B}\phi_i + d\frac{\partial^2 C_1}{\partial x^2} + \epsilon\phi_1^T\left(\mathbf{B}\boldsymbol{w} + \mathbf{D}\frac{\partial^2 \boldsymbol{w}}{\partial x^2}\right), \\ \frac{\partial C_2}{\partial t} &= \sum_{i=1,2} C_i \phi_2^T \mathbf{B}\phi_i + \epsilon\left(\phi_2^T\mathbf{B}\boldsymbol{w} + \phi_2^T\mathbf{V}\frac{\partial \boldsymbol{w}}{\partial x}\right). \end{aligned}$$

Note that $\mathbf{B}\boldsymbol{w} = 0$ and $\mathbf{D}\boldsymbol{w} = 0$. Next, we plug the slow equations into (3.20) to obtain an equation for w. After an application of the Fredholm alternative theorem we find that to leading order

$$\boldsymbol{w} = \frac{v}{2\alpha_0}\begin{pmatrix} 0 \\ -1 \\ 1 \end{pmatrix}\frac{\partial C_2}{\partial x}. \tag{3.21}$$

Finally, we obtain the desired slow manifold equations by substituting in this leading order approximation for $\boldsymbol{w}$ and simplifying. Doing so leaves us with the reduced system

$$\frac{\partial C_1}{\partial t} = f_u C_1 + \sqrt{2} f_r C_2 + D\frac{\partial^2 C_1}{\partial x^2}, \tag{3.22}$$

$$\frac{\partial C_2}{\partial t} = \sqrt{2} g_u C_1 + 2 g_r C_2 + \epsilon\frac{v^2}{\sqrt{2}\alpha_0}\frac{\partial^2 C_2}{\partial x^2}. \tag{3.23}$$

A in the full model (2.3), stability of the zero solution with respect to spatially uniform perturbations is ensured by conditions (3.7a) and (3.7b). Let $D_1 = D$ and $D_2 = \epsilon v^2/\sqrt{2}\alpha_0$. A standard analysis of reaction diffusion systems leads to the following necessary condition for a Turing instability [20]:

$$D_2 f_u + 2D_1 g_r > 0. \tag{3.24}$$

When this is combined with the conditions $f_u + 2g_r < 0$, $f_u > 0$, and $g_r < 0$, we deduce that a necessary condition for a Turing instability is $D_2 > D_1$. This clearly cannot hold in the small ϵ limit (fast switching). This establishes that in the regime where bidirectional active transport effectively reduces to diffusion, a Turing instability cannot occur.

4. Biased active transport. So far we have assumed that the switching rates and speeds are the same for left-moving and right-moving particles. Now suppose that the speeds of the right-moving and left-moving states are v_r and v_l, respectively, with $v_l < v_r$. The mean speed of the active particles is then $\bar{v} = (v_r - v_l)/2$ and there is an additional advection term $-\bar{v}\partial C_2/\partial x$ on the right-hand side of (3.23). We thus obtain a linearized version of an RDA system. There is a growing literature on pattern formation in 1D RDA equations, where one typically considers a finite or semi-infinite domain with some form of forcing at one end ($x = 0$, say) [28, 29, 30, 37]. The combination of forcing, advection, diffusion, and nonlinear reactions can lead to so-called stationary FDS. This suggests that we look for the analogue of an FDS in a biased version of our three-component trafficking model. The nondimensionalized equations with $v_r = v$ and $v_l = \nu v$ become (after rescaling)

$$\frac{\partial U}{\partial t} = \gamma \frac{\partial^2 U}{\partial x^2} + \frac{1}{\alpha} f(U, R_+, R_-), \tag{4.1a}$$

$$\frac{\partial R_+}{\partial t} = -\frac{\partial R_+}{\partial x} + R_- - R + \frac{1}{\alpha} g(U, R_+, R_-), \tag{4.1b}$$

$$\frac{\partial R_-}{\partial t} = \nu \frac{\partial R_-}{\partial x} + R_+ - R_- + \frac{1}{\alpha} g(U, R_+, R_-), \tag{4.1c}$$

where now we take $x \in [0, \infty)$ with the following boundary conditions at $x = 0$ [30]:

$$U(0,t) = U^* + \epsilon_u(t), \quad R_+(0,t) = R_+^* + \epsilon_r(t), \quad R_-(0,t) = R_-^* + \epsilon_l(t), \tag{4.2}$$

for any $t > 0$, where

$$\epsilon_i(t) = \begin{cases} \epsilon_i & \text{if } 0 \le t \le T, \\ 0 & \text{otherwise,} \end{cases} \tag{4.3}$$

and $\epsilon_i, |\epsilon_i| \ll 1$ for $i = u, r, l$ are small constant perturbations that are maintained for a long but finite time T. Here $\mathbf{u}^* = (u^*, r^*, l^*)$ is the spatially uniform steady state. Linearizing about this steady-state solution leads to (3.3) with the same matrices $\mathbf{A}$ and $\mathbf{D}$, and the modified matrix

$$\mathbf{J} = \begin{pmatrix} 0 & 0 & 0 \\ 0 & -1 & 0 \\ 0 & 0 & \nu \end{pmatrix}.$$

Equation (3.3) is supplemented by the boundary conditions

$$u(0,t) = \epsilon_u(t), \quad r(0,t) = \epsilon_r(t), \quad l(0,t) = \epsilon_l(t), \tag{4.4}$$

Since the time-dependent perturbations have compact support in time, they have well-defined Fourier transforms. Therefore, we seek the general solution of (3.3) of the form [30]

$$(u(x,t), r(x,t), l(x,t)) = \int_{-\infty}^{\infty} (u_0(\omega), r_0(\omega), l_0(\omega)) \epsilon^{i\omega t + z(\omega)x} d\omega, \tag{4.5}$$

where $u_0(\omega)$, etc., are determined by the boundary data. Substituting the general solution into (3.3) shows that (ω, z) must satisfy the characteristic equation

$$\begin{aligned} 0 = &-(i\omega)^3 + (i\omega)^2 \left((\nu - 1)z - 2 + \gamma z^2 + \frac{1}{\alpha}(f_u + 2g_r) \right) \\ &+ i\omega \left(\frac{2}{\alpha^2}(\Delta) + \frac{2}{\alpha}\left(f_u + 2g_r - \gamma g_r z^2\right) + \nu z^2 + 2\gamma z^2 \right. \\ &\left. -(\nu - 1)z \left[-1 + z^2\gamma + \frac{f_u + g_r}{\alpha} \right] \right) \\ &+ \frac{4}{\alpha^2}(\Delta) - \frac{z^2}{\alpha}(\nu f_u + 4\gamma g_r) - \gamma\nu z^4 \\ &+ (\nu - 1)z \left[\frac{-\Delta}{\alpha^2} - \gamma z^2 - \frac{f_u - \gamma z^2 g_r}{\alpha} \right]. \end{aligned} \tag{4.6}$$

For notational convenience, we let $\Delta = f_r g_u - f_u g_r$. A necessary condition for a stationary-space periodic solution is that the ω-independent term in (4.6) vanishes:

$$\begin{aligned} &\gamma\nu z^4 + \gamma(\nu - 1)\left(1 - \frac{g_r}{\alpha}\right) z^3 + \frac{z^2}{\alpha}(\nu f_u + 4\gamma g_r) \\ &\quad - (\nu - 1)z \left[\frac{-\Delta}{\alpha^2} - \frac{f_u}{\alpha} \right] - \frac{4}{\alpha^2}\Delta = 0. \end{aligned} \tag{4.7}$$

Solutions that bifurcate to spatially periodic FDS have a purely imaginary wavenumber $z_c = ik_c$. The vanishing of the imaginary part of (4.7) when $z = ik_c$ shows that the critical wavenumber is

$$k_c^2 = \frac{\alpha f_u + \Delta}{\alpha\gamma(\alpha - g_r)}, \tag{4.8}$$

which exists provided that the right-hand side is positive. Note that k_c is independent of the speed bias ν.

We can now determine the neutral curve in (γ, ν) parameter space for the boundary-forcing problem that corresponds to the bifurcation to stationary (FDS) solutions by requiring that the real part of (4.7) vanishes when $z = ik_c$ and solving for ν:

$$\nu^*(\gamma) = \frac{4\left(\Delta + \alpha\gamma g_r k_c^2(\gamma)\right)}{\alpha k_c^2(\gamma)\left(\alpha\gamma k_c^2(\gamma) - f_u\right)}. \tag{4.9}$$

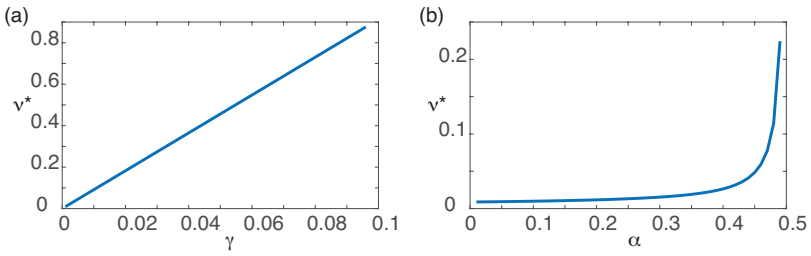

Figure 8. *Plot of* (a) *the* (α, ν^*) *and* (b) *the* (γ, ν^*) *curves for the Gierer–Meinhardt synaptogenesis model with biased active transport. We predict pattern forming instabilities to arise for regions where* $\nu > \nu^*$. *For the Gierer–Meinhardt model, we take nonlinearity parameters* $\rho = 1, \mu_1 = 0.25, \mu_2 = 1$.

We can further simplify this by plugging in our expression for k_c^2,

$$\nu^*(\gamma) = \frac{4\gamma\alpha\,(\alpha - g_r)}{\alpha f_u + \Delta}, \tag{4.10}$$

provided $\alpha - g_r \neq 0$ and $\alpha f_u + \Delta \neq 0$. In seeking stationary FDS solutions, we require that $k_c^2 > 0$ and $\nu^*(\gamma) > 0$. We predict that for ν above this curve defined by ν^*, we will see such solutions. We restrict our analysis here to the case we have explored previously, namely, the Gierer–Meinhardt model. Figure 8 shows the neutral curves in (γ, ν) and (α, ν) parameter space. Since $g_r < 0$, we know that $\alpha - g_r > 0$. This implies that we have the following condition for $k_c^2 > 0$:

$$\alpha f_u + \Delta > 0. \tag{4.11}$$

We show examples of pattern formation in this biased transport regime in Figure 9 for the Gierer–Meinhardt model under multiple values of $\nu > \nu^*$. These patterns arise due to instability and persist in time, despite the underlying net flow to the right. However, we remark here that for certain parameter values, it is possible to generate transient convective instabilities, where the emergent patterns are eventually convected away from their initial perturbation and out of the domain in long times [27, 32]. Further explorations of types of instabilities and conditions under which they arise are not explored in the present work, but yield interesting opportunities for future analysis. Finally, it is important to note that, as in the case of Turing instabilities, FDS solutions do not occur in the fast switching limit for which biased bidirectional transport reduces to advection-diffusion.

5. Discussion. In summary, we have established the existence of an active trafficking-based mechanism for Turing pattern formation in a simple 1D model of synaptogenesis in *C. elegans*. Our model assumes that synaptogenesis is generated by an activator-inhibitor system consisting of passively diffusing Ca^{2+}/calmodulin-dependent protein kinase (CAMKII) and actively transported glutamate receptor 1 (GLR-1). Interactions between the two chemical species were modeled in terms of modified GM kinetics. We used linear stability analysis to derive conditions for a Turing instability and found that $\gamma = \alpha D/v^2$ has to be sufficiently small for patterns to emerge, where α is the motor switching rate, D is the CaMKII diffusion coefficient, and v is the speed of motor-driven GLR-1. One consequence is that patterns

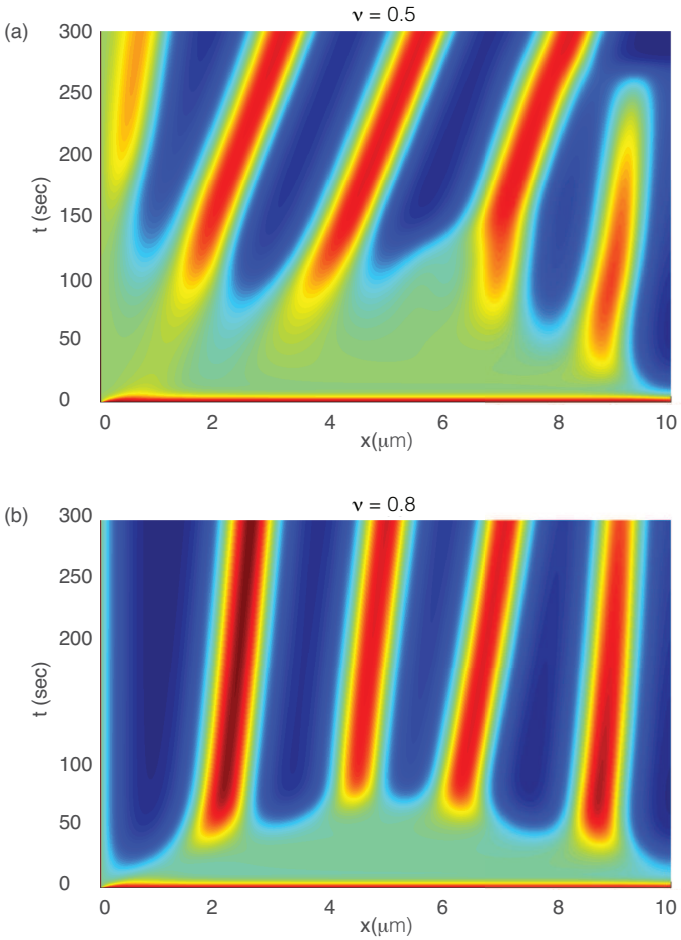

Figure 9. *Examples of evolution of patterns in the Gierer–Meinhardt model under biased active transport. We show two different values of $\nu > \nu^*$:* (a) $\nu = 0.5$ *and* (b) $\nu = 0.8$. *We take* $\rho = 1, \mu_1 = 0.25, \mu_2 = 1, \gamma = 0.0011$, *and* $\alpha = .11$, *as in Figure 8. Despite a biasing in anterograde versus retrograde transport speeds, the density of potential synaptic sites is still properly regulated. Note that despite a net flow to the right, patterns persist in long times (as opposed to being convected out of the domain). Numerical simulations were performed with the Crank–Nicolson scheme for diffusion and Lax–Wendroff scheme for advection with* $\Delta x = 0.01$ *and* $\Delta t = 0.005$. *We take Dirichlet boundary conditions on the left and no flux boundary conditions on the right.*

emerge outside the parameter regime of fast switching, where the linearized model reduces to a two-component reaction-diffusion system. In the case of GM kinetics, the spatially periodic densities for CaMKII and GLR-1 were in-phase, consistent with the interpretation of regions with enhanced densities corresponding to regularly spaced synaptic sites. Moreover, for physiologically reasonable choices of various biophysical parameters such as the diffusivity, motor speed, and degradation rates, the resulting synaptic spacing (pattern wavelength) is

consistent with experimental data. Our results were also robust to changes in these parameters and persisted in the case of biased transport.

Further evidence for our hypothesis that synaptogenesis arises via a Turing mechanism is the observation that the spacing between synapses is maintained during larval growth [26]. In the case of reaction-diffusion equations, the role of domain growth in pattern formation has been investigated by a number of authors [35, 5, 24, 4, 6]. Much of this work has been inspired by experimental observations concerning the skin pigmentation of the marine angelfish [15]. In juvenile fish, the skin color is initially gray and then develops alternating white stripes on a dark blue background. New white stripes are inserted between the existing older stripes, resulting in a doubling of the number of stripes each time the fish doubles in size. Stripe insertion has also been modeled within the context of ocular dominance columns within developing cortex [23]. In the case of synaptogenesis in *C. elegans*, maintenance of synaptic density could be analogous to a stripe insertion mechanism and is something we hope to explore in future work. We will also develop a more detailed multicomponent model that explicitly distinguishes between cytoplasmic and membrane-bound densities.

Another possible extension of our work would be to analyze the generation of patterns in higher spatial dimensions. In the case of axonal or dendritic transport in neurons, microtubules tend to be aligned in parallel so that one can treat the transport process as effectively 1D. On the other hand, intracellular transport within the cell body of neurons and most nonpolarized animal cells occurs along a microtubular network that projects radially from organizing centers (centrosomes) with outward polarity. This allows the delivery of cargo to and from the nucleus. It has also been found that microtubules bend due to large internal stresses, resulting in a locally disordered network. A detailed microscopic model of intracellular transport within the cell would need to specify the spatial distribution of microtubular orientations and polarity, in order to determine which velocity states are available to a motor-cargo complex at a particular spatial location. However, a simplified model can be obtained under the "homogenization" assumption that the network is sufficiently dense so that the set of velocity states (and associated state transitions) available to a motor complex is independent of position. In that case, one can effectively represent the active transport within the cell in terms of a 2D or 3D model of active transport [2, 3].

For the sake of illustration, consider a disordered 2D microtubular network as illustrated in Figure 10. We assume that ATs are transported along this network, randomly switching between different motile states, and interacting with a second chemical species passively transported particles (PT) undergoing 2D diffusion. Suppose that after homogenization, an AT at any point $\mathbf{r} = (x, y)$ in the plane can exhibit ballistic motion with velocity $\mathbf{v}(\theta) = v(\cos\theta, \sin\theta)$ for $\theta \in [0, 2\pi)$ or be in a stationary state. Transitions between different ballistic states are governed by a discrete Markov process with θ-independent transition rate α. Let $c(\mathbf{r}, \theta, t)$ be the concentration of ATs in state $(\mathbf{r}, \theta)$ at time t and $u(\mathbf{r}, t)$ denote the concentration of PT. The 2D analogue of (2.3) is taken to be

$$\frac{\partial u}{\partial t} = d\nabla^2 u + f(u, C),$$
$$\frac{\partial c}{\partial t} = -\nabla \cdot (\mathbf{v}(\theta)c) - \alpha c(\mathbf{r}, \theta, t) + \alpha C(\mathbf{r}, t) + g(u, C),$$

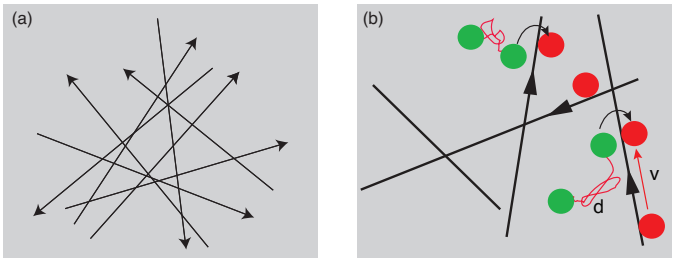

Figure 10. *Active transport on a disordered microtubular network.* (a) *Random orientational arrangement of microtubules.* (b) *Effective 2D trajectory of an AT (red) randomly switching directions and reacting with the ATs (green).*

where

$$C(\mathbf{r},t)=\frac{1}{2\pi}\int_0^{2\pi} c(\mathbf{r},\theta',t)d\theta'.$$

Alternatively, one could take $g(u,c)$ rather than the more symmetric case of $g(u,C)$.

Finally, the new class of model introduced in this paper raises many interesting questions from a mathematical perspective. First, we are considering coupled hyperbolic and parabolic nonlinear PDEs — what are the conditions for well-posedness (existence, uniqueness, stability) for such equations? Second, we focused on the issue of linear stability in order to derive necessary conditions for a Turing instability. However, if one wants to determine the selection and stability of the emerging patterns, it is necessary to take into account the nonlinearities of the system using methods such as weakly nonlinear analysis. This then raises a third issue, namely, the role of symmetry in the selection of patterns. This is a well-studied area in the case of reaction-diffusion systems with an underlying Euclidean symmetry [14]. An additional complicating feature of our trafficking model is that a 2D or 3D microtubular network tends to break Euclidean symmetry, and this depends on the spatial scale at which one is modeling.

REFERENCES

[1] M. Alber, H. G. E. Hentschel, B. Kazmierczak, and S. A. Newman *Existence of solutions to a new model of biological pattern formation*, J. Math. Anal. Appl., 308 (2004), pp. 175–194.
[2] O. Benichou, C. Loverdo, M. Moreau, and R. Voituriez, *Intermittent search strategies*, Rev. Mod. Phys., 83 (2011), pp. 81–129.
[3] P. C. Bressloff, *Stochastic Processes in Cell Biology*, Springer, New York, 2014.
[4] M. A. J. Chaplain, M. Ganesh, and I. G. Graham, *Spatio-temporal pattern formation on spherical surfaces: Numerical simulation and application to solid tumor growth*, J. Math. Biol., 42 (2001), pp. 387–423.
[5] E. J. Crampin, E. A. Gaffney, and P. K. Maini, *Reaction and diffusion on growing domains: Scenarios for robust pattern formation*, Bull. Math. Biol., 61 (1999), pp. 1093–1120.
[6] E. J. Crampin, E. A. Gaffney, and P. K. Maini. *Mode-doubling and tripling in reaction-diffusion patterns on growing domains: A piecewise linear model*, J. Math. Biol., 44, (2002), pp. 107–128.
[7] L. Edelstein-Keshet, *Mathematical Models in Biology*, Classics in Appl. Math. 46, SIAM, Philadelphia, 1988.
[8] A. Gierer and H. Meinhardt, *A theory of biological pattern formation*, Kybernetik, 12 (1972), pp. 30–39.

[9] J. Guckenheimer, M. Myers, and B. Sturmfels, *Computing Hopf bifurcations* I, SIAM J. Numer. Anal., 34 (1997), pp. 1–21.
[10] A. K. Harris, P. Warner, and D. Stopak, *Generation of spatially periodic patterns by a mechanical instability: A mechanical alternative to the Turing model*, Development, 80 (1984), pp. 1–20.
[11] F. J. Hoerndli, D. A. Maxfield, P. J. Brockie, J. E. Mellem, E. Jensen, R. Wang, D. M. Madsen, and A. V. Maricq. *Kinesin-1 regulates synaptic strength by mediating the delivery, removal, and redistribution of AMPA receptors.* Neuron, 80 (2013), pp. 1421–1437.
[12] F. J. Hoerndli, R. Wang, J. E. Mellem, A. Kallarackal, P. J. Brockie, C. Thacker, E. Jensen, D. M. Madsen, and A. V. Maricq. *Neuronal activity and CaMKII regulate kinesin-mediated transport of synaptic AMPARs.* Neuron, 86 (2015), pp. 457–474.
[13] C. Hanus and E. M. Schuman, *Proteostasis in complex dendrites*, Nature Rev. Neurosci., 14 (2013), pp. 638–648.
[14] R. B. Hoyle, *Pattern Formation: An Introduction to Methods*, Cambridge University Press, Cambridge, UK, 2006.
[15] S. Kondo and R. Asai, *A reaction–diffusion wave on the skin of the marine angelfish* pomacanthus, Nature, 376, (1995) pp. 765–768.
[16] A. J. Koch and H. Meinhardt, *Biological pattern formation: From basic mechanisms to complex structures*, Rev. Mod. Phys., 66 (1994), p. 1481.
[17] S. K. Kondo and T. Miura, *Reaction-diffusion model as a framework for understanding biological pattern formation*, Science, 329 (2010), pp. 1616–1620.
[18] H. Meinhardt, *Models of Biological Pattern Formation*, Vol. 6, Academic Press, London, 1982.
[19] M. I. Monteiro, S. Ahlawat, J. R. Kowalski, E. Malkin, S. P. Koushika, and P. Juoa, *The kinesin-3 family motor KLP-4 regulates anterograde trafficking of GLR-1 glutamate receptors in the ventral nerve cord of Caenorhabditis elegans*, Mol. Biol. Cell. 23 (2012), pp. 3647–3662.
[20] J. D. Murray, *Mathematical Biology.* II *Spatial Models and Biomedical Applications*, Interdiscip. Appl. Math. 18, Springer-Verlag, New York, 2001.
[21] J. M. Newby and P. C. Bressloff, *Quasi-steady state reduction of molecular motor-based models of directed intermittent search*, Bull. Math. Biol., 72 (2010), pp. 1840–1866.
[22] G. Nicolis and I. Prigogine, *Self-Organization in Nonequilibrium Systems*, Wiley-Interscience, New York, 1977.
[23] A. M. Oster and P. C. Bressloff, *A developmental model of ocular dominance formation on a growing cortex*, Bull. Math. Biol., 68, (2006), pp. 73–98.
[24] K. J. Painter, P. K. Maini, and H. G. Othmer, *Stripe formation in juvenille* Pomacathus *explained by a generalized Turing mechanism with chemotaxis*, Proc. Natl. Acad. Sci. USA, 96 (1999), pp. 5549–5554.
[25] E. M. Rauch and M. M. Millonas, *The role of trans-membrane signal transduction in Turing-type cellular pattern formation*, J. Theoret. Biol. 226 (2004), pp. 401–407.
[26] C. Rongo and J. M. Kaplan, *CaMKII regulates the density of central glutamatergic synapses in vivi,* Nature, 402 (1999), pp. 195–199.
[27] B. Sandstede and A. Scheel, *Absolute and convective instabilities of waves on unbounded and large bounded domains,* Phys. D, 145 (2000), pp. 233–277.
[28] R. A. Satnoianu, M. Menzinger, and P. K. Maini, *Turing instabilities in general systems,* J. Math. Biol., 41 (2000), pp. 493–512.
[29] R. A. Satnoianu and M. Menzinger, *Non-Turing stationary patterns in flow-distributed oscillators with general diffusion and flow rates,* Phys. Rev. E, 62 (2000), pp. 113–119.
[30] R. A. Satnoianu, P. K. Maini, and M. Menzinger, *Parameter space analysis, pattern sensitivity and model comparison for Turing and stationary flow-distributed waves (FDS),* Phys. D, 160 (2001), pp. 79–102.
[31] K. Shen and T. Meyer, *Dynamic control of CaMKII translocation and localization in hippocampal neurons by NMDA receptor stimulation*, Science, 284 (1999), pp. 162–166.
[32] J. A. Sherratt, A. S. Dagbovie, and F. M. Hilker, *A mathematical biologists guide to absolute and convective instability*, Bull. Math Biol., 76 (2014), pp. 1–26.
[33] N. V. Swindale, *A model for the formulation of ocular dominance stripes*, Proc. R. Soc. Lond. B, 208 (1980), pp. 243–264.

[34] A. M. Turing, *The chemical basis of morphogenesis*, Philos. Trans. Roy. Soc. Lond. Ser. B Biol. Sci., 237 (1952), pp. 37–72.

[35] C. Varea, J. L. Aragon, and R. A. Barrio, *Confined Turing patterns in growing systems*, Phys. Rev. E, 56 (1997), pp. 1250–1253.

[36] M. Yamaguchi, E. Yoshimoto, and S. Kondo, *Pattern regulation in the stripe of zebrafish suggests an underlying dynamic and autonomous mechanism*, Proc. Natl. Acad. Sci. USA, 104 (2007), pp. 4790–3.

[37] A. Yochelis and M. Sheintuch, *Principal bifurcations and symmetries in the emergence of reaction-diffusion-advection patterns on finite domains,* Phys. Rev. E, 80 (2009), 056201.

CHAPTER 3

A TURING MECHANISM FOR HOMEOSTATIC CONTROL OF SYNAPSE DENSITY DURING *C. ELEGANS* GROWTH

The article in this chapter was originally published in Physical Review E **96**, 012413 (2017).

PHYSICAL REVIEW E **96**, 012413 (2017)

Turing mechanism for homeostatic control of synaptic density during *C. elegans* growth

Heather A. Brooks and Paul C. Bressloff
Department of Mathematics, University of Utah 155 South 1400 East, Salt Lake City, Utah 84112, USA
(Received 16 April 2017; published 21 July 2017)

We propose a mechanism for the homeostatic control of synapses along the ventral cord of *Caenorhabditis elegans* during development, based on a form of Turing pattern formation on a growing domain. *C. elegans* is an important animal model for understanding cellular mechanisms underlying learning and memory. Our mathematical model consists of two interacting chemical species, where one is passively diffusing and the other is actively trafficked by molecular motors, which switch between forward and backward moving states (bidirectional transport). This differs significantly from the standard mechanism for Turing pattern formation based on the interaction between fast and slow diffusing species. We derive evolution equations for the chemical concentrations on a slowly growing one-dimensional domain, and use numerical simulations to demonstrate the insertion of new concentration peaks as the length increases. Taking the passive component to be the protein kinase CaMKII and the active component to be the glutamate receptor GLR-1, we interpret the concentration peaks as sites of new synapses along the length of *C. elegans*, and thus show how the density of synaptic sites can be maintained.

DOI: 10.1103/PhysRevE.96.012413

I. INTRODUCTION

The dynamical processes underlying the establishment of synaptic connections during neural development are thought to be critical in learning and memory. One of the most important signaling pathways underlying the maturation, maintenance, and elimination of synapses is the interplay between type II calcium- and calmodulin-dependent protein kinase (CaMKII) and the trafficking of glutamate receptors. Since these proteins are conserved across multiple species, considerable insights into synaptic development can be obtained by studying simpler organisms, such as the nematode worm *Caenorhabditis elegans*; see Fig. 1. During larval development of *C. elegans*, the density of ventral and dorsal cord synapses containing the glutamate receptor GLR-1 is maintained despite significant changes in neurite length [1]. It is known that the coupling of synapse number to neurite length requires CaMKII and voltage-gated calcium channels, and that CaMKII regulates the active (kinesin-based) transport and delivery of GLR-1 to synapses [1–3]. However, a long outstanding problem has been identifying a possible physical mechanism involving diffusing CaMKII molecules and motor-driven GLR-1 that leads to the homeostatic control of synaptic density.

Although the above problem arises within the context of neural development, it raises a more general issue regarding self-organization in systems of actively and passively transported particles. That is, (i) the formation of a regularly spaced distribution of synaptic puncta at an early stage of development is suggestive of some form of Turing-like pattern formation and (ii) the maintenance of synaptic density as the organism grows is suggestive of "pulse or stripe insertion" in spatially periodic patterns on growing domains [4]. Following the original work of Turing [5], the traditional mechanism for spontaneous pattern formation is the interaction of two or more passively diffusing chemical species undergoing nonlinear reaction kinetics and having different rates of diffusion [6–8]. Recently, motivated by issue (i), we proposed an alternative pattern-forming mechanism [9], involving the interaction between a slowly diffusing species (e.g., CaMKII) and a rapidly advecting species (e.g., GLR-1) switching between anterograde and retrograde motor-driven transport (bidirectional transport). Using the classical Gierer and Meinhardt mechanism for reaction kinetics [10], we showed that our model supported in-phase Turing patterns on a one-dimensional domain of fixed length. Within the context of synaptogenesis in *C. elegans*, the periodically spaced concentration peaks are interpreted as the locations of synaptic puncta. (Note that Turing pattern formation based on advecting species has also been considered within the context of animal movement and chemotaxis [11]. However, in the latter case, all species are assumed to undergo bidirectional transport, and in the fast switching limit the model reduces to a traditional reaction-diffusion model for pattern formation. In our model, pattern formation cannot occur in the fast switching limit. Advection also plays a role in reaction-diffusion systems subject to active fluid flow [12].)

In this paper, we address issue (ii), namely, how is the synaptic density of *C. elegans* maintained as the worm grows? From the perspective of self-organizing systems, this corresponds to the issue of whether or not the Turing mechanism based on interacting diffusing and advecting species exhibits pulse or stripe insertion on a growing domain. We establish the latter by extending the analysis of Crampin *et al.* [4] to our diffusion-advection model, and thus provide an experimentally testable explanation for the homeostatic control of synaptic density in *C. elegans*. Our main hypothesis is that synaptogeneisis in *C. elegans* is an example of pattern formation on a growing domain, analogous to stripe insertion in patterns of skin pigmentation of the marine angelfish [13].

II. MODEL

The homeostatic control of synaptic density appears to be mediated by two distinct antagonistic effects of CaMKII; see Fig. 2. As the worm grows in size, the synaptic density along the ventral cord decreases, which tends to result in reduced synaptic excitation of the motor neurons. In this situation, the activation of CaMKII via voltage-gated calcium

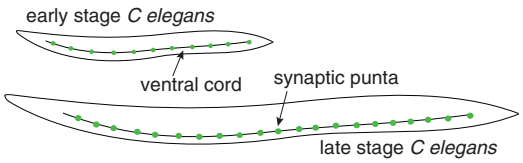

FIG. 1. Schematic figure showing distribution of synaptic punta along ventral cord of early and late stage *C. elegans*. New synapses are inserted during development to maintain the synaptic density.

channels induces the formation of new synapses by enhancing the active transport of GLR-1. On the other hand, when the synaptic density becomes too high, the corresponding increase in excitation leads to constitutive activation of CaMKII (autophosphorylation) due to the increased calcium levels. Although constitutively active CaMKII also enhances the motor-driven transport of GLR-1 along the ventral cord, it fails to localize the receptors at synaptic sites. This is consistent with the observation that the synaptic localization of CaMKII in rate changes in response to autophosphorylation [14].

To model this system, consider a one-dimensional domain of fixed length L, which represents a neurite in the ventral cord of *C. elegans* at a particular stage of larval development. Let $R(x,t)$ denote the concentration of GLR-1 receptors at position x along the cell at time t and let $C(x,t)$ denote the corresponding concentration of active CaMKII. For simplicity, no distinction is made between membrane-bound (synaptically localized) and cytoplasmic CaMKII. On the other, GLR-1 is partitioned into two subpopulations: those that undergo anterograde transport (R_+) and those that undergo retrograde transport (R_-) with $R(x,t) = R_+(x,t) + R_-(x,t)$. Individual receptors randomly switch between the two advective states according to a two-state Markov process $R_+ \frac{\beta}{\alpha} R_-$, with transition rates α,β. This yields the following system of equations [9]:

$$\frac{\partial C}{\partial t} = D\frac{\partial^2 C}{\partial x^2} + f(R_+,R_-,C), \tag{1a}$$

$$\frac{\partial R_+}{\partial t} = -v\frac{\partial R_+}{\partial x} + \alpha R_- - \beta R_+ + g(R_+,C), \tag{1b}$$

$$\frac{\partial R_-}{\partial t} = v\frac{\partial R_-}{\partial x} + \beta R_+ - \alpha R_- + g(R_-,C). \tag{1c}$$

Here D is the CaMKII diffusion coefficient and v is the speed of motor-driven GLR-1. The reaction term $f(R_+,R_-,C)$ represents both the self-activation of CaMKII and the inhibition of CaMKII by GLR-1. (In a more detailed model, one could consider synaptic rather than cytoplasmic GLR-1 inhibiting synaptic rather than cytoplasmic CaMKII.) The reaction terms $g(R_\pm,C)$ represents the increase in actively-transported GLR-1 due to the action of CaMKII, which is taken to be symmetric with regards anterograde and retrograde transport. Equations (1) are supplemented by reflecting boundary conditions at the ends $x = 0,L$:

$$\left.\frac{\partial C(x,t)}{\partial x}\right|_{x=0,L} = 0, \tag{2a}$$

$$vR_+(0,t) = vR_-(0,t), \quad vR_+(L,t) = vR_-(L,t). \tag{2b}$$

For simplicity, we will take $\alpha = \beta$ in the following.

It remains to specify the form of the chemical interaction functions f and g. The precise details of the interactions between CaMKII and GLR-1 are currently unknown. Therefore, we choose the simplest model that can capture the activation of GLR-1 transport and delivery by CaMKII and the inhibition (synapse removal) of CaMKII by GLR-1 and the autophosphorylation properties of CaMKII. Another requirement is that the nonlinear interactions yield Turing patterns for which the peaks of the various concentrations are in-phase. Hence, following our previous work [9], we take the classical activator-inhibitor system due to Gierer and Meinhardt (GM) [10]:

$$f(R_+,R_-,C) = \rho_1\frac{C^2}{R_+ + R_-} - \mu_1 C + \gamma, \tag{3a}$$

$$g(R,C) = \rho_2 C^2 - \mu_2 R. \tag{3b}$$

Here ρ_1,ρ_2 represent the strength of interactions, μ_1 and μ_2 are the respective decay rates, and γ is the production rate of CaMKII. To justify the trafficking-based mechanism for pattern formation in *C. elegans*, the conditions for Turing instability must be satisfied for biophysically relevant parameters. Many of these parameters can be cited from the biological literature. First, we require $\mu_1 < \mu_2$ for stability in the homogeneous steady state in this system; this is satisfied because the decay rate of GLR-1 is approximately four times that of CaMKII [15]. For our simulations (see Sec. III), we

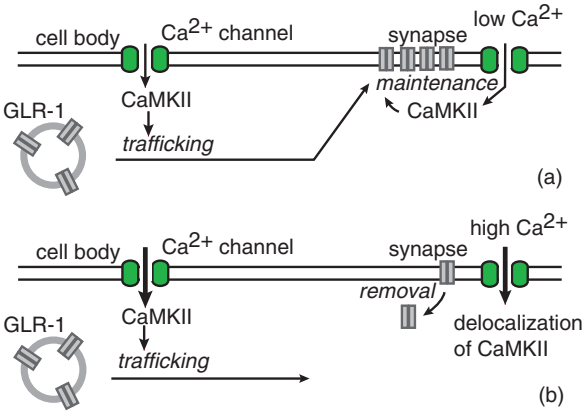

FIG. 2. Regulation of transport and delivery of GLR-1 to synapses by CaMKII. (a) Calcium influx through voltage-gated calcium channels activates CaMKII, which enhances the active transport and delivery of GLR-1 to synapses. (b) Under conditions of increased excitation, higher calcium levels results in constitutively active CaMKII which fails to localize at synapses, leading to the removal of GLR-1 from synapses.

take $\mu_1 = 0.25/\text{s}$ and $\mu_2 = 1/\text{s}$. Additionally, data on the transport of GLR-1 via molecular motors suggest an average velocity along the ventral cord is 1 μm/s, with an average run length of 9.2 μm [16]. From this, we infer a switching rate of $\alpha \approx 0.11/\text{s}$. We take diffusion of CaMKII to be 0.01 $\mu\text{m}^2/\text{s}$ and production rate to be $\gamma = 0.02\ \mu M/\text{s}$. Finally, we set the strength of interaction parameters to be $\rho_1 = 1/\text{s}$ and $\rho_2 = 1/(\mu M\ \text{s})$.

III. PATTERN FORMATION ON A GROWING DOMAIN

Previously, we used linear stability analysis to derive conditions for a Turing instability, and confirmed numerically that spatially periodic patterns emerge beyond the Turing bifurcation point [9]. In particular, we found that $\gamma = \alpha D/v^2$ has to be sufficiently small for patterns to emerge. One consequence is that patterns emerge outside the parameter regime of fast switching (large α), where the linearized model reduces to a two-component reaction-diffusion system. Here we investigate pattern formation on a slowly growing 1D domain, $0 < x < L(t)$, where $L(t)$ is the increasing length of the domain. The basic idea is that $L(t)$ represents the length of *C. elegans* at a time t during development, following an initial phase of synaptogenesis at time $t = 0$. This means that the model system is already operating beyond the Turing bifurcation point identified in our previous paper [9]. If we interpret the in-phase peaks of CaMKII and GLR-1 as synaptic sites, then the wavelength of the pattern at time $t = 0$ is equivalent to the spacing of the newly formed synapses. This suggests that under uniform growth of the domain for $t > 0$, the spacing of the synapses will increase. Therefore, to obtain a similar synaptic density in the adult as in the first stages of synaptiogenesis, it is necessary for new synaptic puncta to be formed. From the mathematical perspective, this can be interpreted as stripe insertion of a Turing pattern on a growing domain.

In light of the above, consider the system of advecting and diffusing particles (1) on the growing domain $0 < x < L(t)$. Following previous studies of diffusion processes on growing domains [4], we model domain growth in terms of a velocity field u such that $x \to x + u(x,t)\Delta t$ over the time interval $[t, t + \Delta t]$. We will assume spatially uniform growth by taking $\partial_x u = \sigma(t)$, which implies that

$$u(x,t) = \frac{x}{L(t)}\frac{dL(t)}{dt}. \tag{4}$$

Let $X \in [0, L_0]$ be the local coordinate system at the initial length L_0. Using a Lagrangian description, we can then represent spatial position at time t as

$$x = \Lambda(X,t) \equiv \frac{XL(t)}{L_0}, \quad L(0) = L_0.$$

To derive the evolution equations on a growing domain, let us focus on the diffusing component $C(x,t)$; the other components can be treated in a similar fashion. Consider the particle conservation equation

$$\frac{d}{dt}\int_0^{L(t)} C(x,t)dx = \int_0^{L(t)}\left[-\frac{\partial J(x,t)}{\partial x} + f\right]dx, \tag{5}$$

with $J(x,t) = -D\frac{\partial C(x,t)}{\partial x}$. Using the Reynold's transport theorem, the left-hand side becomes

$$\frac{d}{dt}\int_0^{L(t)} C(x,t)dx = \int_0^{L(t)}\left[\frac{\partial C(x,t)}{\partial t} + \frac{\dot{L}(t)}{L(t)}\frac{\partial [xC(x,t)]}{\partial x}\right]dx.$$

We thus obtain the following evolution equation for C on $0 < x < L(t)$:

$$\frac{\partial C}{\partial t} + \frac{\dot{L}(t)}{L(t)}\frac{\partial [xC]}{\partial x} = D\frac{\partial^2 C}{\partial x^2} + f. \tag{6}$$

Finally, we transform Eq. (6) to the fixed interval $[0, L_0]$ by performing the change of variables $x \to X = (xL_0)/L(t)$. Under this transformation the advection term in Eq. (6) is eliminated and we obtain the modified evolution equation,

$$\frac{\partial C}{\partial t} = \frac{D}{L(t)^2}\frac{\partial^2 C}{\partial x^2} - \left(\frac{\dot{L}}{L}\right)C + f(R_+, R_-, C). \tag{7a}$$

Applying a similar analysis to the advecting variables $R_\pm(x,t)$, with fluxes $J_\pm(x,t) = \mp v R_\pm$ and $f(R_+, R_-, C)$ replaced by $\pm(\alpha R_- - \beta R_+) + g(R_\pm, C)$, we derive the following evolution equations on $[0, L_0]$:

$$\frac{\partial R_+}{\partial t} = -\frac{v}{L(t)}\frac{\partial R_+}{\partial x} - \left(\frac{\dot{L}}{L}\right)R_+ + \alpha R_- - \beta R_+ + g(R_+, C) \tag{7b}$$

$$\frac{\partial R_-}{\partial t} = \frac{v}{L(t)}\frac{\partial R_-}{\partial x} - \left(\frac{\dot{L}}{L}\right)R_- + \beta R_+ - \alpha R_- + g(R_-, C). \tag{7c}$$

In the above equations, we have fixed the length-scale by setting $L_0 = 1$.

Equations (7a)–(7c) and (3a), (3b) are the starting point for our investigation of Turing pattern formation on a growing domain of length $L(t)$. Following Ref. [4], we make one further simplification by noting that for sufficiently slow growth, the terms involving the dilution factor $-\dot{L}(t)/L(t)$ are small compared to the remaining terms and can be neglected. It is reasonable to assume slow growth for *C. elegans*, since the larvae grow to the adult stage at an average rate of around 10^{-3} μm/s [17]. For the sake of illustration, we will assume logistic growth [4],

$$L(t) = e^{rt}\left[1 + \frac{1}{\Lambda_0}(e^{rt} - 1)\right]^{-1}, \tag{8}$$

with $r = 0.001$ μm/s and $\Lambda_0 = 10$. With this choice of growth function, a section of the ventral cord grows from 10 μm to 100 μm in 2 h. Although we choose this logistic growth function because it represents the physical growth during *C. elegans* development, similar results are obtained for other choices of growth functions (such as exponential or linear).

In our numerical simulations, we assume that the system of evolution equations operates beyond the Turing bifurcation point for pattern formation at the initial length L_0. The initial concentrations are chosen from a uniform random distribution

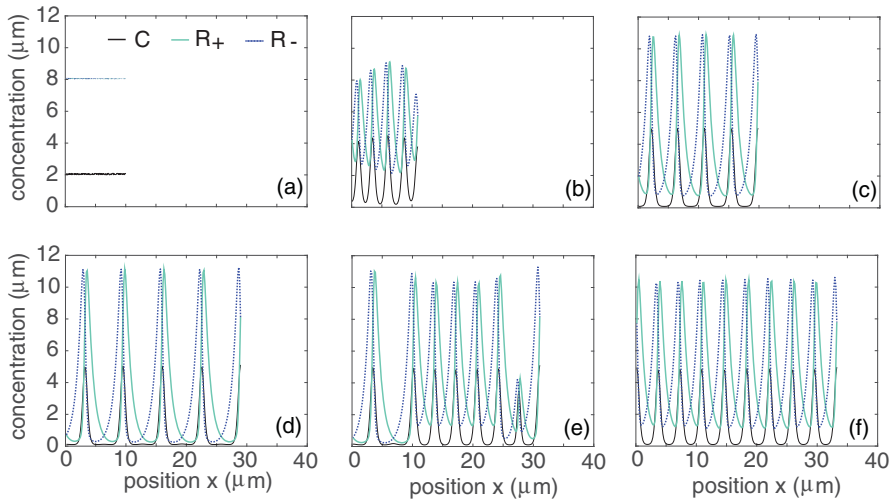

FIG. 3. Numerical simulations showing temporal evolution of the concentrations $C, R_\pm$ on a slowly growing domain. (a) $t = 0$ s; (b) $t = 100$ s; (c) $t = 850$ s; (d) $t = 1300$ s; (e) $t = 1400$ s; (f) $t = 1500$ s. Initial concentrations are taken to be random fluctuations about steady-state values. A spatially periodic pattern is becoming established with five potential synapse sites by $t = 100$ s, and as the domain continues to grow, the synapse sites begin to spread out. At $t = 1300$ s, we can see the beginnings of pattern reorganization between the synapse sites as CaMKII concentrations start to grow there. New peaks are inserted after the second, third, and fourth existing synapse sites by $t = 1400$ s; the beginnings of a new CaMKII peak can also be observed between the first and second peak. Numerical simulations were performed using a combination of Crank-Nicolson and Lax-Wendroff schemes, with no flux boundary conditions. Full solutions were computed in the Lagrangian coordinate system, and then converted back into physical coordinates. We take space step $dx = 0.05$ and time step $dt = 0.025$. The 1D domain grows with growth parameters $r = 0.001$ μm/s and $\Lambda_0 = 10$. Other parameters are $\rho_1 = 1/\text{s}$, $\rho_2 = 1/(\mu M\,\text{s})$, $\mu_1 = 0.25/\text{s}$, $\mu_2 = 1/\text{s}$, $\alpha = 0.11/\text{s}$, $D = 0.01$ $\mu\text{m}^2/\text{s}$, $\gamma = 0.02$ $\mu M/\text{s}$, and $v = 1$ μm/s.

near fixed point values of the spatially uniform equations. Example plots showing the evolution of the concentrations $C, R_\pm$ are shown in Fig. 3. As the system evolves, we initially observe growth of the concentration C of the diffusive component, and then patterns emerge as the activator is eventually tempered by increase of the advecting inhibitors $R_\pm$. In this case, the concentration of both activating and inhibiting species are in phase with each other. Once the pattern is established, it persists as the domain length increases, with areas of high concentration slowly growing farther apart. As the areas of high concentration become sufficiently separated, the pattern becomes reorganized and we see the emergence of new peaks.

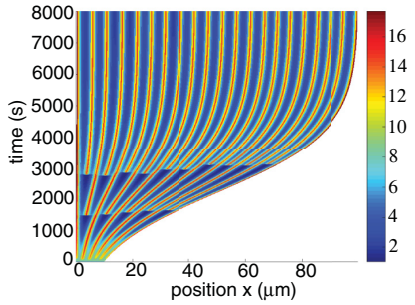

FIG. 4. Space-time plot showing the insertion of new potential synaptic sites as the domain representing a section of the ventral cord grows over the course of 2.5 h. The horizontal axis represents position along the *C. elegans* ventral cord and the vertical axis represents time in seconds. Colors represent local concentration of GLR-1 (a combined total of both leftward and rightward trafficking species) in μM. Areas of high concentration represent potential synapse sites. Numerical simulations and parameter values are as in Fig. 3.

Having established that the Turing mechanism based on interacting advecting and diffusing species supports pulse-insertion on a growing domain, we can now relate our results to the particular problem of homeostatic control of synaptic density in *C. elegans*. That is, interpreting C and $R_\pm$ as concentrations of CaMKII and GLR-1, respectively, we can interpret the peaks in concentration as synaptic sites. Hence, the insertion of additional peaks as the domain grows provides a mechanism for maintaining synaptic density. This is illustrated in Fig. 4, which shows a space-time plot of CaMKII and GLR-1 concentrations in a growing domain. For the given parameter values, our results match well the experimental observations of Rongo and Kaplan [1], who found that *C. elegans* synaptic density is maintained.

IV. DISCUSSION

In summary, we have shown how an active trafficking-based mechanism for Turing pattern formation on a 1D growing domain can account for the homeostatic regulation of synapses in *C. elegans* during development. While the important role of CaMKII in regulating the delivery of GLR-1 to synapses along the ventral cord of *C. elegans* is well known, the detailed mechanisms regarding their interactions are still unclear. In future modeling work, it will

be necessary to develop a more detailed biophysical model of CaMKII-GLR-1 coupling, and to distinguish between membrane-bound versus cytoplasmic CaMKII. Nevertheless, our simple model can provide experimentally testable predictions, particularly with regard the spacing of synaptic puncta. For example, linear stability analysis can determine the wavelength of emerging patterns as a function of various biophysical parameters such as the diffusivity of CaMKII, the speed and switching rates of molecular motors, and the rate of CaMKII phosphorylation. Our model predicts that manipulation of these parameters should change the synaptic spacing. On the other hand, the insertion of new puncta should persist.

From the more general perspective of self-organizing systems, our model provides a new paradigm for exploring pattern-forming dynamical systems, based on nonlinear interactions between distinct advecting and diffusing species. Although our model involved molecular species, one could equally well consider population models of animal species. One obvious extension would be to analyze the generation of patterns in higher spatial dimensions. In the case of the neurites in *C. elegans*, the microtubles tend to be aligned in parallel so that one can treat the active transport process as effectively 1D. On the other hand, intracellular transport within most non–polarized animal cells occurs along a microtubular network projecting radially from an organizing centers or centrosomes [18]. It has been found that microtubules bend due to large internal stresses, resulting in a locally disordered network, suggesting that *in vivo* transport on relatively short length scales may be similar to transport observed *in vitro*, where microtubular networks are not grown from a centrosome and thus exhibit orientational and polarity disorder [19,20]. If the network is sufficiently dense, then to a first approximation one can assume that the set of velocity states (and associated state transitions) available to an active particle is independent of position. This means that one can effectively represent active transport within the cell in terms of a two- or three-dimensional velocity jump process [21–23], which is analogous to an animal movement model with a turning function [24,25]. One of the interesting features of higher dimensional models, is that one has to use weakly nonlinear analysis to derive amplitude equations for the emerging patterns close to the Turing bifurcation point, to investigate the selection and stability of patterns (rolls, rhomboids, and hexagons).

[1] C. Rongo and J. M. Kaplan, Nature **402**, 195 (1999).
[2] F. J. Hoerndli, D. A. Maxfield, P. J. Brockie, J. E. Mellem, E. Jensen, R. Wang, D. M. Madsen, and A. V. Maricq, Neuron **80**, 1421 (2013).
[3] F. J. Hoerndli, R. Wang, J. E. Mellem, A. Kallarackal, P. J. Brockie, C. Thacker, E. Jensen, D. M. Madsen, and A. V. Maricq, Neuron **86**, 457 (2015).
[4] E. J. Crampin, E. A. Gaffney, and P. K. Maini, Bull. Math. Biol. **61**, 1093 (1999).
[5] A. M. Turing, Philos. Trans. R. Soc. B **237**, 37 (1952).
[6] A. J. Koch and H. Meinhardt, Rev. Mod. Phys. **66**, 1481 (1994).
[7] J. D. Murray, *Mathematical Biology. II Spatial Models and Biomedical Applications*, Interdisciplinary Applied Mathematics Vol. 18 (Springer-Verlag, New York, 2001).
[8] D. Walgraef, *Pattern Formation with Examples from Physics, Chemistry, and Materials Science* (Springer-Verlag, New York, 1997).
[9] H. A. Brooks and P. C. Bressloff, SIAM J. Appl. Dyn. Syst. **15**, 1823 (2016).
[10] A. Gierer and H. Meinhardt, Kybernetik **12**, 30 (1972).
[11] T. Hillen, J. Math. Biol. **35**, 49 (1996).
[12] J. S. Bois, F. Julicher, and S. W. Grill, Phys. Rev. Lett. **106**, 028103 (2011).
[13] S. Kondo and R. Asai, Nature **376**, 765 (1995).
[14] K. Shen and T. Meyer, Science **284**, 162 (1999).
[15] C. Hanus and E. M. Schuman, Nat. Rev. Neurosci. **14**, 638 (2013).
[16] M. I. Monteiro, S. Ahlawat, J. R. Kowalski, E. Malkin, S. P. Koushika, and P. Juoa, Mol. Biol. Cell. **23**, 3647 (2012).
[17] J. E. Sulston and H. R. Horvitz, Dev. Biol. **56**, 110 (1977).
[18] P. C. Bressloff, *Stochastic Processes in Cell Biology* (Springer, Berlin, 2014).
[19] A. Kahana, G. Kenan, M. Feingold, M. Elbaum, and R. Granek, Phys. Rev. E **78**, 051912 (2008).
[20] H. Salman, A. Abu-Arish, S. Oliel, A. Loyter, J. Klafter, R. Granek, and M. Elbaum, Biophys. J. **89**, 2134 (2005).
[21] O. Bénichou, C. Loverdo, M. Moreau, and R. Voituriez, J. Phys.: Condens. Matter **19**, 065141 (2007).
[22] C. Loverdo, O. Benichou, M. Moreau, and R. Voituriez, Phys. Rev. E **80**, 031146 (2009).
[23] P. C. Bressloff and J. M. Newby, Phys. Rev. E **83**, 061139 (2011).
[24] T. Hillen and H. G. Othmer, SIAM J. Appl. Math. **61**, 751 (2000).
[25] T. Hillen and A. Swan, in *Mathematical Models and Methods for Living Systems*, edited by L. Preziosi *et al.*, (Springer, Berlin, 2016), pp. 73–129.

CHAPTER 4

MATHEMATICAL ANALYSIS OF PATTERN FORMATION IN REACTION-TRANSPORT MECHANISMS

The mathematical model for pattern formation due to reaction-transport mechanisms discussed in Chapters 2 and 3 was originally formulated in the context of synapse density maintenance in *C. elegans*. However, analysis of this mechanism leads to some natural mathematical extensions. In this chapter, we discuss two of these extensions. In Section 4.1, we use weakly nonlinear analysis to determine stability conditions for one-dimensional patterns arising due to this mechanism. In Section 4.2, we develop a two-dimensional analog of the reaction transport model. Future work on analysis of pattern formation in the two-dimensional reaction transport mechanism is discussed in Section 4.2.2.

4.1 Weakly nonlinear analysis for the one-dimensional reaction-transport mechanism

4.1.1 The one-dimensional model

For the purposes of clarity and to standardize notation for this chapter, we will briefly review the one-dimensional reaction-transport model in this section. Let $\mathcal{A}(x,t)$ represent the concentration of actively transported particles at position $x \in \mathbb{R}$ at time t; likewise, $P(x,t)$ will denote the corresponding concentration of passively transported particles. Passively transported (PT) particles undergo diffusion with constant diffusion coefficient D. Actively transported (AT) particles undergo bidirectional transport and travel with constant velocity states $\pm v_{\pm}$. The AT particles are partitioned into two subpopulations: those that undergo anterograde (rightward) transport with positive velocity v_+, represented by density $A_+(x,t)$, and those that undergo retrograde (leftward) transport with negative velocity $-v_-$ with density $A_-(x,t)$:

$$\mathcal{A}(x,t) = A_+(x,t) + A_-(x,t). \tag{4.1}$$

As the active transport is bidirectional, we allow these AT particles to switch between the constant velocity states according to the two-state Markov process with switching rate α.

Therefore, this system is described by the following system of PDEs:

$$\frac{\partial P}{\partial t} = D\frac{\partial^2 p}{\partial x^2} + f(P, \mathcal{A}), \tag{4.2a}$$

$$\frac{\partial A_+}{\partial t} = -v_+\frac{\partial A_+}{\partial x} - \alpha A_+ + \alpha A_- + \frac{1}{2}g(P, \mathcal{A}) \tag{4.2b}$$

$$\frac{\partial A_-}{\partial t} = v_-\frac{\partial A_-}{\partial x} + \alpha A_+ - \alpha A_- + \frac{1}{2}g(P, \mathcal{A}), \tag{4.2c}$$

where f and g are the nonlinear reaction terms that are functions of PT and AT concentration.

4.1.2 Weakly nonlinear stability analysis

Suppose that there exists a spatially uniform fixed point (P^*, A_+^*, A_-^*) for which

$$f(P^*, \mathcal{A}^*) = g(P^*, \mathcal{A}^*) = 0 \text{ and } A_\pm^* = A^*.$$

Linearizing about this fixed point by setting

$$P(x,t) = P^* + p(x,t), \quad A_\pm(x,t) = A^* + a_\pm(x,t)$$

yields the system of linear equations

$$\frac{\partial p}{\partial t} = D\frac{\partial^2 p}{\partial x^2} + f_1 p + f_2(a_+ + a_-) \tag{4.3a}$$

$$\frac{\partial a_+}{\partial t} = -v\frac{\partial a_+}{\partial x} - \alpha a_+ + \alpha a_- + g_1 p + g_2(a_+ + a_-) \tag{4.3b}$$

$$\frac{\partial a_-}{\partial t} = v\frac{\partial a_-}{\partial x} + \alpha a_+ - \alpha a_- + g_1 p + g_2(a_+ + a_-). \tag{4.3c}$$

Here $f_1 = \partial f/\partial P$, $f_2 = \partial f/\partial_{\mathcal{A}}$ and similarly for $g_{1,2}$, with all derivatives evaluated at the fixed point. Setting $p(x,t) = pe^{\lambda t + ikx}$, etc., then yields the following equations for the continuous spectrum $\lambda = \lambda(k)$ with $k \in \mathbb{R}$:

$$\lambda p = (f_1 - Dk^2)p + f_2(a_+ + a_-) \tag{4.4a}$$

$$\lambda a_+ = (-ikv - \alpha + g_2)a_+ + (\alpha + g_2)a_- + g_1 p \tag{4.4b}$$

$$\lambda a_- = (ikv - \alpha + g_2)a_- + (\alpha + g_2)a_+ + g_1 p. \tag{4.4c}$$

In general, for each value of k, there will be three eigenvalues $\lambda_j(k), j = 1,2,3$, one of which will be real and the other two either are real or form a complex conjugate pair.

There are thus three solution branches or dispersion curves. Necessary conditions for a Turing instability are as follows:

(i) $\mathrm{Re}[\lambda(0)] < 0$ (fixed point is linearly stable with respect to homogeneous perturbations);
(ii) There exists a critical wavenumber k_c such that for one of the branches

$$\max_{k\in\mathbb{R}}\{\mathrm{Re}[\lambda(k)]\} = \mathrm{Re}[\lambda(k_c)] = \lambda(k_c) = 0;$$

(iii) $\lambda(k)$ is real in a neighborhood of the critical point (excludes a Turing-Hopf bifurcation).

In our previous work discussed in Chapter 2 we proved that all of these conditions are satisfied provided that [7]

$$\gamma \equiv \frac{\alpha D}{v^2} < -\frac{f_1}{4g_2} < \frac{1}{2}, \quad g_2 < 0, \quad f_1 > 0, \quad f_2 g_1 < 0. \tag{4.5}$$

At the critical point, the fixed point is marginally stable with respect to excitation of a spatially periodic pattern of critical wavelength $2\pi/k_c$. Typically, varying one of the parameters of the underlying model can then push the associated real dispersion curve $\lambda = \lambda(k)$ above zero in a neighborhood of k_c, resulting in a Turing instability. Whether or not a stable periodic pattern forms then depends on the nonlinearities of the system, which can be investigated numerically or using weakly nonlinear analysis, as discussed below.

Let us now focus on the real solution branch of equations (4.4), which we simply denote by $\lambda(k)$, and take p to be real. It immediately follows from equation (4.4a) that $a_+ + a_-$ is also real. Adding equations (4.4b,c) then establishes that $a_+ - a_-$ has to be pure imaginary and, hence, $a_+ = a = \overline{a}_-$, where $\overline{a}$ denotes the complex conjugate (c. c.) of a. It follows that the bifurcating planform $\mathbf{u}(x,t)$ takes the form

$$\mathbf{u}(x,t) = \mathrm{e}^{\lambda(k)t}\begin{pmatrix} 1 \\ a(k) \\ \overline{a}(k) \end{pmatrix}\left[z\mathrm{e}^{ikx} + \text{ c . c.}\right], \tag{4.6}$$

where we have set $p(k) = z \in \mathbb{C}$, and $a(k) = u(k) + iv(k)$ with

$$u(k) = \frac{\lambda(k) + D(k^2) - f_1}{2f_2}, \quad v(k) = \frac{kv}{\lambda(k) + 2\alpha}u(k). \tag{4.7}$$

As amplitude z grows the linear approximation breaks down and the nonlinearities dominate. We can use weakly nonlinear theory to investigate the selection and stability of patterns in this regime. Denoting $\gamma = \gamma_c$ as the bifurcation point where the homogeneous

state becomes unstable, we seek to define a small parameter $\gamma - \gamma_c = \epsilon\Delta\gamma < 0$ sufficiently close to this bifurcation point. The dominant behavior just beyond this bifurcation point is the slow growth of the mode $e^{\epsilon\Delta\gamma t}$, so it is justified to introduce a slow timescale $\tau = \epsilon t$. We proceed to derive amplitude equations for $z(\tau)$.

First, assuming the nonlinear reaction terms are sufficiently smooth, we can Taylor expand the nonlinearities f, g locally about the steady state $p^*, \mathcal{A}^*$.

$$f(p,\mathcal{A}) = f(p^*,\mathcal{A}^*) + f_1\Delta p + f_2\Delta\mathcal{A} + \frac{1}{2}\left[f_{11}\Delta p^2 + 2f_{12}\Delta p\Delta\mathcal{A} + f_{22}\Delta\mathcal{A}^2\right] \tag{4.8}$$

$$+ \frac{1}{6}\left[f_{111}\Delta p^3 + 3f_{112}\Delta p^2\Delta\mathcal{A} + 3f_{122}\Delta p\Delta\mathcal{A}^2 + f_{222}\Delta\mathcal{A}^3\right] + \dots \tag{4.9}$$

where $\Delta p = p - p^*, \Delta\mathcal{A} = \mathcal{A} - \mathcal{A}^*$ and we use the notation $f_1 = \frac{\partial f}{\partial p}, f_{22} = \frac{\partial^2 f}{\partial \mathcal{A}^2}$, etc., all evaluated at the fixed point. Note that g has a similar expansion, namely

$$g(p,\mathcal{A}) = g(p^*,\mathcal{A}^*) + g_1\Delta p + g_2\Delta\mathcal{A} + \frac{1}{2}\left[g_{11}\Delta p^2 + 2g_{12}\Delta p\Delta\mathcal{A} + g_{22}\Delta\mathcal{A}^2\right] \tag{4.10}$$

$$+ \frac{1}{6}\left[g_{111}\Delta p^3 + 3g_{112}\Delta p^2\Delta\mathcal{A} + 3g_{122}\Delta p\Delta\mathcal{A}^2 + g_{222}\Delta\mathcal{A}^3\right] + \dots. \tag{4.11}$$

Once again, we represent the partial derivatives evaluated at the fixed point as $g_1 = \frac{\partial g}{\partial p}, g_{22} = \frac{\partial^2 g}{\partial \mathcal{A}^2}$, and so on.

We apply the following perturbation expansion, seeking solutions of the form

$$p(x,t) = p^* + \epsilon^{1/2}p_1 + \epsilon p_2 + \epsilon^{3/2}p_3 + \dots \tag{4.12}$$

$$a_+(x,t) = a_+^* + \epsilon^{1/2}a_{+1} + \epsilon a_{+2} + \epsilon^{3/2}a_{+3} + \dots \tag{4.13}$$

$$a_-(x,t) = a_-^* + \epsilon^{1/2}a_{-1} + \epsilon a_{-2} + \epsilon^{3/2}a_{-3} + \dots \tag{4.14}$$

We also set $\mathcal{A}_n = a_{+n} + a_{-n}$. For the next step, we make the following substitutions. First, we substitute in each of the perturbed solutions from Equations 4.14. We combine this with the Taylor expansions of $f(p,\mathcal{A})$ (given in Equation 4.9) and $g(p,\mathcal{A})$ (given in Equation 4.11) into the linearized system represented by Equations 4.3.

Plugging these expansions into the full system yields

$$\begin{aligned}
\epsilon\partial_\tau(p^* + \epsilon^{1/2}p_1 + \epsilon p_2 + \epsilon^{3/2} + \dots) &= (\gamma_c + \epsilon\Delta\gamma)\partial_{xx}(p^* + \epsilon^{1/2}p_1 + \epsilon p_2 + \dots) \\
&\quad + f(p, \mathcal{A}) \\
\epsilon\partial_\tau(a_+^* + \epsilon^{1/2}a_{+1} + \epsilon a_{+2} + \epsilon^{3/2}a_{+3} + \dots) &= -\partial_x(a_+^* + \epsilon^{1/2}a_{+1} + \epsilon a_{+2} + \epsilon^{3/2}a_{+3} + \dots) \\
&\quad + (a_-^* + \epsilon^{1/2}a_{-1} + \epsilon a_{-2} + \epsilon^{3/2}a_{-3}...) \\
&\quad - (a_+^* + \epsilon^{1/2}a_{+1} + \epsilon a_{+2} + \epsilon^{3/2}a_{+3} + \dots) \\
&\quad + g(p, \mathcal{A}) \\
\epsilon\partial_\tau(a_-^* + \epsilon^{1/2}a_{-1} + \epsilon a_{-2} + \epsilon^{3/2}a_{-3} + \dots) &= \partial_x(a_-^* + \epsilon^{1/2}a_{-1} + \epsilon a_{-2} + \epsilon^{3/2}a_{-3} + \dots) \\
&\quad + (a_+^* + \epsilon^{1/2}a_{+1} + \epsilon a_{+2} + \epsilon^{3/2}a_{+3} + \dots) \\
&\quad - (a_-^* + \epsilon^{1/2}a_{-1} + \epsilon a_{-2} + \epsilon^{3/2}a_{-3} + \dots) \\
&\quad + g(p, \mathcal{A}),
\end{aligned}$$

where the Taylor expansions listed above can be substituted in for f, g, along with the appropriate perturbed solutions.

Next, we collect terms according to their power in ϵ. The $\mathcal{O}(1)$ terms give us the steady state equations

$$\begin{aligned}
0 &= \gamma_c\partial_{xx}p^* + f(p^*, \mathcal{A}^*) \\
0 &= -\partial_x a_+^* + a_-^* - a_+^* + g(p^*, \mathcal{A}^*) \\
0 &= \partial_x a_+^* + a_+^* - a_-^* + g(p^*, \mathcal{A}^*).
\end{aligned}$$

The $\mathcal{O}(\epsilon^{1/2})$ equations are

$$\begin{aligned}
0 &= \gamma_c\partial_{xx}p_1 + f_1 p_1 + f_2\mathcal{A}_1 \\
0 &= -\partial_x a_{+1} + a_{-1} - a_{+1} + g_1 p_1 + g_2\mathcal{A}_1 \\
0 &= \partial_x a_{-1} + a_{+1} - a_{-1} + g_1 p_1 + g_2\mathcal{A}_1,
\end{aligned}$$

which is the homogeneous linear problem

$$\mathcal{L}\boldsymbol{u}_1 = 0$$

where

$$\mathcal{L} = \begin{pmatrix} \gamma_c\frac{\partial^2}{\partial x^2} + f_1 & f_2 & f_2 \\ g_1 & -\frac{\partial}{\partial x} - 1 + g_2 & 1 + g_2 \\ g_1 & 1 + g_2 & \frac{\partial}{\partial x} - 1 + g_2 \end{pmatrix},$$

which has solutions

$$\boldsymbol{u}_1 = \begin{pmatrix} 1 \\ a(k) \\ \bar{a}(k) \end{pmatrix} z\mathrm{e}^{ikx} + \text{ c . c.}$$

In particular,

$$p_1 = z\mathrm{e}^{ikx} + \bar{z}\mathrm{e}^{-ikx}, \quad \mathcal{A}_1 = (a + \bar{a})(z\mathrm{e}^{ikx} + \bar{z}\mathrm{e}^{-ikx}).$$

Now we examine the $\mathcal{O}(\epsilon)$ equations, which take the form

$$\mathcal{L}\boldsymbol{u}_2 = \mathbf{F_2}, \tag{4.15}$$

where

$$\mathbf{F_2} = -\frac{1}{2}\begin{pmatrix} f_{11}p_1^2 + f_{22}\mathcal{A}_1^2 + 2f_{12}p_1\mathcal{A}_1 \\ g_{11}p_1^2 + g_{22}\mathcal{A}_1^2 + 2g_{12}p_1\mathcal{A}_1 \\ g_{11}p_1^2 + g_{22}\mathcal{A}_1^2 + 2g_{12}p_1\mathcal{A}_1 \end{pmatrix}. \tag{4.16}$$

We can derive solvability conditions for these amplitude equations by applying the Fredholm alternative, which tells us that $\mathcal{L}\boldsymbol{u}_2 = \mathbf{F_2}$ has a solution $\boldsymbol{u}_2$ i.f.f. $\langle \tilde{\boldsymbol{u}}, F_2 \rangle = 0$, where $\tilde{\boldsymbol{u}} \in Ker(\mathcal{L}^\dagger)$, with $\mathcal{L}^\dagger$ the adjoint of $\mathcal{L}$. In contrast with a classical reaction-diffusion system, it is important to note that $\mathcal{L}$ is not self adjoint. One can find the adjoint (at least formally) by applying integration by parts. For this problem, we need to consider a large (but finite) domain $x \in [-L, L]$ with periodic boundary conditions such that $\boldsymbol{u}(-L,t) = \boldsymbol{u}(L,t)$ and $\boldsymbol{u}_x(-L,t) = \boldsymbol{u}_x(L,t)$. Suppose $\boldsymbol{u}$ and $\boldsymbol{w}$ both satisfy these conditions. Then, if $\mathcal{L}^\dagger$ is the adjoint of $\mathcal{L}$, it must be true that

$$\langle \mathcal{L}\boldsymbol{u}, \boldsymbol{w} \rangle = \langle \boldsymbol{u}, \mathcal{L}^\dagger \boldsymbol{w} \rangle,$$

with inner product

$$\langle \boldsymbol{u}, \boldsymbol{w} \rangle = \frac{1}{2L}\int_{-L}^{L} (\boldsymbol{u} \cdot \mathbf{w}) dx.$$

Writing this out and applying integration by parts, we can show that

$$\mathcal{L}^\dagger = \begin{pmatrix} \gamma\frac{\partial^2}{\partial x^2} + f_1 & f_2 & f_2 \\ g_1 & \frac{\partial}{\partial x} - 1 + g_2 & 1 + g_2 \\ g_1 & 1 + g_2 & -\frac{\partial}{\partial x} - 1 + g_2 \end{pmatrix}. \tag{4.17}$$

It is straightforward to find $Ker(\mathcal{L}^\dagger)$, which is spanned by $(\widetilde{u}, \overline{\widetilde{u}})$ with

$$\tilde{u} = \begin{pmatrix} 1 \\ \bar{a} \\ a \end{pmatrix} e^{-ikx}. \tag{4.18}$$

We note here that the solvability condition $\langle \tilde{u}, F_2 \rangle = 0$ is always satisfied, since all integral terms go to 0. Thus a solution $\boldsymbol{u}_2$ exists, and we seek to find it using the ansatz

$$\boldsymbol{u}_2 = \mathbf{C}_2 e^{2ikx} + \mathbf{C}_{-2} e^{-2ikx} + \mathbf{C}_0 + \zeta \boldsymbol{u}_1, \tag{4.19}$$

where $\mathbf{C_{\pm 2}}$ and $\mathbf{C_0}$ are $x-$independent coefficient vectors. Plugging equation (4.19) into equation (4.15) and collecting terms yields

$$\mathbf{M}(k)\mathbf{C}_2 = -z^2 \mathbf{B}(a+\bar{a}), \quad \mathbf{C}_{-2} = \overline{\mathbf{C}}_2, \quad \mathbf{M}(0)\mathbf{C}_0 = -2|z|^2 \mathbf{B}(a+\bar{a}), \tag{4.20}$$

with matrices

$$\mathbf{M}(k) = \begin{pmatrix} -4k^2\gamma_c + f_1 & f_2 & f_2 \\ g_1 & -2ik - 1 + g_2 & 1 + g_2 \\ g_1 & 1 + g_2 & 2ik - 1 + g_2 \end{pmatrix}, \tag{4.21}$$

$$\mathbf{B}(a+\bar{a}) = \frac{1}{2} \begin{pmatrix} f_{11} + f_{22}(a+\bar{a})^2 + 2f_{12}(a+\bar{a}) \\ g_{11} + g_{22}(a+\bar{a})^2 + 2g_{12}(a+\bar{a}) \\ g_{11} + g_{22}(a+\bar{a})^2 + 2g_{12}(a+\bar{a}) \end{pmatrix}. \tag{4.22}$$

Assuming that $\mathbf{M}(k)$ is invertible and introducing the vector

$$\mathbf{G}(k) = -\mathbf{M}(k)^{-1}\mathbf{B}(a+\bar{a}), \tag{4.23}$$

we have the explicit solutions

$$\mathbf{C}_2 = z^2 \mathbf{G}(k), \quad \mathbf{C}_{-2} = \bar{z}^2 \overline{\mathbf{G}}(k), \quad \mathbf{C}_0 = 2|z|^2 \mathbf{G}(0). \tag{4.24}$$

Setting $\mathbf{G}(k) = (G_p(k), G_+(k), G_-(k))^\top$, we note that $G_p(k)$, $G_+(k) + G_-(k)$, and $G_\pm(0)$ are real.

Collecting the $\mathcal{O}(\epsilon^{3/2})$ terms, we find

$$\mathcal{L}\boldsymbol{u}_3 = \partial_\tau \boldsymbol{u}_1 + \mathbf{F}_3, \quad \mathbf{F_3} = -\begin{pmatrix} F_{3,1} \\ F_{3,2} \\ F_{3,3} \end{pmatrix}$$

where

$$\begin{aligned} F_{3,1} =& \Delta\gamma \partial_{xx} p_1 + f_{11} p_1 p_2 + f_{22} \mathcal{A}_1 \mathcal{A}_2 + f_{12}(p_1 \mathcal{A}_2 + p_2 \mathcal{A}_1) \\ &+ \frac{1}{6}\left(f_{111} p_1^3 + 3 f_{112} p_1^2 \mathcal{A}_1 + 3 f_{122} p_1 \mathcal{A}_1^2 + f_{222} \mathcal{A}_1^3\right), \\ F_{3,2} =& g_{11} p_1 p_2 + g_{22} \mathcal{A}_1 \mathcal{A}_2 + g_{12}(p_1 \mathcal{A}_2 + p_2 \mathcal{A}_1) \\ &+ \frac{1}{6}\left(g_{111} p_1^3 + 3 f_{112} p_1^2 \mathcal{A}_1 + 3 g_{122} p_1 \mathcal{A}_1^2 + g_{222} \mathcal{A}_1^3\right), \\ F_{3,3} =& F_{3,2}. \end{aligned}$$

Once again, there exists a solution $\boldsymbol{u}_3$ if and only if $\langle \tilde{u}, \partial_\tau \boldsymbol{u}_1 + \mathbf{F}_3 \rangle = 0$. Substituting in the expression for $\boldsymbol{u}_2$ and calculating the various inner products, we obtain the following equation:

$$\begin{aligned}\frac{dz}{d\tau}(1+2|a|^2) = -k^2\Delta\gamma z + \frac{1}{2}\left[h_{111} + 3h_{112}(a+\bar{a}) + 3h_{122}(a+\bar{a})^2 + h_{222}(a+\bar{a})^3\right] z|z|^2 \\ + \left[h_{11}(G_p(k) + 2G_p(0)) + h_{22}(a+\bar{a})(G_+(k) + G_-(k) + 2G_+(0) + 2G_-(0))\right] z|z|^2 \\ + h_{12}\left[(G_+(k) + G_-(k) + 2G_+(0) + 2G_-(0)) + (a+\bar{a})(G_p(k) + 2G_p(0))\right] z|z|^2,\end{aligned} \tag{4.25}$$

with

$$h_{ij\ldots l} = f_{ij\ldots l} + (a+\bar{a})g_{ij\ldots l}.$$

In summary, the amplitude equation takes the expected cubic form

$$\frac{dz}{d\tau} = \frac{z}{1+2|a|^2}(-k^2|\Delta\gamma| + \beta(k)|z|^2), \tag{4.26}$$

with β the real coefficient

$$\begin{aligned}\beta = \frac{1}{2}\left[h_{111} + 3h_{112}(a+\bar{a}) + 3h_{122}(a+\bar{a})\right]^2 + h_{222}(a+\bar{a})^3\right] \\ + \left[h_{11}(G_p(k) + 2G_p(0)) + h_{22}(a+\bar{a})(G_+(k) + G_-(k) + 2G_+(0) + 2G_-(0))\right] \\ + h_{12}\left[(G_+(k) + G_-(k) + 2G_+(0) + 2G_-(0)) + (a+\bar{a})(G_p(k) + 2G_p(0))\right] z|z|^2.\end{aligned} \tag{4.27}$$

A stable pattern will occur provided that $\beta(k) < 0$ at the critical wavenumber.

4.2 Pattern formation in two dimensions

In this section, we seek to further develop our understanding of the reaction-transport mechanism by considering the model in two dimensions. In the case of neurites in the *C. elegans* ventral cord, microtubules tend to be aligned in parallel so that the active transport process is effectively one-dimensional. In most nonpolarized animal cells, however, intracellular transport occurs along a network where microtubules project radially from an organizing center with outward polarity [2]. This organization is important for transport of molecules to and from the nucleus. Furthermore, it is known that microtubules bend due to large internal stresses, resulting in a locally disordered network. In other words, this suggests that microtubules on short length scales *in vivo* exhibit disorder in orientation and polarity, and thus may behave like transport *in vitro* [8, 11]. While specifying the exact

spatial distribution of microtubules along with orientation and polarity would require a detailed microscopic model, we can assume that the network is sufficiently dense so that active transport within the cell can be represented in terms of a velocity jump process [1, 5, 9]. This provides biological motivation for extending the reaction-transport model to higher dimensions. A schematic of this model is shown in Figure 4.1.

4.2.1 The model

Once again, we let $P(\mathbf{x}, t)$ be the concentration of passively transported particles at position $\mathbf{x} \in \mathbb{R}^2$ at time t and $A(\mathbf{x}, \mathbf{v}, t)$ denote the corresponding concentration of actively transported particles with velocity $\mathbf{v} \in V \subset \mathbb{R}^2$. The two dimensional formulation of the model then reads

$$\frac{\partial P}{\partial t} = D\nabla^2 P + f(P, \mathcal{A}) \tag{4.28a}$$

$$\frac{\partial A}{\partial t} = -\mathbf{v} \cdot \nabla A - \alpha A + \alpha \int_V T(\mathbf{v}, \mathbf{v}') A(\mathbf{x}, \mathbf{v}', t) d\mathbf{v}' + g(P, \mathcal{A}), \tag{4.28b}$$

where

$$\mathcal{A}(\mathbf{x}, t) = \int_V A(\mathbf{x}, \mathbf{v}, t) d\mathbf{v}, \tag{4.29}$$

and $T(\mathbf{v}, \mathbf{v}')$ is called the turning distribution [10]. The latter describes the probability that an AT particle with velocity $\mathbf{v}'$ switches to the velocity $\mathbf{v}$. Here we consider some particular types of turning functions relevant to intracellular transport, such as those considered by Bressloff and Newby in [6]. First, we assume that the speed is the same in all directions so that $\mathbf{v}$ can be parameterized by the direction angle $\theta \in [0, 2\pi)$ and $\mathbf{v}(\theta) = v(\cos\theta, \sin\theta)$. Under this assumption, we can write $A = A(\mathbf{x}, \theta, t)$ and the turning operator as $T(\theta, \theta')$. We can further simplify the model by assuming that T is independent of θ'. Then, the model reads

$$\frac{\partial P}{\partial t} = D\nabla^2 P + f(P, \mathcal{A}) \tag{4.30a}$$

$$\frac{\partial A}{\partial t} = -\mathbf{v}(\theta) \cdot \nabla A - \alpha A + \alpha T(\theta) \mathcal{A}(\mathbf{x}, t) + g(P, \mathcal{A}), \tag{4.30b}$$

with

$$\mathcal{A}(\mathbf{x}, t) = \int_0^{2\pi} A(\mathbf{x}, \theta, t) d\theta, \quad \int_0^{2\pi} T(\theta) d\theta = 1. \tag{4.31}$$

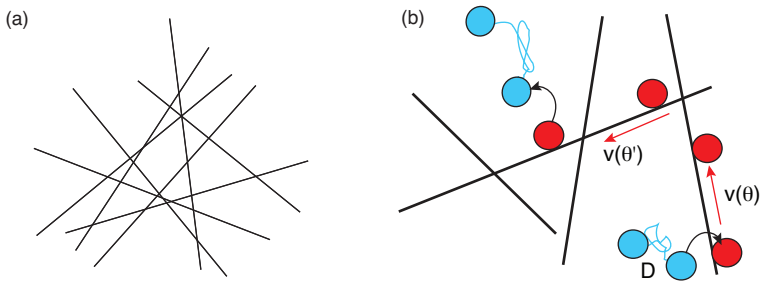

Figure 4.1. Reaction-transport model on a disordered microtubular network. (a) Random orientational arrangement of microtubules. (b) Hybrid 2D transport in which a particle switches between diffusion and ballistic motion in a random direction θ. We ignore the polarization of each filament, since we assume that a bound particle can reverse its direction along a given filament, as in the one-dimensional model.

4.2.2 Future work: bifurcation analysis of two dimensional pattern formation

We will explore whether Turing-type instabilities can arise with a two-dimensional version of this hybrid transport model, where it is necessary to consider the microtubular network configuration. If we assume that the microtubule network is locally disordered and sufficiently dense, we can make the simplifying homogenization assumption that all velocity directions are possible independent of position. Alternatively, one can suppose that the microtubules are arranged in a dense mesh in the plane, which is formed by a regular planar lattice. For a given lattice type (*e.g.* square or hexagonal), there will be a corresponding group generated by the rotations and reflections that preserve the lattice. We can exploit this group structure to study the bifurcations of the solutions. In general, unlike the classical reaction-diffusion models, the full hybrid reaction-transport equations has an oriented structure which explicitly breaks $\mathbf{O}(2)$ symmetry. However, we can exploit the existing shift-twist symmetries of the system to understand selection and stability of patterns in higher dimensions. The same shift-twist Euclidean group action occurs within the context of continuum neural field models of primary visual cortex, where non–local interactions are mediated by axonal connections between neurons that are tuned to respond to oriented visual stimuli [4, 3, 12]. These symmetries have not yet been explored in the context of transport models.

4.3 References

[1] O. Benichou, C. Loverdo, M. Moreau, and R. Voituriez, *A minimal model of intermittent search in dimension two*, J. Phys. Condens. Matter, 19 (2007), p. 065141.

[2] P. C. Bressloff, *Stochastic processes in cell biology*, vol. 41, Springer, 2014.

[3] P. C. Bressloff, J. D. Cowan, M. Golubitsky, and P. J. Thomas, *Scalar and pseudoscalar bifurcations motivated by pattern formation on the visual cortex*, Nonlinearity, 14 (2001), p. 739.

[4] P. C. Bressloff, J. D. Cowan, M. Golubitsky, P. J. Thomas, and M. C. Wiener, *Geometric visual hallucinations, Euclidean symmetry and the functional architecture of striate cortex*, Philos. Trans. R. Soc. Lond. B Biol. Sci., 356 (2001), pp. 299–330.

[5] P. C. Bressloff and J. M. Newby, *Quasi-steady-state analysis of two-dimensional random intermittent search processes*, Phys. Rev. E, 83 (2011), p. 061139.

[6] ——, *Stochastic models of intracellular transport*, Rev. Modern Phys., 85 (2013), p. 135.

[7] H. A. Brooks and P. C. Bressloff, *A mechanism for Turing pattern formation with active and passive transport*, SIAM J. Appl. Dyn. Syst., 15 (2016), pp. 1823–1843.

[8] A. Kahana, G. Kenan, M. Feingold, M. Elbaum, and R. Granek, *Active transport on disordered microtubule networks: The generalized random velocity model*, Phys. Rev. E, 78 (2008), p. 051912.

[9] C. Loverdo, O. Bénichou, M. Moreau, and R. Voituriez, *Robustness of optimal intermittent search strategies in one, two, and three dimensions*, Phys. Rev. E, 80 (2009), p. 031146.

[10] H. G. Othmer and T. Hillen, *The diffusion limit of transport equations derived from velocity-jump processes*, SIAM J. Appl. Math., 61 (2000), pp. 751–775.

[11] H. Salman, A. Abu-Arish, S. Oliel, A. Loyter, J. Klafter, R. Granek, and M. Elbaum, *Nuclear localization signal peptides induce molecular delivery along microtubules*, Biophys. J., 89 (2005), pp. 2134–2145.

[12] P. J. Thomas and J. D. Cowan, *Symmetry induced coupling of cortical feature maps*, Phys. Rev. Lett., 92 (2004), p. 188101.

CHAPTER 5

COARSE-GRAINING INTERMITTENT INTRACELLULAR TRANSPORT: TWO- AND THREE-DIMENSIONAL MODELS

The article in this chapter was originally published in Physical Review E **92**, 042709 (2015).

PHYSICAL REVIEW E **92**, 042709 (2015)

Coarse-graining intermittent intracellular transport: Two- and three-dimensional models

Sean D. Lawley,* Marie Tuft, and Heather A. Brooks
Department of Mathematics, University of Utah, Salt Lake City, Utah 84112, USA
(Received 31 August 2015; published 20 October 2015)

Viruses and other cellular cargo that lack locomotion must rely on diffusion and cellular transport systems to navigate through a biological cell. Indeed, advances in single particle tracking have revealed that viral motion alternates between (a) diffusion in the cytoplasm and (b) active transport along microtubules. This intermittency makes quantitative analysis of trajectories difficult. Therefore, the purpose of this paper is to construct mathematical methods to approximate intermittent dynamics by effective stochastic differential equations. The coarse-graining method that we develop is more accurate than existing techniques and applicable to a wide range of intermittent transport models. In particular, we apply our method to two- and three-dimensional cell geometries (disk, sphere, and cylinder) and demonstrate its accuracy. In addition to these specific applications, we also explain our method in full generality for use on future intermittent models.

DOI: 10.1103/PhysRevE.92.042709 PACS number(s): 87.17.Aa, 87.16.A−, 05.10.Gg, 87.10.−e

I. INTRODUCTION

Intracellular transport of cargo (macromolecules and organelles) is fundamental to cellular function. Indeed, many diseases are associated with defects in intracellular transport [1]. In addition, trafficking through the cytoplasm is a crucial step in viral and nonviral mediated gene transfer [2–4]. In order to infect and multiply inside a host cell, viruses must travel through the cytoplasm to the nucleus, and newly formed viral progeny must travel back this route to exit the cell.

Lacking locomotion, viruses and other cellular cargo must rely on diffusion and existing cellular transport systems to maneuver through a biological cell. Advances in live cell imaging and single particle tracking have revealed the complex nature of viral motion. Viruses alternate between epochs of (a) diffusion in the cytoplasm and (b) active transport along microtubules [5–7]. This intermittency makes quantitative analysis of trajectories difficult.

Therefore, we seek to approximate the intermittent dynamics by some simpler effective dynamics. In this paper, we answer the following question: given information about the cell and the cargo (cellular and microtubular geometry, cargo dynamics in cytoplasm, cargo dynamics on microtubules, number of microtubules, etc.), how can we find an effective stochastic differential equation (SDE) to approximate the intermittent cargo motion? Put another way, we show how to choose two parameters (the drift and diffusion coefficient in an SDE) that encapsulate the full intermittent dynamics.

Using Monte Carlo simulations, we verify the accuracy of our methods by showing that the probability distributions of random variables stemming from our effective SDE match the probability distributions of random variables stemming from the full intermittent process. In particular, we compare the distributions of first passage times (FPTs) and the distributions of the spatial position of the process at a sequence of times. We note that this is a more stringent test of accuracy than previous methods which sought to match only *means* of FPTs and not *distributions* of FPTs [8,9].

Given its biological and medical importance, intracellular transport has garnered mathematical attention for decades [10]. Recently, mathematicians have developed techniques to compute the efficiency of the delivery of plasmids or viral DNAs from the cell membrane to nuclear pores [11–13]. These techniques, however, take as their starting point a single SDE describing cargo motion, not the full intermittent dynamics. Our method for reducing intermittent dynamics to an SDE is therefore well motivated. Existing methods for this reduction exist, but they apply only to two-dimensional cells [8,9]. Our method applies to three-dimensional cells (Secs. IV and V) and is in fact more accurate than previous methods for two-dimensional cells (Sec. II).

The paper is organized as follows. We begin in Sec. II by describing a well-known model of intermittent intracellular transport in a two-dimensional cell that was first formulated in Ref. [8]. In Refs. [8,9], the authors derive effective SDEs to approximate this intermittent model, and so we compare our coarse-graining method to theirs. We give our general coarse-graining method in Sec. III and demonstrate its wide applicability in Secs. IV and V by applying it to models of intermittent intracellular transport in spherical and cylindrical cellular geometries, respectively. In all cases, Monte Carlo simulations show that our effective SDE closely resembles the intermittent dynamics. We conclude with a brief summary.

II. TWO-DIMENSIONAL CELL—DISK

We begin by applying our coarse-graining method to a well-known model of virus trafficking in a two-dimensional cell that was formulated in Ref. [8] and further studied in Refs. [9,12]. In this model, the cell is a two-dimensional disk of radius R with its nucleus located in a concentric disk of smaller radius $\delta < R$ (this cellular geometry would apply, for example, to flat skin fibroblast culture cells [14]). There are N microtubules radiating from the nucleus to the cellular membrane that partition the cytoplasm into N wedges of equal angular width $\Theta = 2\pi/N$ (see Fig. 1). By this symmetry, it is enough to consider the viral motion restricted to one of these N wedges:

$$C := \{(r,\theta) : \delta \leqslant r \leqslant R \text{ and } \theta \in [0,\Theta]\}.$$

*lawley@math.utah.edu

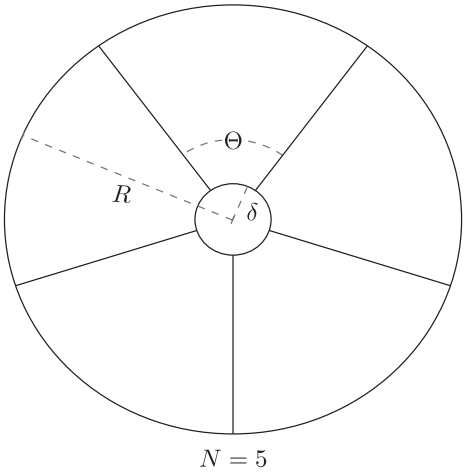

FIG. 1. Two-dimensional cell model with cell radius R, nucleus radius δ, and $N = 5$ microtubules. Each wedge has angular width $\Theta = 2\pi/N$.

A virus enters C at the cellular membrane at radius R at an angle uniformly distributed in $[0,\Theta]$. The virus then moves by pure diffusion with diffusion coefficient D in the cytoplasm (with a reflecting boundary condition at the cellular membrane at radius R) until it either hits the nucleus at radius δ or hits a microtubule at angle 0 or Θ. If the virus ever reaches radius δ, then it is immediately absorbed. If the virus hits a microtubule, then it moves along the microtubule toward the nucleus with constant velocity V for an exponentially distributed amount of time. After this exponential time, the virus is released back into the cytoplasm at its current radius at an angle uniformly distributed in $[0,\Theta]$ and begins to diffuse again (see Fig. 2).

The virus continues to alternate between epochs of diffusion and directed motion along microtubules until it reaches the nucleus. If we write the position of the virus at time t in polar coordinates $(r_t,\theta_t) \in C$, then viral motion is described by

$$dr_t = \begin{cases} -V\,dt & \text{on a microtubule} \\ (D/r_t)dt + \sqrt{2D}\,dW_t^r & \text{in cytoplasm,} \end{cases}$$
$$d\theta_t = \begin{cases} 0 & \text{on a microtubule} \\ (\sqrt{2D}/r_t)dW_t^\theta & \text{in cytoplasm,} \end{cases} \tag{2.1}$$

where W_t^r and W_t^θ are independent standard Brownian motions.

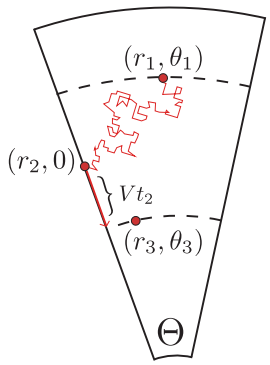

FIG. 2. (Color online) Sample trajectory of intermittent dynamics within a single wedge of two-dimensional cell model. Here, the virus diffuses in the cytoplasm from radius r_1 and angle θ_1 until it hits the microtubule at radius r_2 and angle 0. It then moves along the microtubule at velocity V for an exponentially distributed time t_2. Then, it is released back into the cytoplasm at radius $r_3 = r_2 - Vt_2$ and at an angle θ_3 uniformly distributed in $[0,\Theta]$. The process continues until the virus is absorbed at radius δ.

The intermittent nature of this process makes it difficult to analyze. Thus, much effort has gone into finding effective coarse-grained SDE approximations. In Sec. II A below, we outline this previous work and identify aspects that we seek to improve. We then give our coarse-grained SDE in Sec. II B and make comparisons in Sec. II C.

A. Previous coarse-grained dynamics by Lagache and Holcman

In Refs. [8,9], the authors use sophisticated asymptotic analysis of partial differential equations to derive a radial drift $B(r)$ in terms of model parameters in order to approximate the intermittent dynamics in Eq. (2.1) by an effective radial SDE

$$dr_t = [D/r_t - B(r_t)]\,dt + \sqrt{2D}\,dW_t. \tag{2.2}$$

In Ref. [8] the derived drift $B(r)$ is constant in r, whereas in Ref. [9] it a function of r. In both papers, the authors take the effective angular SDE to be the cytoplasmic angular SDE from the intermittent dynamics, namely,

$$d\theta_t = (\sqrt{2D}/r_t)\,dW_t^\theta.$$

In both Refs. [8,9], the approximation in Eq. (2.2) is justified by two criteria: (a) the mean first passage time (MFPT) to the nucleus for the effective dynamics in Eq. (2.2) closely matches the MFPT to the nucleus for the intermittent dynamics in Eq. (2.1) if $\Theta \ll 1$, and (b) if one imposes reflecting boundary conditions at the nucleus, then the steady state radial distribution of the effective dynamics in Eq. (2.2) resembles the steady state distribution of the intermittent dynamics in Eq. (2.1) for certain intermediate values of Θ.

The FPT to the nucleus is closely related to the probability and timing of viral infection and is thus a key biological quantity. Therefore, matching the FPTs for the two processes is a good criteria for justifying the coarse-grained SDE, and so we agree in principle with criteria (a). However, while the MFPTs for Eqs. (2.1) and (2.2) match closely, we discover below that the FPT *distributions* for the two processes are quite different. We thus seek an effective SDE whose FPT distribution matches that of the intermittent dynamics in Eq. (2.1). Furthermore, we want the effective SDE to be valid for a larger range of Θ. We see below that our effective SDE accomplishes both of these.

In addition, the criteria (b) of matching steady state radial distributions could be sharpened since steady state distributions contain (in principle) little information about time scale. As a trivial example, consider a diffusing particle in a one-dimensional interval with reflecting boundaries. The steady state distribution (uniform) is completely independent of the diffusion coefficient, but the dynamics are of course highly dependent on the diffusion coefficient. Instead of seeking to match the steady state radial distribution (which

is essentially the radial distribution at infinite time), we match the radial distribution at a sequence of finite times.

Furthermore, the fact that criteria (b) can only hold in certain intermediate parameter regimes is made clear by the form of the effective SDE in Eq. (2.2). Notice that the diffusion term in Eq. (2.2) is the same as the cytoplasmic diffusion term for the radial dynamics in Eq. (2.1). Thus, the effective SDE (2.2) always has this same amount of noise. However, this effective SDE was derived under the assumption that $\Theta \ll 1$, and it is clear that the intermittent process becomes deterministic in this limit because the proportion of time that the virus is bound to a microtubule converges to one. Thus, the steady state radial distribution for the intermittent process in this limit must be a delta function at the nucleus, and so the steady state radial distributions of Eqs. (2.1) and (2.2) cannot match in this limit. We see below that assuming the diffusion term in the effective SDE is the same as the cytoplasmic diffusion term causes other problems. We thus allow the diffusion term in our effective SDE to depend on Θ.

B. New coarse-grained dynamics

A systematic exposition of our general coarse-graining method is given below in Sec. III, but we first illustrate our method for the two-dimensional cell model described above. We approximate the intermittent dynamics of Eq. (2.1) by an effective radial SDE that is a mixture of the cytoplasmic and microtubular dynamics

$$dr_t = \{[D/r_t)(1 - p(r_t)] - Vp(r_t)\}dt + \sqrt{2D[1 - p(r_t)]}\, dW_t, \tag{2.3}$$

where $p(r)$ is related to the probability that the virus is on a microtubule given that it is at radius r.

A precise definition of $p(r)$ is given in Sec. III, but first consider the following intuitive derivation. By assumption, each time the virus hits a microtubule, it attaches to the microtubule for an exponential amount of time (say with mean μ). After this exponential time, the virus is released back into the cytoplasm at its current radius (call it r) at an angle uniformly distributed in $[0,\Theta]$. Ignoring radial motion, we approximate the amount of time it takes the virus to reach a microtubule again by

$$T(r) := \frac{1}{\Theta}\int_0^{\Theta} \tau(\theta; r)d\theta, \tag{2.4}$$

where $\tau(\theta; r)$ satisfies boundary value problem

$$\frac{D}{r^2}\frac{d}{d\theta}\tau(\theta; r) = -1, \quad \tau(0; r) = 0 = \tau(\Theta; r). \tag{2.5}$$

For a particle diffusing in the interval $[0,\Theta]$ with diffusion coefficient D/r^2, the quantity $T(r)$ is the MFPT to reach either 0 or Θ, given a uniform initial position [15]. A quick calculation yields $T(r) = \Theta^2 r^2/(12D)$.

Setting $p(r)$ as the proportion of time on a microtubule

$$p(r) = \frac{\mu}{\mu + T(r)},$$

our effective SDE in Eq. (2.3) becomes

$$dr_t = \left(\frac{D}{r_t}\frac{T(r_t)}{\mu + T(r_t)} - V\frac{\mu}{\mu + T(r_t)}\right)dt \times \sqrt{2D\frac{T(r_t)}{\mu + T(r_t)}}\, dW_t. \tag{2.6}$$

C. Comparison

We now compare our effective SDE in Eq. (2.6) to both the original intermittent process in Eq. (2.1) and the effective SDE in Eq. (2.2) derived in Ref. [9]. In keeping with parameter values used in Refs. [8,9] (taken from experimental papers [5,16–18]), we take the radius of the cell to be $R = 20\ \mu$m, the radius of the nucleus to be $\delta = 5\ \mu$m, the cytoplasmic diffusion coefficient to be $D = 1.3\ \mu\text{m}^2\,\text{s}^{-1}$, the velocity on microtubules to be $V = 0.7\ \mu\text{m}\,\text{s}^{-1}$, and the average time on a microtubule to be $\mu = 1$ s.

Figure 3 compares the distributions of the FPT to the nucleus for various numbers of microtubules ($N = 12,24,48,96$). These values of N are in keeping with [8,9] which used N between 12 and 48. Figure 4 compares the distributions of the radial positions at times $t = 5,10,15$ for $N = 48$. That is, it compares the distribution of r_t for (2.1), (2.6), and (2.2) at $t = 5,10,15$. The standard Euler-Maruyama method is used to simulate the cytoplasmic motion in the intermittent process as well as the effective SDEs. It is clear from these figures that our SDE in Eq. (2.6) approximates the intermittent process more closely than the SDE in Eq. (2.2) derived in Ref. [9].

III. GENERAL METHOD

Before considering higher dimensional and more complicated cellular geometries in Secs. IV and V, we first give our general coarse-graining method. Suppose one is given a stochastic process $\{(\rho_t,\phi_t)\}_{t\geqslant 0} \in \mathbb{R} \times \mathbb{R}^d$. [We use the (ρ,ϕ) notation for analogy to Sec. II above, but notice that (ρ,ϕ) is not assumed to be a radius and angle as it takes values in $\mathbb{R} \times \mathbb{R}^d$.]

Let the sets $\{A_k\}_{k=1}^n \subset \mathbb{R}^d$ partition the state space of ϕ_t and suppose the dynamics of ρ_t depend only on which A_k the process ϕ_t is in and not on the details of ϕ_t. That is, suppose the dynamics of ρ_t are governed by the SDE

$$d\rho_t = \left(\sum_{k=1}^n b_k(\rho_t)1_{\phi_t\in A_k}\right)dt + \left(\sum_{k=1}^n \sigma_k(\rho_t)1_{\phi_t\in A_k}\right)dW_t, \tag{3.1}$$

where $1_{\{\cdot\}}$ denotes the indicator function, for some given functions $\{b_k(\rho)\}_{k=1}^n$ and $\{\sigma_k(\rho)\}_{k=1}^n$. [In the case of the two-dimensional cell considered in Sec. II above, $\rho_t = r_t, \phi_t = \theta_t$, $b_1(\rho) = V, \sigma_1(\rho) = 0, b_2(\rho) = D/\rho$, and $\sigma_2(\rho) = \sqrt{2D}$, with partitioning sets $A_1 = \{0,\Theta\}$ and $A_2 = (0,\Theta)$.]

The dynamics of ϕ_t may be complicated and may depend on ρ_t, but we suppose that which set A_k the process ϕ_t is in is approximately Markovian. That is, we suppose there exists a continuous-time Markov jump process J_t (with instantaneous

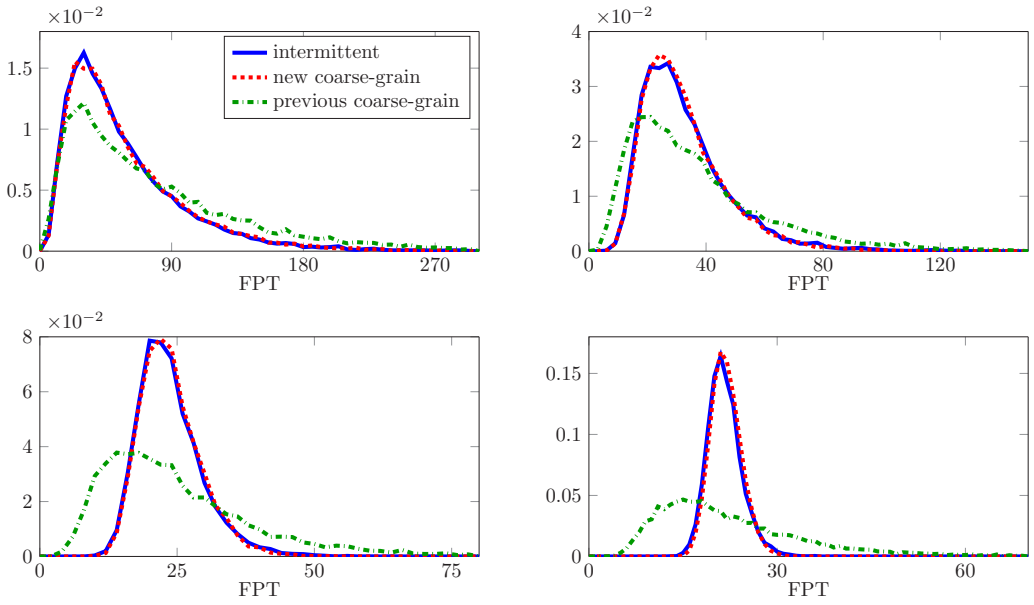

FIG. 3. (Color online) Empirical distributions of FPT to nucleus of 2D cell for intermittent in Eq. (2.1), our new coarse grain in Eq. (2.6), and the previous coarse grain in Eq. (2.2) derived in Ref. [9] for $N = 12$ (top left), $N = 24$ (top right), $N = 48$ (bottom left), and $N = 96$ (bottom right). Each distribution is calculated from 10^4 trials. Parameters are given in Sec. II C.

jump rates which may depend on ρ_t) so that

$$J_t \approx \sum_{k=1} k 1_{\phi_t \in A_k}.$$

[In the case of the two-dimensional cell considered in Sec. II above, J_t jumps from state 1 to 2 with rate $1/\mu$ and from 2 to 1 with rate $1/T(\rho_t)$.]

Under this assumption, we approximate ρ_t by

$$d\tilde{\rho}_t = \left(\sum_{k=1}^{n} b_k(\tilde{\rho}_t) 1_{J_t=k}\right) dt + \left(\sum_{k=1}^{n} \sigma_k(\tilde{\rho}_t) 1_{J_t=k}\right) dW_t.$$

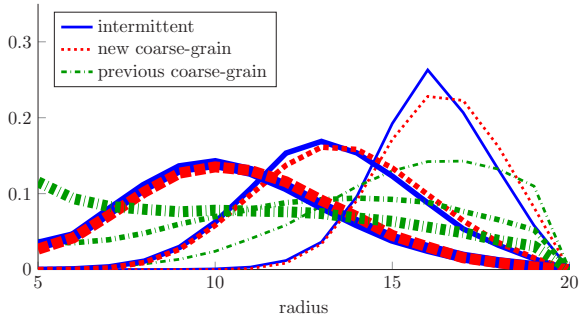

FIG. 4. (Color online) Empirical distribution of radial position for 2D cell for intermittent in Eq. (2.1), our new coarse grain in Eq. (2.6), and the previous coarse grain in Eq. (2.2) derived in Ref. [9] at times $t = 5, 10, 15$. Thicker lines correspond to larger times. Each distribution is calculated from 10^5 trials and we take $N = 48$. Parameters are given in Sec. II C.

This process $\tilde{\rho}_t$ is a hybrid switching diffusion [19]. If the J_t dynamics are much faster than the $\tilde{\rho}_t$ dynamics, then one can approximate $\tilde{\rho}_t$ to first order by the adiabatic limit (see Ref. [19], Chap. 12)

$$d\bar{\rho}_t = \left(\sum_{k=1}^{n} b_k(\bar{\rho}_t) p_k(\bar{\rho}_t)\right) dt + \left(\sum_{k=1}^{n} \sqrt{\sigma_k^2(\bar{\rho}_t) p_k(\bar{\rho}_t)}\right) dW_t, \tag{3.2}$$

where $\{p_k(\rho)\}_{k=1}^n$ is the quasi steady state distribution of J_t. This time scale separation is the key assumption. The SDE in Eq (3.2) is our coarse-grained effective SDE approximation to Eq. (3.1).

IV. THREE-DIMENSIONAL CELL—SPHERE

In this section, we first formulate a mathematical model of intermittent virus trafficking in a three-dimensional spherical cell and then apply our general coarse-graining method of Sec. III to derive an effective SDE describing viral motion.

In this intermittent model, the cell is a sphere of radius R with its nucleus located in a concentric sphere of smaller radius $\delta < R$. The position of the virus is restricted to the cytoplasm

$$C := \{\mathbf{x} \in \mathbb{R}^3 : |\mathbf{x}| \geqslant \delta \text{ and } |\mathbf{x}| \leqslant R\}.$$

There are N microtubules, each of radius ε, that radiate from the nucleus at radius δ to the cellular membrane at radius R (see Fig. 5). That is, for N points $\{\mathbf{c}_k\}_{k=1}^N$ on the unit sphere, we define the microtubules $\{m_k\}_{k=1}^N$ to be the sets

$$m_k = \{\mathbf{x} \in \mathbb{R}^3 : |\mathbf{x} - r\mathbf{c}_k| \leqslant \varepsilon \quad \text{for some} \quad r \in [\delta, R]\}.$$

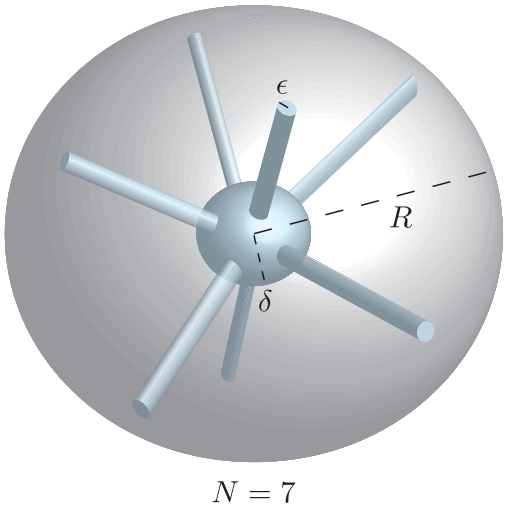

FIG. 5. (Color online) Three-dimensional spherical cell model with cell radius R, nucleus radius δ, and $N = 7$ microtubules with radius ε. The N microtubules radiate from locations on the nucleus which are randomly drawn from a uniform distribution.

We suppose that the N points $\{\mathbf{c}_k\}_{k=1}^N$ on the surface of the unit sphere are randomly placed according to a uniform distribution.

A virus enters the cell at the cellular membrane at a position uniformly distributed on the surface of the sphere of radius R. The virus then moves by pure diffusion with diffusion coefficient D in the three-dimensional cytoplasm (with a reflecting boundary condition at the cellular membrane at radius R) until it either hits the nucleus at radius δ or hits one of the N microtubules. If the virus ever reaches radius δ, then it is immediately absorbed. If the virus hits a microtubule, then it moves along the microtubule toward the nucleus with constant velocity V for an exponentially distributed amount of time. After this exponential time, the virus is released back into the cytoplasm at its current radius at a position uniformly distributed on the surface of the sphere with that radius, and then the virus begins to diffuse in the three-dimensional cytoplasm again.

The virus continues to alternate between epochs of diffusion and directed motion along microtubules until it reaches the nucleus. If we let $r_t \in [\delta, R]$ denote the radial position of the virus at time t, then the radial viral motion is described by

$$dr_t = \begin{cases} -V\,dt & \text{on a microtubule} \\ (2D/r_t)dt + \sqrt{2D}\,dW_t & \text{in cytoplasm.} \end{cases} \tag{4.1}$$

A. Coarse-grained spherical dynamics

To derive an effective SDE for the intermittent dynamics in Eq. (4.1), we cast the problem in the framework and notation of Sec. III. Let r_t denote the radial position of the virus and let $\mathbf{x}_t \in \mathbb{R}^3$ denote its Cartesian coordinates. Define the (ρ_t, ϕ_t) of Sec. III to be

$$(\rho_t, \phi_t) = (r_t, \mathbf{x}_t) \in \mathbb{R} \times \mathbb{R}^3.$$

The partitioning sets become

$$A_1 = \cup_{k=1}^N m_k \quad \text{and} \quad A_2 = \mathbb{R}^3 \backslash A_1.$$

The drift and diffusion terms become

$$b_1(\rho) = -V, \quad \sigma_1(\rho) = 0,$$
$$b_2(\rho) = 2D/\rho, \quad \sigma_2(\rho) = \sqrt{2D}.$$

In order to apply the method of Sec. III, it remains to approximate the process

$$1_{\phi_t \in A_1} + 21_{\phi_t \in A_2}$$

by a continuous-time Markov jump process J_t on {1,2}. Since the virus is assumed to attach to a microtubule for an exponential amount of time (say with mean μ), we suppose J_t jumps from state 1 to 2 with rate $1/\mu$.

Choosing the jump rate from state 2 to 1 is more difficult as it represents the rate at which a virus finds a microtubule. We choose it to be the inverse of the MFPT of a particle diffusing on the surface of a sphere to one of the N microtubules.

More precisely, let S denote the surface of the unit sphere and let $\eta(\rho) \subset S$ denote the set

$$\eta(\rho) := \{\mathbf{x} \in S : |\mathbf{x} - \mathbf{c}_k| \leqslant \varepsilon/\rho \quad \text{for some} \quad k = 1, \ldots, N\}.$$

Suppose $\tau(\mathbf{x}; \rho) : S \to [0, \infty)$ satisfies the following boundary value problem:

$$\Delta\tau(\mathbf{x}; \rho) = -\rho^2/D, \quad \mathbf{x} \in S\backslash\eta(\rho),$$
$$\tau(\mathbf{x}; \rho) = 0, \quad \mathbf{x} \in \partial\eta(\rho).$$

For a particle diffusing with diffusion coefficient D on the surface of a sphere of radius ρ, the quantity

$$\frac{1}{4\pi} \int_S \tau(\mathbf{x}; \rho)\, d\mathbf{x} \tag{4.2}$$

is the MFPT to hit one of N traps of radius ε centered at positions $\{\rho\mathbf{c}_k\}_{k=1}^N$, assuming the particle is initially distributed uniformly. Coombs, Straube, and Ward provide the following asymptotic approximation of Eq. (4.2) in the small ε limit [20]:

$$T(\rho) := \frac{\rho^2}{D}\left[-\frac{2}{N}\ln\left(\frac{\varepsilon}{\rho}\right) + 2\,\ln 2 - 1 - \frac{4}{N^2}\Psi\right],$$

where

$$\Psi = \sum_{k=1}^N \sum_{j>k}^N \ln|\mathbf{c}_k - \mathbf{c}_j|.$$

If we choose the jump rate of J_t from state 2 to 1 to be $1/T(\rho)$, then the quasi steady state distribution of J_t is given by

$$p_1(\rho) = \frac{\mu}{\mu + T(\rho)},$$

with $p_2(\rho) = 1 - p_1(\rho)$.

Thus, using Eq. (3.2) in Sec. III, we approximate the intermittent dynamics in Eq. (4.1) by the following effective SDE:

$$d\rho_t = \left(\frac{2D}{\rho_t}\frac{T(\rho_t)}{\mu + T(\rho_t)} - V\frac{\mu}{\mu + T(\rho_t)}\right)dt + \sqrt{2D\frac{T(\rho_t)}{\mu + T(\rho_t)}}\,dW_t. \tag{4.3}$$

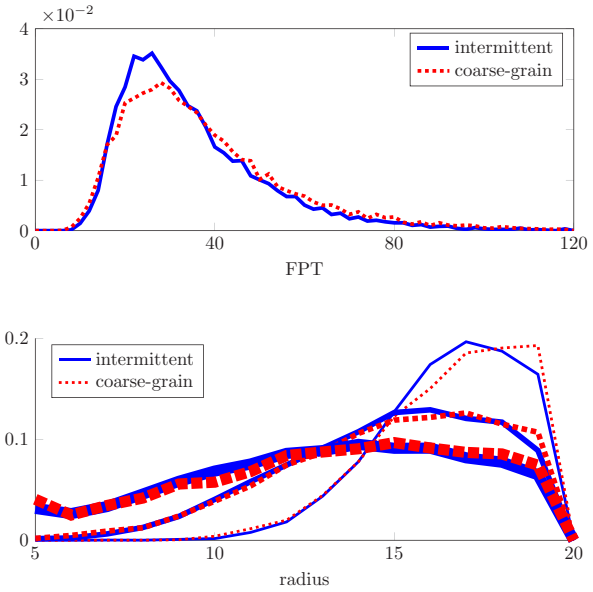

FIG. 6. (Color online) 3D spherical cell: comparison of intermittent in Eq. (4.1) and our coarse grain in Eq. (4.3). Each distribution is calculated from 10^4 trials and parameters are given in Sec. IV B. Top: Empirical distributions of FPT to nucleus. Bottom: Empirical distribution of radial position at times $t = 5, 10, 15$. Thicker lines correspond to larger times.

B. Comparison

We now compare the 3D intermittent dynamics of Eq. (4.1) to our effective SDE in Eq. (4.3).

In keeping with the parameters used in Sec. II, we take the radius of the cell to be $R = 20\ \mu$m, the radius of the nucleus to be $\delta = 5\ \mu$m, the cytoplasmic diffusion coefficient to be $D = 1.3\ \mu\text{m}^2\,\text{s}^{-1}$, the velocity on microtubules to be $V = 0.7\ \mu\text{m}\,\text{s}^{-1}$, and the average time on a microtubule to be $\mu = 1$ s. A typical eukaryotic cell large aster has between 600 and 1000 microtubules [16], and so we take $N = 1000$. A microtubule has approximate diameter 0.03 μm [21], an Adeno associated virus has approximate diameter 0.03 μm [5], and the interaction range between microtubules and molecular motors is approximately 0.05 μm [17]. Thus, we take $\varepsilon = 0.1\ \mu$m. The standard Euler-Maruyama method is used to simulate the cytoplasmic motion in the intermittent process as well as the effective SDE.

The top of Fig. 6 compares the distributions of the FPT to the nucleus and the bottom compares the distributions of the radial positions at a sequence of times. That is, the bottom compares the distribution of r_t for Eqs. (4.1) and (4.3) at $t = 5, 10, 15$. In both cases, the coarse-grained SDE closely approximates the full intermittent dynamics.

V. THREE-DIMENSIONAL CELL—CYLINDER

In this section, we formulate a mathematical model of virus trafficking in a three-dimensional cylindrical cell and apply our general coarse-graining method of Sec. III to derive an effective SDE describing viral motion. This cylindrical geometry is well motivated as many viruses rely on trafficking though axons and dendrites which resemble long cylinders.

Indeed, similar mathematical models of axonal transport have a long and rich history. Following experimental work in the 1970s and 1980s that showed radiolabeled amino acids progressing through axons as slowly spreading waves, Reed and Blum developed PDE models of axonal transport that remarkably exhibited this same behavior [22–24]. These PDE models have been generalized and have generated lots of rigorous mathematical analysis [25–28]. In addition to PDE models, probabilistic models (in both discrete and continuous time) have been constructed that also demonstrate this same behavior [29–32].

These previous models begin with two simplifying reductions: (a) the cell is one-dimensional, and (b) the rate at which a virus (or other cargo) attaches to a microtubule is some given exponential rate. Our intermittent model makes neither reduction; the cell's three-dimensional geometry is included, and the time when a virus attaches to a microtubule is determined by the random time that a virus diffusing in the three-dimensional cytoplasm hits a microtubule. However, the coarse-grained SDE that we derive in Sec. V A does make use of these reductions. We show in Sec. V B that this SDE compares favorably with the full intermittent model, and therefore verify the efficacy of these reductions and show how to make them. That is, we show how to choose the pair of one-dimensional parameters (drift and diffusion coefficient) in order to encapsulate the full three-dimensional model.

We now define the intermittent dynamics. In this model, the cell is a cylinder of length L and radius R:

$$C := \{(x,y,z) \in \mathbb{R}^3 : 0 \leqslant x \leqslant L \text{ and } y^2 + z^2 \leqslant R^2\}.$$

There are N microtubules, each of radius ε and length L, that run parallel to the principal axis of the cell (see Fig. 7). More precisely, for N points $\{(y_k,z_k)\}_{k=1}^N$ on the disk of radius R in the (y,z) plane, we define the microtubules $\{m_k\}_{k=1}^N$ to be the sets

$$m_k = \{(x,y,z) \in \mathbb{R}^3 : 0 \leqslant x \leqslant L,\ |(y,z) - (y_k,z_k)| \leqslant \varepsilon\}.$$

We suppose the N points $\{(y_k,z_k)\}_{k=1}^N$ are randomly placed on the disk of radius R according to a uniform distribution.

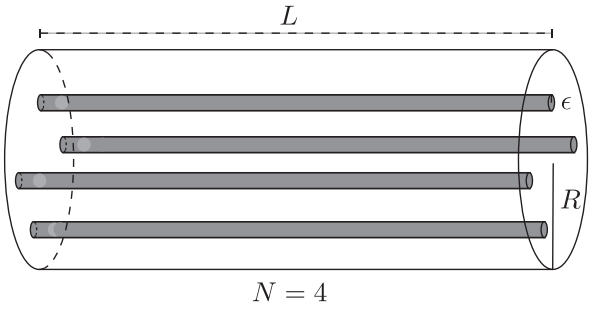

FIG. 7. Three-dimensional cylindrical (axon) model with cell radius R, length L, and $N = 4$ microtubules with radius ε. The locations of the N microtubules are randomly drawn from a uniform distribution.

We suppose that a virus enters the cell at position $(0,y_0,z_0) \in C$ with (y_0,z_0) uniformly distributed on the disk of radius R. The virus then moves by pure diffusion with diffusion coefficient D in the three-dimensional cytoplasm with a reflecting boundary condition at the cellular membrane

$$\{(y,z) \in \mathbb{R}^2 : y^2 + z^2 = R^2\}$$

and at the left end of the cell ($x = 0$), until it either hits the right end of the cell ($x = L$) or hits one of the N microtubules. If the virus reaches $x = L$, then it is immediately absorbed. If the virus hits a microtubule, then it moves along the microtubule with constant velocity $V > 0$ for an exponentially distributed amount of time. After this exponential time, the virus is released back into the cytoplasm at its current x position at a point in the (y,z) plane uniformly distributed on the disk of radius R, and then the virus begins to diffuse again.

The virus continues to alternate between epochs of diffusion and directed motion along microtubules until it reaches $x = L$. If we let $(x_t,y_t,z_t) \in C$ denote the position of the virus at time t, then the viral motion in the x direction is described by

$$dx_t = \begin{cases} V\,dt & \text{on a microtubule} \\ \sqrt{2D}\,dW_t & \text{in cytoplasm.} \end{cases} \tag{5.1}$$

A. Coarse-grained cylindrical dynamics

To derive an effective SDE for the intermittent dynamics in Eq. (5.1), we cast the problem in the framework and notation of Sec. III. Define the (ρ_t,ϕ_t) of Sec. III to be

$$(\rho_t,\phi_t) = (x_t,(y_t,z_t)) \in C.$$

The partitioning sets become

$$A_1 = \cup_{k=1}^{N} m_k \quad \text{and} \quad A_2 = C \backslash A_1.$$

The drift and diffusion terms become

$$b_1(\rho) = V, \quad \sigma_1(\rho) = 0,$$
$$b_2(\rho) = 0, \quad \sigma_2(\rho) = \sqrt{2D}.$$

In order to apply the method of Sec. III, it remains to approximate the process

$$1_{\phi_t \in A_1} + 2 1_{\phi_t \in A_2}$$

by a continuous-time Markov jump process J_t on $\{1,2\}$. Since the virus is assumed to attach to a microtubule for an exponential amount of time (say with mean μ), we suppose J_t jumps from state 1 to state 2 at rate $1/\mu$.

The jump rate from state 2 to state 1 represents the rate at which a virus finds a microtubule. We choose it to be the inverse of the MFPT of a particle diffusing on the disk of radius R to one of N uniformly distributed circular traps of radius ε. In the small ε limit, this MFPT is Ref. [9]

$$T = \frac{R^2 \ln(1/\varepsilon)}{2ND}.$$

The quasi steady state distribution of J_t is then given by

$$p_1 = \frac{\mu}{\mu + T} \quad \text{and} \quad p_2 = \frac{T}{\mu + T}.$$

Thus, using Eq. (3.2) in Sec. III, we approximate the intermittent dynamics in Eq. (5.1) by the following effective SDE:

$$d\rho_t = V \frac{\mu}{\mu + T}\,dt + \sqrt{2D \frac{T}{\mu + T}}\,dW_t. \tag{5.2}$$

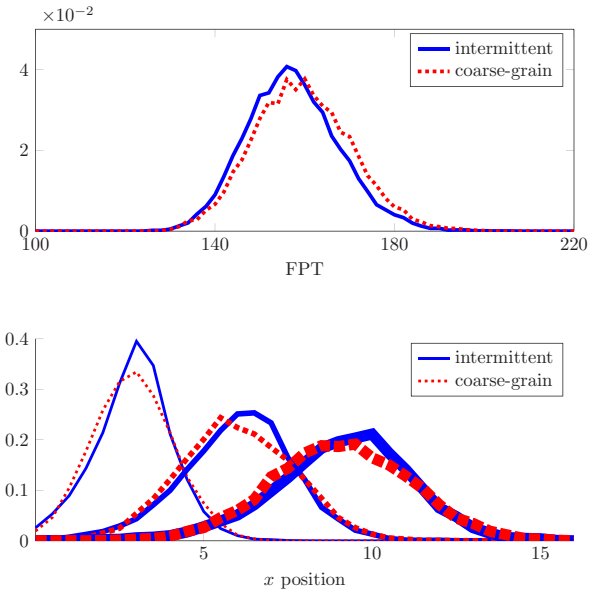

FIG. 8. (Color online) 3D cylindrical cell: comparison of intermittent in Eq. (5.1) and our coarse grain in Eq. (5.2). Each distribution is calculated from 10^4 trials and parameters are given in Sec. V B. Top: Empirical distributions of FPT to nucleus. Bottom: Empirical distribution of x position at times $t = 5,10,15$. Thicker lines correspond to larger times.

B. Comparison

We now compare the 3D intermittent dynamics of Eq. (5.1) to our effective SDE in Eq. (5.2). As above, we take $\varepsilon = 0.1\ \mu$m, $D = 1.3\ \mu\text{m}^2\,\text{s}^{-1}$, $V = 0.7\ \mu\text{m}\,\text{s}^{-1}$, and $\mu = 1$ s. We take $R = 10\ \mu$m, $L = 100$, and $N = 700$ [33,34]. The standard Euler-Maruyama method is used to simulate the cytoplasmic motion in the intermittent process as well as the effective SDE.

The top of Fig. 8 compares distributions of the FPT to $x = L$ and the bottom compares the distributions of the x positions at a sequence of times. That is, the bottom compares x_t in Eq. (5.1) and ρ_t in Eq. (5.2) at $t = 5,10,15$. In both cases, the coarse-grained SDE closely approximates the full intermittent dynamics.

VI. SUMMARY AND CONCLUSIONS

In this paper, we developed a method for coarse-graining intermittent intracellular transport into effective SDEs. We used Monte Carlo simulations to demonstrate the accuracy of our method across a variety of cellular geometries. For comparison and analogy to previous work, we incorporated various assumptions into the intermittent models (deterministic motion on microtubules, uniform placement in cytoplasm

after leaving a microtubule, etc.). However, we stress that our method (as described in Sec. III) is easily applied without these assumptions. We anticipate our method being used on future intermittent models and the machinery of Ref. [11] being applied to our effective SDEs [Eqs. (2.6) and (4.3)] to estimate the efficiency of viral infection. Additional future work includes combining our present coarse-grained models of viral motion with the sequence of biochemical transformations that viruses undergo during their journey through the cell, as these are known to affect the probability and timing of infection [35].

ACKNOWLEDGMENTS

We thank Paul C. Bressloff for comments on this work. S.D.L. was supported by NSF Grant No. DMS-RTG 1148230, M.T. was supported by NSF Grant No. DMS-RTG 1148230, and H.A.B. was supported by NSF Grant No. DMS-RTG 1148230.

[1] M. Aridor and L. A. Hannan, Traffic **1**, 836 (2000).
[2] C. M. Wiethoff and C. R. Middaugh, J. Pharm. Sci. **92**, 203 (2003).
[3] G. Zuber, E. Dauty, M. Nothisen, P. Belguise, and J.-P. Behr, Adv. Drug Delivery Rev. **52**, 245 (2001).
[4] K. Dohner, C.-H. Nagel, and B. Sodeik, Trends Microbiol. **13**, 320 (2005).
[5] G. Seisenberger, M. U. Ried, T. Endress, H. Buning, M. Hallek, and C. Brauchle, Science **294**, 1929 (2001).
[6] N. Arhel, A. Genovesio, K.-A. Kim, S. Miko, E. Perret, J.-C. Olivo-Marin, S. Shorte, and P. Charneau, Nat. Methods **3**, 817 (2006).
[7] B. Brandenburg and X. Zhuang, Nat. Rev. Microbiol. **5**, 197 (2007).
[8] T. Lagache and D. Holcman, SIAM J Appl. Math. **68**, 1146 (2008).
[9] T. Lagache and D. Holcman, Phys. Rev. E **77**, 030901(R) (2008).
[10] P. C. Bressloff and J. M. Newby, Rev. Mod. Phys. **85**, 135 (2013).
[11] D. Holcman, J. Stat. Phys. **127**, 471 (2007).
[12] T. Lagache, E. Dauty, and D. Holcman, Phys. Rev. E **79**, 011921 (2009).
[13] T. Lagache, E. Dauty, and D. Holcman, Curr. Opin. Microbiol. **12**, 439 (2009).
[14] A.-T. Dinh, T. Theofanous, and S. Mitragotri, Biophys. J. **89**, 1574 (2005).
[15] S. Redner, *A Guide to First-Passage Processes* (Cambridge University Press, Cambridge, UK, 2001).
[16] F. Nedelec, T. Surrey, and A. C. Maggs, Phys. Rev. Lett. **86**, 3192 (2001).
[17] D. L. Coy, M. Wagenbach, and J. Howard, J. Biol. Chem. **274**, 3667 (1999).
[18] S. J. King and T. A. Schroer, Nat. Cell Biol. **2**, 20 (2000).
[19] G. G. Yin and C. Zhu, *Hybrid Switching Diffusions: Properties and Applications* (Springer Science & Business Media, Berlin-Heidelberg, 2009).
[20] D. Coombs, R. Straube, and M. Ward, SIAM J. Appl. Math. **70**, 302 (2009).
[21] F. Gittes, B. Mickey, J. Nettleton, and J. Howard, J. Cell Biol. **120**, 923 (1993).
[22] J. J. Blum and M. C. Reed, Cell Motil. **5**, 507 (1985).
[23] M. C. Reed and J. J. Blum, Cell Motil. Cytoskeleton **6**, 620 (1986).
[24] M. C. Reed, S. Venakides, and J. J. Blum, SIAM J. Appl. Math. **50**, 167 (1990).
[25] A. Friedman and G. Craciun, J. Math. Biol. **51**, 217 (2005).
[26] A. Friedman and G. Craciun, SIAM J. Math. Anal. **38**, 741 (2006).
[27] A. Friedman and B. Hu, Indiana Univ. Math. J. **56**, 2133 (2007).
[28] A. Friedman and B. Hu, Arch. Ration. Mech. Anal. **186**, 251 (2007).
[29] E. A. Brooks, Ann. Appl. Probab. **9**, 719 (1999).
[30] P. C. Bressloff, Phys. Rev. E **74**, 031910 (2006).
[31] P. Bressloff and J. Newby, New J. Phys. **11**, 023033 (2009).
[32] L. Popovic, S. A. McKinley, and M. C. Reed, SIAM J. Appl. Math. **71**, 1531 (2011).
[33] D. Debanne, E. Campanac, A. Bialowas, E. Carlier, and G. Alcaraz, Physiol. Rev. **91**, 555 (2011).
[34] W. Yu and P. W. Baas, J. Neurosci. **14**, 2818 (1994).
[35] M. R. D'Orsogna and T. Chou, PLoS ONE **4**, e8165 (2009).

CHAPTER 6

QUASICYCLES IN THE STOCHASTIC HYBRID MORRIS-LECAR NEURAL MODEL

The article in this chapter was originally published in Physical Review E **92**, 012704 (2015).

PHYSICAL REVIEW E **92**, 012704 (2015)

Quasicycles in the stochastic hybrid Morris-Lecar neural model

Heather A. Brooks and Paul C. Bressloff*
Department of Mathematics, University of Utah, 155 South 1400 East, Salt Lake City, Utah 84112, USA
(Received 2 February 2015; published 6 July 2015)

Intrinsic noise arising from the stochastic opening and closing of voltage-gated ion channels has been shown experimentally and mathematically to have important effects on a neuron's function. Study of classical neuron models with stochastic ion channels is becoming increasingly important, especially in understanding a cell's ability to produce subthreshold oscillations and to respond to weak periodic stimuli. While it is known that stochastic models can produce oscillations (quasicycles) in parameter regimes where the corresponding deterministic model has only a stable fixed point, little analytical work has been done to explore these connections within the context of channel noise. Using a stochastic hybrid Morris-Lecar (ML) model, we combine a system-size expansion in K^+ and a quasi-steady-state (QSS) approximation in persistent Na^+ in order to derive an effective Langevin equation that preserves the low-dimensional (planar) structure of the underlying deterministic ML model. (The QSS analysis exploits the fact that persistent Na^+ channels are fast.) By calculating the corresponding power spectrum, we determine analytically how noise significantly extends the parameter regime in which subthreshold oscillations occur.

DOI: 10.1103/PhysRevE.92.012704 PACS number(s): 87.19.lc, 87.10.Mn, 05.40.−a

I. INTRODUCTION

Noise has emerged as a key component of a wide range of biological systems [1]. In the particular case of neuroscience, noise is present at all levels, yet neural networks are still able to perform complex computations reliably [2]. The most dominant source of intrinsic noise in neurons is ion channel noise [3,4]. The membrane potential of a neuron changes as ions such as Na^+ and K^+ pass in and out of the cell through voltage-dependent channels within the membrane and the opening and closing of the channels is stochastic due to thermal fluctuations [5]. In classical approaches, the number of ion channels is assumed to be very large and thus the fluctuations in membrane potential from individual stochastic channels is ignored in favor of a deterministic average. More recent work has questioned this assumption. It has been shown that channel noise indeed produces membrane potential fluctuations that are large enough to affect action potential timing [6–11] and increase the range of spiking behavior exhibited in some neural populations [3], with the effects of channel noise increasing dramatically as neurons become smaller. However, even when large numbers of stochastic ion channels are present in a neuron, fluctuations can become critical near the action potential threshold [2,12]. In addition, sodium channel noise places structural limits on neural anatomy [13], since in the case of very small neurons, significant channel noise would disrupt signal transmission [14].

Ion channel noise has also been implicated in subthreshold membrane potential oscillations (STOs). These are observed in a variety of neural cell types: stellate cells in the entorhinal cortex, hippocampal cells, and mitral cells in the olfactory bulb, to name a few. Intrinsic ion currents are sufficient to produce oscillatory activity [15]. Tetrodotoxin blocks STOs, implicating a persistent Na^+ current in the generation of oscillatory activity [16–20]. Using the dynamic clamp technique, it has been shown that stochastic flicker of these persistent sodium channels is crucial for subthreshold oscillations and phase locking to weak periodic stimuli in entorhinal spiny stellate cells [13]. Hyperpolarization is due to a noninactivating outward current, for example, a tetraethylammonium-sensitive M current in layer-V pyramidal cells [20]. In addition to the phase locking of periodic stimuli, it has been shown experimentally and theoretically that noise can enhance weak signal transduction in sensory neurons via tuning intrinsic subthreshold oscillations [21]. White *et al.* [18] showed that the presence of channel noise alters the dynamical behavior of a medial entorhinal cortical cell model; in particular, subthreshold oscillations are most easily generated for intermediate noise levels. In these cells, it is predicted that there are only on the order of 1000–5000 persistent Na^+ channels, a surprisingly small number that does not match the assumptions of classical deterministic neuron model approaches.

Deterministic conductance-based models of a single neuron such as the Hodgkin-Huxley model have been widely used to understand the dynamical mechanisms underlying membrane excitability [22]. These models assume a large population of ion channels so that their effect on membrane conductance can be averaged. As a result, the average fraction of open ion channels modulates the effective ion conductance, which in turn depends on voltage. It is often convenient to consider a simplified planar model of a neuron, which tracks the membrane voltage v and a recovery variable w that represents the fraction of open potassium channels. The advantage of a two-dimensional model is that one can use phase-plane analysis to develop a geometric picture of neuronal spiking. One well-known example is the Morris-Lecar (ML) model [23]. Although this model was originally developed to model Ca^{2+} spikes in mollusks, it has been widely used to study both type-I and type-II forms of neural excitability for Na^+ spikes [22] since it exhibits many of the same bifurcation scenarios as more complex models. The ML model has also been used to investigate STOs due to persistent Na^+ currents [24].

Another advantage of the ML model is that it is straightforward to incorporate intrinsic channel noise [25–27]. In order to

*bressloff@math.utah.edu

capture the fluctuations in membrane potential from stochastic switching in voltage-gated ion channels, the resulting model includes both discrete jump processes (to represent the opening and closing of ion channels) and a continuous-time piecewise process (to represent the membrane potential). This is an example of a stochastic hybrid system with piecewise deterministic dynamics. There has been much recent interest in such systems, within the context of both conductance-based models and gene and biochemical networks [1].

In this paper we use a stochastic hybrid ML model of a persistent (noninactivating) sodium current and a slower outward potassium current to investigate analytically the role of channel noise in the generation of STOs. Previous computational studies have shown how channel noise can significantly extend the parameter regime over which STOs occur [18,28]. We show that such a phenomenon can be analyzed in terms of the emergence of so-called quasicycles below a supercritical Hopf bifurcation point of the corresponding deterministic model. The emergence of quasicycles in a stochastic model—periodic oscillations that arise outside the limit cycle regime of a deterministic system—has been studied in various biological applications (see [29–33]). In some cases, such as calcium oscillations, the addition of noise serves to expand the range of parameter values for which limit cycle behavior is observed [29]; it is also possible in some reaction networks to induce oscillations where there are no limit cycles anywhere in the parameter space of the deterministic system [30].

In addition to providing an analytical framework for understanding noise-induced STOs, we introduce a mathematical approach to study quasicycles in stochastic hybrid systems. Typically, the emergence of quaiscycles in a jump Markov process is handled by carrying out a system-size expansion of the underlying master equation. This generates a Fokker-Planck (FP) equation, whose corresponding Langevin equation can be linearized about the fixed point solution of the deterministic system below the Hopf-bifurcation point. If the resulting power spectrum exhibits a significant peak at a nonzero frequency, then this indicates the existence of a quasicycle. In the case of the stochastic ML model, one could carry out a double system-size expansion with respect to the total number N of Na^+ channels and the total number M of K^+ channels. However, this would lead to a multivariate Langevin equation in three stochastic variables: the voltage v, the fraction w of open K^+ channels, and the fraction A of open Na^+ channels. Instead, we would like to preserve the low-dimensional (planar) structure of the ML model by deriving a Langevin equation for v and w alone.[1] We show how this can be achieved by exploiting the fact that the opening and closing of the persistent Na^+ channels is much faster than the dynamics of the voltage and the K^+ channels. We thus combine a quasi-steady-state (QSS) analysis of the Na^+ dynamics and a system-size expansion of the K^+ dynamics to derive a Langevin equation for the pair (v,w) and relate the existence of noise-induced STOs to the power spectrum of the resulting stochastic voltage. We briefly review the deterministic ML model in Sec. II, with parameter values chosen so that the model supports subthreshold oscillations via a supercritical Hopf bifurcation, rather than the more familiar spiking via a subcritical Hopf bifurcation. The stochastic version of the ML model is introduced in Sec. III, which is then systematically reduced by carrying out a system-size expansion with respect to K^+ (Sec. IV) and a QSS approximation with respect to Na^+ (Sec. V). The emergence of quasicycles (noise-induced STOs) is then established in Sec. VI.

II. DETERMINISTIC MODEL

A version of the deterministic Morris-Lecar model [23] has previously been used to understand the initiation and behavior of STOs [24]. The model consists of a persistent sodium current Na^+, a slow potassium current K^+, a leak current L, and an applied current $I_{\rm app}$. For simplicity, each ion channel is treated as a two-state system that switches between an open and a closed state; the more detailed subunit structure of ion channels is neglected [11,25]. The membrane voltage v evolves as

$$\begin{aligned}\frac{dv}{dt} &= a_\infty(v) f_{\rm Na}(v) + w f_{\rm K}(v) + f_L(v) + I_{\rm app},\\ \frac{dw}{dt} &= (1-w)\alpha_{\rm K}(v) - w\beta_{\rm K},\end{aligned} \tag{2.1}$$

where w is the K^+ gating variable. It is assumed that Na^+ channels are in quasi-steady-state $a_\infty(v)$, thus eliminating Na^+ as a variable. For $i = {\rm K,Na},L$, let $f_i = g_i(V_i - v)$, where g_i are ion conductances and V_i are reversal potentials. Opening and closing rates of ion channels depending only on membrane potential v are represented by α and β, respectively, so that

$$a_\infty(v) = \frac{\alpha_{\rm Na}(v)}{\alpha_{\rm Na}(v) + \beta_{\rm Na}(v)}. \tag{2.2}$$

For concreteness, take

$$\alpha_i(v) = \beta_i \exp\left(\frac{v - v_{i,1}}{v_{i,2}}\right), \quad i = {\rm K,Na}, \tag{2.3}$$

with β_i, $v_{i,1}$, and $v_{i,2}$ constant. Parameters are chosen (see Table I) such that there is no well-defined threshold above which an action potential is generated; rather, stable small-amplitude oscillations arise for a sufficient value of applied current (this appears in the model as a supercritical Hopf bifurcation). This corresponds well to the observed behavior of STOs and is not meant to function as a traditional spiking neuron model. Limit cycles in a traditional spiking model

[1]One motivation for preserving the planar structure of the ML model is that we would ultimately like to incorporate our theory of subthreshold oscillations into a model of spontaneous action potentials for an excitable neuron. This would require including a population of nonpersistent Na^+ ion channels along the lines of [27]. The analysis of the resulting escape problem becomes almost intractable beyond planar systems, so it is preferable to carry out a slow-fast analysis rather than a system-size expansion with respect to the two classes of Na^+ channels. The advantage of maintaining a low-dimensional Langevin equation by performing a slow-fast analysis rather than a system-size expansion also becomes significant when the complexity of the fast ion channels increases (see also Sec. VII).

TABLE I. Model parameters to generate subthreshold oscillations via a supercritical Hopf bifurcation. Note that we assume capacitance $C = 1\ \mu$F.

Sodium					Leak		Potassium				
g_{Na}	V_{Na}	β_{Na}	$v_{n,1}$	$v_{n,2}$	g_L	V_L	g_K	V_K	β_K	$v_{k,1}$	$v_{k,2}$
4.4 mS	55 mV	100 ms^{-1}	−1.2 mV	18 mV	2 mS	−60 mV	8 mS	−84 mV	0.35 ms^{-1}	2 mV	30 mV

often appear via a subcritical Hopf bifurcation. We do not provide further analysis for the subcritical Hopf case in this work; however, in the presence of noise, a transition to the oscillatory state has also been observed to shift in the vicinity of a subcritical Hopf bifurcation (see, for example, [34]). Thus, it is not unreasonable to expect that similar results may hold.

By evaluating the eigenvalues of the Jacobian of Eq. (2.1), it is straightforward to show that there is a unique steady state (v^*, w^*), which is linearly stable for $I_{app} < I^*_{app}$ [22]. At I^*_{app} a supercritical Hopf bifurcation occurs; (v^*, w^*) becomes unstable and a stable limit cycle emerges (see Fig. 1). Figure 2 shows the phase plane of the deterministic system; here one can see how oscillations arise in the membrane potential $v(t)$ as the applied current is increased.

III. STOCHASTIC MODEL

The deterministic ML model holds under the assumption that the number of ion channels is very large, thus the ion channel activation can be approximated by the average ionic currents. However, it is known that channel noise does affect membrane potential fluctuations (and thus neural function) and the number of persistent Na^+ channels is on the order of 10^3 [3,18]. In order to account for ion channel fluctuations, we consider a stochastic version of the Morris-Lecar model [25–27], with M K^+ channels and N Na^+ channels. Let $m(t)$ denote the number of open K^+ channels and $n(t)$ the number of open Na^+ channels at time t. Since it follows that the number of closed channels at time t is $M - m$ and $N - n$, respectively, there is no need to also track the number of closed channels. Then, for $m(t) = m$ and $n(t) = n$, the voltage evolves according to the equation

$$\frac{dv}{dt} = \frac{n}{N} f_{Na}(v) + \frac{m}{M} f_K(v) + f_L(v) + I_{app}. \tag{3.1}$$

We assume that the state transitions of the ion channels are given by a discrete Markov process, that is, ion channels are memoryless and the probability per unit time of changing states depends only on the current state, not on any past events (including the amount of time spent in the current state). In this case, sodium and potassium channels switch between open O and closed C states as follows:

$$C \underset{\beta_{Na}/\epsilon}{\overset{\alpha_{Na}(v)/\epsilon}{\rightleftarrows}} O, \quad C \underset{\beta_K}{\overset{\alpha_K(v)}{\rightleftarrows}} O. \tag{3.2}$$

The opening and closing of these channels is a birth-death process, where n and m evolve according to

$$\begin{aligned} n &\to n-1, \quad \omega_n^- = n\beta_{Na}, \\ n &\to n+1, \quad \omega_n^+ = (N-n)\alpha_{Na}(v), \\ m &\to m-1, \quad \omega_m^- = m\beta_K, \\ m &\to m+1, \quad \omega_m^+ = (M-m)\alpha_K(v). \end{aligned} \tag{3.3}$$

The above model is an example of a stochastic hybrid system based on a piecewise deterministic process. That is, the transition rates depend on v, with the latter coupled to the associated jump Markov process according to Eq. (3.1), which is only defined between jumps, during which $v(t)$ evolves deterministically. Furthermore, we assume that Na^+ channels open and close much faster than K^+ channels. We define $\epsilon = O(10^{-2})$ as a time scale variable for Na^+. Define $P(v,n,m,t)dv = \text{Prob}[n(t) = n; m(t) = m; v \leqslant v(t) \leqslant v + dv]$ at time t, given initial conditions $v(0) = v_0$, $m(0) = m_0$, and $n(0) = n_0$. Dropping the explicit dependence on initial conditions, this probability density will then satisfy the differential Chapman-Kolmogorov (CK) equation

$$\begin{aligned} \frac{\partial P}{\partial t} =& -\frac{\partial}{\partial v}\left[\left(\frac{n}{N} f_{Na}(v) + \frac{m}{M} f_K(v) + f_L(v) + I_{app}\right) P(v,n,m,t)\right] \\ &+ \frac{1}{\epsilon}[\omega_n^+(v,n-1)P(v,n-1,m,t) + \omega_n^-(v,n+1)P(v,n+1,m,t)] - \frac{1}{\epsilon}[(\omega_n^+(v,n) + \omega_n^-(v,n)]P(v,n,m,t) \\ &+ [\omega_m^+(v,m-1)P(v,n,m-1,t) + \omega_m^-(v,m+1)P(v,n,m+1,t)] - [\omega_m^+(v,m) + \omega_m^-(v,m)]P(v,n,m,t). \end{aligned} \tag{3.4}$$

The first line on the right-hand side represents the piecewise deterministic dynamics of v, whereas the second and third lines represent the stochastic opening and closing of Na^+ and K^+ ion channels, respectively. It is not possible to obtain exact solutions of the CK equation, so some sort of approximation is needed.

IV. SYSTEM-SIZE EXPANSION OF POTASSIUM

Suppose that M is large (but finite). Then it is possible to carry out a perturbation expansion in terms of the system size M^{-1}, which allows us to approximate the potassium dynamics as a continuous process [1,35,36]. The system-size expansion is a standard technique in stochastic processes

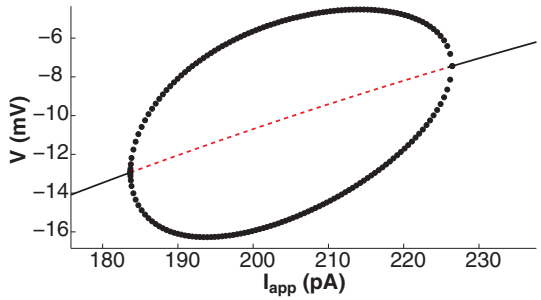

FIG. 1. (Color online) Bifurcation diagram of the deterministic model. As I_{app} is increased, the system undergoes a supercritical Hopf bifurcation H at $I_{app}^{*} = 183$, which leads to the generation of stable oscillations. The maximum and minimum values of oscillations are plotted as solid (black) curves. Oscillations disappear via another supercritical Hopf bifurcation.

that allows us to describe fluctuations about the deterministic theory via second-order terms in the expansion. It was first introduced within the context of stochastic ion channels by Fox and Lu [6] and further developed by Chow and White [7]. (More precisely, these authors assumed that the stochastic dynamics of a large population of identical ion channels can be approximated by a Gaussian process and then calculated the mean and variance based on single-channel properties.) First we introduce rescaled variables

$$w = \frac{m}{M}, \quad M\Omega_{\pm}(w) = \omega_m^{\pm}(Mw) \tag{4.1}$$

and set $p_n(v,w,t) = P(v,n,Mw,t)$. In order for the system-size expansion to be valid, it is important to note that the transition rates $\omega_m^{\pm}$ scale as specified. It is straightforward to check that this condition is satisfied for our model. Thus we rewrite Eq. (3.4) as

$$\begin{aligned}\frac{\partial p_n}{\partial t} &= -\frac{\partial}{\partial v}\{I_n(v,w)p_n(v,w,t)\} + \frac{1}{\epsilon}[\omega_n^{+}(v,n-1)\\ &\times p_{n-1}(v,w,t) + \omega_n^{-}(v,n+1)p_{n+1}(v,w,t)]\\ &- \frac{1}{\epsilon}\{[\omega_n^{+}(v,n) + \omega_n^{-}(v,n)]p_n(v,w,t)\} - M\{[\Omega_{+}(v,w)\\ &+ \Omega_{-}(v,w)]p_n(v,w,t)\}\\ &+ M\left\{\left[\Omega_{+}\left(v,w-\frac{1}{M}\right)p_n\left(v,w-\frac{1}{M},t\right)\right.\right.\\ &\left.\left.+ \Omega_{-}\left(v,w+\frac{1}{M}\right)p_n\left(v,w+\frac{1}{M},t\right)\right]\right\},\end{aligned} \tag{4.2}$$

where

$$I_n(v,w,t) = wf_{\mathrm{K}}(v) + \frac{n}{N}f_{\mathrm{Na}}(v) + f_L(v) + I_{\mathrm{app}}. \tag{4.3}$$

Note that for M sufficiently large, w can be treated as a continuous variable, where $0 \leqslant w \leqslant 1$. Taylor expanding in $1/M$ to $O(1/M)$ yields

$$\begin{aligned}\frac{\partial p_n}{\partial t} &= -\frac{\partial}{\partial v}[I_n(v,w,t)p_n] - \frac{\partial}{\partial w}[B_{-}(v,w)p_n]\\ &+ \frac{1}{2M}\frac{\partial^2}{\partial w^2}[B_{+}(v,w)p_n] + \frac{1}{\epsilon}[\omega_n^{+}(v,n-1)p_{n-1}\\ &+ \omega_n^{-}(v,n+1)p_{n+1}] - \frac{1}{\epsilon}\{[\omega_n^{+}(v,n) + \omega_n^{-}(v,n)]p_n\},\end{aligned} \tag{4.4}$$

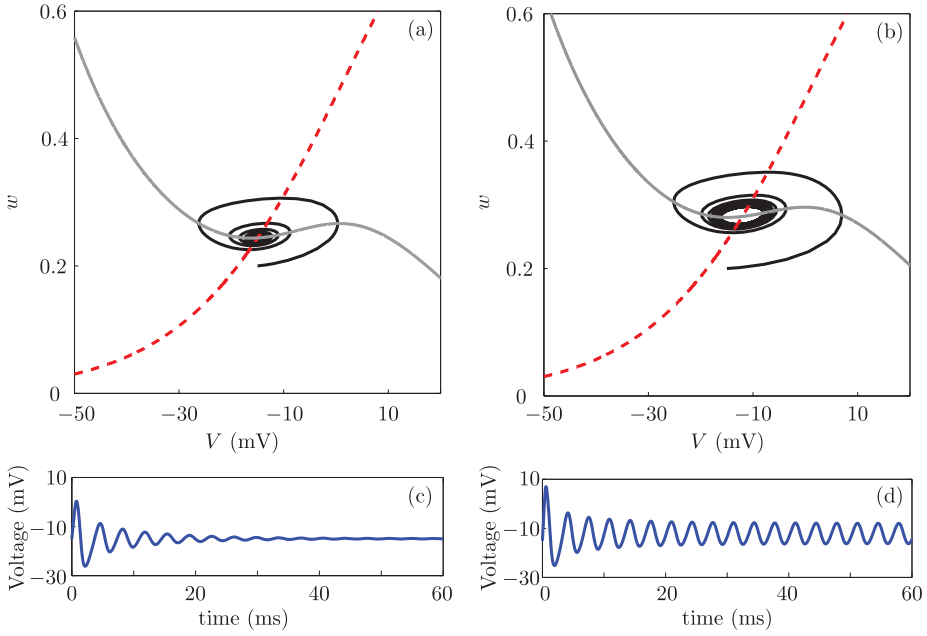

FIG. 2. (Color online) Phase plane diagrams of the deterministic model for (a) $I_{app} = 170$ pA (below the Hopf bifurcation point) and (b) $I_{app} = 190$ pA (above the Hopf bifurcation point). The dashed (red) curve is the w nullcline and the solid (gray) curve represents the v nullcline. The intersection of nullclines is the fixed point (v^{*}, w^{*}). (c) and (d) Corresponding voltage time courses.

where

$$B_-(v,w) = \Omega_+ - \Omega_-, \quad B_+(v,w) = \Omega_+ + \Omega_-. \tag{4.5}$$

Note that the system-size expansion has replaced the jump-Markov process for the K^+ channels by a continuous diffusionlike process for the fraction of open K^+ channels. The variance associated with the stochastic K^+ channels scales as $\sigma_K^2 \sim M^{-1}$. One could proceed in a similar fashion for the Na^+ ion channels by carrying out a system-size expansion with respect to N. This would then lead to a multivariate FP equation for the three variables v, w, and a, where a is the fraction of open Na^+ ion channels. Note in particular that the variance associated with the stochastic Na^+ channels would scale as $\sigma_{Na}^2 \sim (\epsilon N)^{-1}$. Since $\epsilon \ll 1$ and $N \ll M$, it immediately follows that the main source of channel noise arises from the persistent Na^+. In this paper we wish to develop an alternative approximation of the stochastic hybrid system that preserves the planar nature of the deterministic ML model. We will make use of the fact that the Na^+ jump process is much faster than potassium or voltage to perform a QSS approximation, also known as the adiabatic approximation [1,26,35].

V. QUASI-STEADY-STATE DIFFUSION APPROXIMATION OF SODIUM

Let $W_{nj}(v)$ be the voltage-dependent transition matrix for the Na^+ jump process, that is,

$$W_{nj}(v) = \omega_n^+(v,n-1)\delta_{j,n-1} + \omega_n^-(v,n+1)\delta_{j,n+1} - [\omega_n^+(v,n) + \omega_n^-(v,n)]\delta_{j,n}.$$

Rewrite Eq. (4.4) using this transition matrix

$$\frac{\partial p_n}{\partial t} = -\frac{\partial}{\partial v}[I_n(v,w)p_n] - \frac{\partial}{\partial w}[B_-(v,w)p_n] + \frac{1}{2M}\frac{\partial^2}{\partial w^2}[B_+(v,w)p_n] + \frac{1}{\epsilon}\sum_j W_{nj}(v)p_j. \tag{5.1}$$

For fixed values of v, the transition matrix $W_{nj}(v)$ is irreducible. By the Perron-Frobenius theorem, W has a simple zero eigenvalue, with all others having a negative real part. This implies that there exists a unique right null vector $\rho_n(v)$ such that $\sum_j W_{nj}(v)\rho_j(v) = 0$. Furthermore, $(1,1,\ldots,1)^T$ is the left null vector of W, so $\sum_n W_{nj}(v) = 0$ for all n. For fixedv,w, it can be shown that the Markov process for sodium

$$\frac{dp_n}{dt} = \frac{1}{\epsilon}[\omega_n^+(v,n-1)p_{n-1} + \omega_n^-(v,n+1)p_{n+1}] - \frac{1}{\epsilon}\{[\omega_n^+(v,n) + \omega_n^-(v,n)]p_n\} \tag{5.2}$$

has a globally attracting steady state $\rho(v,n) = \rho_n$ such that [27]

$$\rho_n = \frac{N!}{n!(N-n)!}\frac{\alpha_{Na}^n \beta_{Na}^{(N-n)}}{(\alpha_{Na}+\beta_{Na})^N}. \tag{5.3}$$

Since Na^+ is fast, there are many open-close transitions in n while the voltage v and w change very little. Thus we expect that the system will converge to the sodium QSS ρ_n, which will be perturbed as v and w evolve. This can be analyzed using a QSS approximation.

First, we decompose the probability density p_n such that

$$p_n(v,w,t) = C(v,w,t)\rho_n(v) + \epsilon x_n(v,w,t), \tag{5.4}$$

where

$$\sum_n p_n(v,w,t) = C(v,w,t), \quad \sum_n x_n(v,w,t) = 0.$$

Substituting Eq. (5.4) into Eq. (5.1), the CK equation now reads

$$\rho_n\frac{\partial C}{\partial t} + \epsilon\frac{\partial x_n}{\partial t} = -\frac{\partial}{\partial v}[CI_n\rho_n] - \epsilon\frac{\partial}{\partial v}[I_n x_n] + \mathbb{L}_w[\rho_n C + \epsilon x_n] + \sum_j W_{nj}x_j, \tag{5.5}$$

where

$$\mathbb{L}_w\psi(w) = -\frac{\partial}{\partial w}[B_-\psi(w)] + \frac{1}{2M}\frac{\partial^2}{\partial w^2}[B_+\psi(w)]. \tag{5.6}$$

Summing both sides over n and setting $\bar{I} = \sum_n I_n\rho_n$ yields

$$\frac{\partial C}{\partial t} = -\frac{\partial C\bar{I}}{\partial v} - \epsilon\frac{\partial \sum_n I_n x_n}{\partial v} + \mathbb{L}_w C. \tag{5.7}$$

We rewrite Eq. (5.5) by using Eq. (5.7) for $\partial C/\partial t$:

$$\epsilon\frac{\partial x_n}{\partial t} = \left(\frac{\partial C\bar{I}}{\partial v} + \epsilon\frac{\partial \sum_n I_n x_n}{\partial v}\right)\rho_n - \frac{\partial CI_n\rho_n}{\partial v} - \epsilon\frac{\partial I_n x_n}{\partial v} + \epsilon\mathbb{L}_w x_n + \sum_j W_{nj}x_j. \tag{5.8}$$

Introducing the asymptotic expansion $x \sim x^{(0)} + \epsilon x^{(1)} + \epsilon^2 x^{(2)} + \cdots$ and considering only $O(1)$ terms gives

$$\sum_j W_{nj}x_j^{(0)} = -\frac{\partial C\bar{I}}{\partial v}\rho_n + \frac{\partial CI_n\rho_n}{\partial v}. \tag{5.9}$$

From the Fredholm alternative theorem, Eq. (5.9) has a solution of the form

$$x_j^{(0)} = \sum_j W_{jn}^\dagger\left(-\frac{\partial C\bar{I}}{\partial v}\rho_n + \frac{\partial CI_n\rho_n}{\partial v}\right), \tag{5.10}$$

where $W^\dagger$ is the pseudoinverse of W. Using this solution for $x^{(0)}$ as a leading-order approximation for x_n in (5.7) gives the Fokker-Planck equation

$$\frac{\partial C}{\partial t} = -\frac{\partial}{\partial v}\left(\left\{\bar{I} - \epsilon\sum_n\left[\bar{I}\frac{\partial}{\partial v}\left(I_n\sum_j W_{jn}^\dagger\rho_n\right) - I_n\rho_n\frac{\partial}{\partial v}\left(I_n\sum_j W_{jn}^\dagger\right)\right]\right\}C\right) - \frac{\partial}{\partial w}[B_-C] + \frac{1}{2M}\frac{\partial^2 B_+C}{\partial w^2} + \epsilon\frac{\partial^2}{\partial v^2}\left(\sum_{n,j} W_{jn}^\dagger I_n\rho_n(\bar{I} - I_n)C\right). \tag{5.11}$$

Letting

$$\mu_1 = \overline{I} - \epsilon \sum_n \left[\overline{I} \frac{\partial}{\partial v} \left(I_n \sum_j W^\dagger_{jn} \rho_n \right) - I_n \rho_n \frac{\partial}{\partial v} \left(I_n \sum_j W^\dagger_{jn} \right) \right], \tag{5.12a}$$

$$\mu_2 = B_-, \tag{5.12b}$$

$$D = \begin{pmatrix} \epsilon \sum_{n,j} W^\dagger_{jn} I_n \rho_n (\overline{I} - I_n) & 0 \\ 0 & B_+/2M \end{pmatrix}, \tag{5.12c}$$

we can simplify the Fokker-Planck equation as

$$\frac{\partial C}{\partial t} = -\sum_{i=1}^{2} \frac{\partial}{\partial z_i} \mu_i C + \sum_{i,i'=1}^{2} \frac{\partial^2}{\partial z_i \partial z_{i'}} D_{ii'} C, \tag{5.13}$$

which corresponds to the Langevin stochastic differential equation (SDE)

$$dz_i = \mu_i(\mathbf{z}) dt + \sum_{j=1}^{2} \sigma_{ij}(\mathbf{z},t) dW_j \quad \text{for } i = 1,2, \tag{5.14}$$

where $\mathbf{z} = (v,w)$,

$$\sigma = \begin{pmatrix} \sqrt{2D_{11}} & 0 \\ 0 & \sqrt{2D_{22}} \end{pmatrix}, \tag{5.15}$$

and W_j is a Wiener process such that $\langle W_j(t) \rangle = 0$ and $\langle W_j(t) W_{j'}(t') \rangle = \delta_{jj'} \min(t,t')$. In terms of the original model parameters, we find that

$$D_{11} = \frac{1}{N} f_{\rm Na}(v)^2 a_\infty(v)[1 - a_\infty(v)]^2$$

and

$$D_{22} = w\beta_{\rm K} + (1-w)\alpha_{\rm K}(v).$$

The latter result was previously obtained by Fox and Lu [6] and the former by Keener and Newby [26]. Equation (5.14) can now be linearized about the stable rest state by letting $z_j = z_j^* + \epsilon \eta_j(t)$ where $\mu_j(\mathbf{z}^*) = 0$. Taylor expanding to $O(\epsilon)$ yields

$$d\eta_i(t) = \sum_{j=1}^{2} A_{ij} \eta_j + \sum_{j=1}^{2} \sigma_{ij}(\mathbf{z}^*) dW_j, \tag{5.16}$$

where A_{ij} is the Jacobian of the drift terms such that

$$A_{ij} = \left. \frac{\partial \mu_i}{\partial z_j} \right|_{\mathbf{z}^*}.$$

Finally, introducing white noise processes $\xi_j(t)$ such that $dW_j(t) = \xi_j(t) dt$ with $\langle \xi_j(t) \rangle = 0$ and $\langle \xi_j(t) \xi_{j'}(t') \rangle = \delta_{jj'} \delta(t-t')$ allows us to formally write the SDE as

$$\frac{d\eta_i(t)}{dt} = \sum_{j=1}^{2} A_{ij} \eta_j + \sum_{l=1}^{2} \sigma_{il}(\mathbf{z}^*) \xi_l. \tag{5.17}$$

VI. QUASICYCLES IN THE STOCHASTIC MODEL

Using our linear SDE (5.17), we can now look for oscillations in either voltage or potassium dynamics by obtaining analytical expressions for the power spectra. Let $\widetilde{\eta}_j(\omega)$ denote the Fourier transform of $\eta_j(t)$, i.e.,

$$\widetilde{\eta}_j(\omega) = \int_{-\infty}^{\infty} e^{-i\omega t} \eta_j(t) dt. \tag{6.1}$$

Here we follow standard steps to derive power spectra, as in [31,32]. Taking the Fourier transform of (5.17) yields

$$\widetilde{\eta}_j(\omega) = \sum_{i=1}^{2} \Phi^{-1}_{ij}(\omega) \sigma_{ij} \widetilde{\xi}(\omega), \tag{6.2}$$

where $\Phi_{ij} = -i\omega\delta_{i,j} - A_{ij}$. Recall that the power spectrum $P_i(\omega)$ is defined such that $2\pi\delta(0) P_i(\omega) = \langle |\widetilde{\eta}_j(\omega)|^2 \rangle$. Using Eq. (6.2), we obtain the power spectrum for the stochastic ML model

$$P_i(\omega) = \sum_j \sum_k \Phi^{-1}_{ij}(\omega) D_{jk} (\Phi^\dagger)^{-1}_{ki}(\omega), \tag{6.3}$$

where we have used $\Phi_{ij}(-\omega) = \Phi^\dagger_{ji}(\omega)$. It is worth mentioning that when comparing the analytical power spectrum to one that is generated numerically, one must take care to include a proportionality factor. This arises from the use of the discrete Fourier transform when computing numerical spectra and is equal to a time increment of Δt in the time series. A peak in the voltage power spectrum for $\omega \neq 0$ indicates that the voltage is oscillating with frequency ω.

As can be seen in Fig. 3, the spectrum of voltage when $I_{\rm app} = 150$ in the model shows a maximum around the Hopf frequency $\omega_c = 1.51$. This means that the model exhibits subthreshold oscillations at this frequency, despite the fact that this is well below the supercritical Hopf bifurcation point. In other words, channel noise from the stochastic opening and closing of Na^+ and K^+ channels is driving subthreshold oscillations outside the deterministic regime. We also compare our analytic power spectrum against numerical estimates of the power spectrum obtained using the Gillespie algorithm [37] and find good agreement. Next we explore the range of applied current for which the membrane potential exhibits a subthreshold oscillation. With channel noise, we first see the emergence of oscillatory behavior for $I_{\rm app} = 93$. Including channel noise from stochastic K^+ and Na^+ channels increases both the range of applied currents for which subthreshold oscillations are present and the range of frequencies of these subthreshold oscillations (Fig. 4). This analysis provides support for the claim that channel noise increases a neuron's ability to produce subthreshold oscillations, particularly for stimuli that are weak.

As we already highlighted in Sec. IV within the context of a double system-size expansion, we expect the contribution of Na^+ channel noise to be dominant. This is indeed found to be the case under our QSS approximation. The relative contribution of Na^+ versus K^+ channel noise can be quantified by looking at the magnitude of the respective diagonal terms in the diffusion matrix D (see Fig. 5). With physiological parameter values ($\epsilon \in [10^{-3}, 10^{-2}], N \sim 10^3$), D_{11}, the term in the diffusion matrix affected by N and ϵ (and thus Na^+), is orders of magnitude larger than D_{22}. Therefore, in this parameter regime, Na^+ channel noise is dominant. While fixing N and ϵ we asked whether there was a physiologically plausible number of K^+ channels M that would allow for Na^+

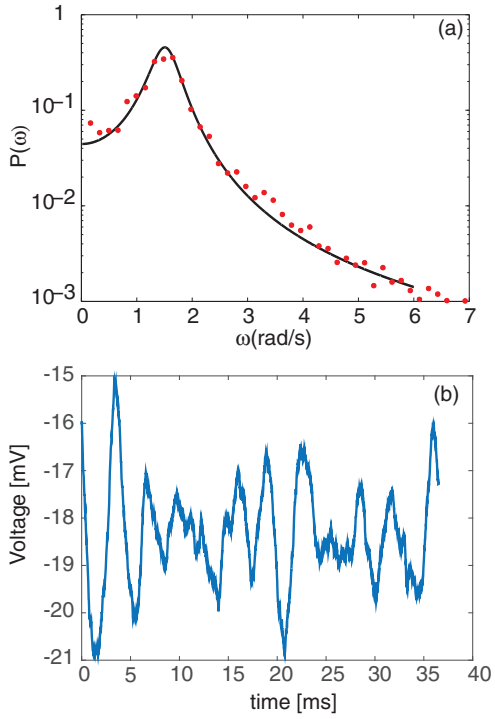

FIG. 3. (Color online) (a) Power spectrum of the voltage in the stochastic hybrid ML model for $I_{app} = 150$. The spectrum has a well-defined peak around the Hopf frequency $\omega_c = 1.51$ rad/s, indicating the presence of oscillations (quasicycles) below the supercritical Hopf bifurcation point. Filled (red) circles are from numerical simulations via the Gillespie algorithm, whereas the black solid line is the analytical prediction. The simulation values are $N = 10^3$, $M = 10^4$, and 50 trials. (b) Time domain response of voltage for a particular realization of the simulation shows STO-like behavior.

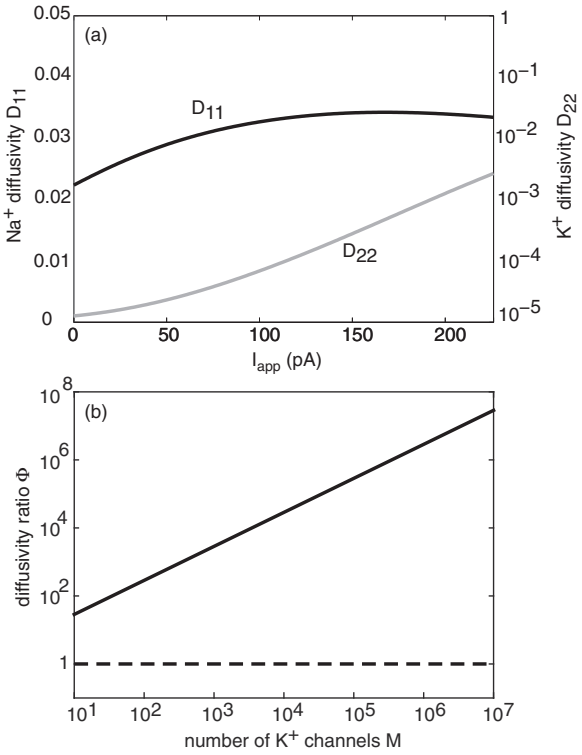

FIG. 5. Comparison of the contribution of Na^+ and K^+ channel noise to the diffusion term in the SDE. (a) Comparing D_{11} and D_{22}, with $N = 10^3$, $M = 10^4$, and $\epsilon = 10^{-2}$. Here D_{11} (and thus the contribution of Na^+ channel noise) is orders of magnitude larger for all values of I_{app}. (b) Fixing $\epsilon = 10^{-2}$ and $N = 1000$, there are no values of $M > 10$ such that the magnitudes D_{11} and D_{22} are comparable, i.e., the ratio $\Phi = D_{11}/D_{22}$ is always greater than 1 (dotted black line).

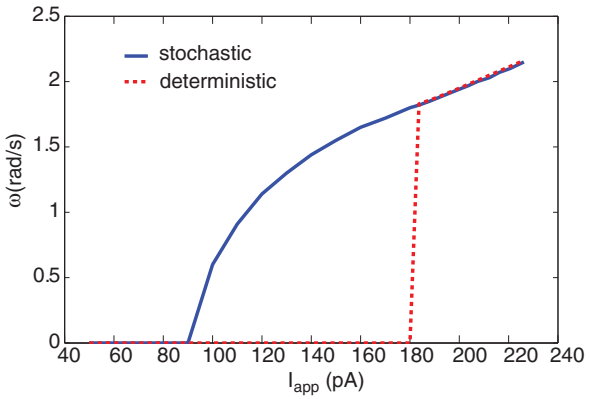

FIG. 4. (Color online) Channel noise increases the range of applied current values for which subthreshold oscillations exist. It also increases the range of frequencies that the model may produce. Frequency of oscillation ω is defined as the maximum of the power spectrum $P(\omega)$ for a given I_{app}. Here $N = 10^3$, $M = 10^4$, and $\epsilon = 10^{-3}$.

and K^+ channel noise to have a comparable effect. As shown in Fig. 5, the neuron would have to have fewer than ten K^+ channels for this to be the case. This leads us to the conclusion that fast Na^+ channel dynamics are the primary source of channel noise.

Another factor that could be important is the degree of coherence of the noise-induced subthreshold oscillations as a function of applied current; only sufficiently coherent oscillations would allow for a synchronization code, for example. One measure of coherence is the so-called quality factor $Q = \omega_c/\Delta w$, where Δw is the bandwidth of the power spectrum and ω_c is the peak. In Fig. 6 we plot Q as a function of I_{app} for three cases: Na^+ channel noise, K^+ channel noise, and joint channel noise. It can be seen that over a wide range of I_{app}, the system with stochastic K^+ channels exhibits more coherent oscillations than the one with stochastic Na^+ channels. Interestingly, the Q factor itself exhibits some form of resonance, having a sharp peak at some critical value of the applied current.

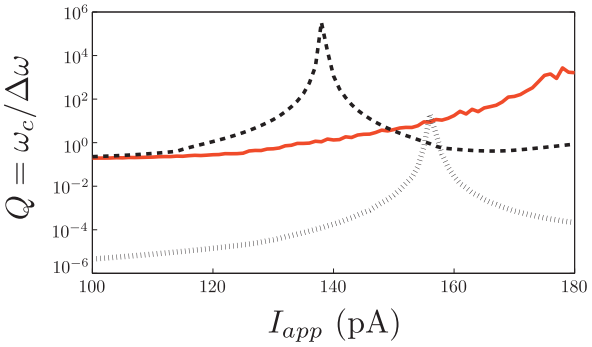

FIG. 6. (Color online) Quality factor $Q = \omega_c/\Delta\omega$ for the model with stochastic Na^+ channels only (black dashed line), stochastic K^+ channels only (gray dotted line), and both channel types stochastic (red solid line). Here ω_c is the the critical value of ω, i.e., the peak of the power spectrum $P(\omega)$, and $\Delta\omega$ is the bandwidth. With K^+ channel noise, the oscillations tend to be more coherent (larger Q factor). The parameter values are the same as in Fig. 4.

VII. DISCUSSION

In conclusion, we have shown how the noise-induced formation of STOs can be modeled in terms of the emergence of quasicycles in a stochastic hybrid ML model with both persistent sodium and potassium channel noise. This is consistent with biological data that show that channel noise enables a neuron's ability to generate subthreshold oscillations and enhance signal transduction over a wide range of parameter values. From a mathematical perspective, we have shown how one can preserve the low-dimensional (planar) structure of the deterministic ML model by carrying out a QSS approximation of the stochastic sodium channel dynamics. This method for reducing the dimensionality of the Langevin equation can be applied to any stochastic hybrid system with fast kinetics.

The computational advantages of the QSS method over a diffusion approximation based on a system-size expansion become particularly significant when the complexity of the ion channel model increases. As we highlighted in Sec. II, one major simplification of the stochastic ML model is to neglect that fact that ion channels typically have a subunit structure resulting in multiple states [25]. If these features were included, then the simple birth-death process used to describe the opening and closing of a two-state ion channel would need to be generalized to a more complicated multistate master equation. (It might be possible to obtain some simplifications by identifying invariant submanifolds of the stochastic dynamics [38].) Carrying out a system-size expansion of the resulting master equation would generate a high-dimensional Langevin equation that couples the voltage to additional variables representing the fraction of ion channels in each of the states. However, the numerical calculation of the associated diffusion matrix (or its square root) is numerically expensive. Fox and Lu [6] tackle this by approximating the multistate system in terms of uncoupled gating particles. However, such a simplification can lead to a breakdown of the diffusion approximation. More recently, a number of groups have shown that the diffusion approximation holds provided one considers coupled gating particles [11,39–41]. The QSS reduction is also a Gaussian approximation, but is based on a slow-fast decomposition rather than a system-size expansion, which eliminates the fraction of ion channels in each state as dynamical variables. Since the resulting Langevin equation is lower dimensional than in the case of the system-size expansion, one avoids the computational issues highlighted in Refs. [11,39–41]. On the other hand, the calculation of the pseudoinverse that determines the diffusion coefficient D_{11} in Eq. (5.13) could become computationally expensive as the complexity of the fast ion channel models increases.

Another possible extension of this work would be to consider the effects of noise-induced subthreshold oscillations on spontaneous action potentials (SAPs) by including a second class of nonpersistent Na^+ channels. The effects of channel noise on SAPs in excitable neuron models has recently been investigated within the context of noise-induced escape problems [1,26,27]. Diffusionlike approximations such as the system-size expansion and QSS analysis break down for such problems and one has to use alternative methods such as Wentzel-Kramers-Brillouin and large-deviation theories.

ACKNOWLEDGMENTS

P.C.B. was supported by the National Science Foundation (Grant No. DMS-1120327) and H.A.B. by the National Science Foundation (Grant No. RTG-1148230).

[1] P. C. Bressloff, *Stochastic Processes in Cell Biology* (Springer, Basel, 2014).
[2] A. A. Faisal, L. P. J. Selen, and D. M. Wolpert, Nat. Rev. Neurosci. **9**, 292 (2008).
[3] J. A. White, J. T. Rubinstein, and A. R. Kay, Trends Neurosci. **23**, 131 (2000).
[4] P. N. Steinmetz, A. Manwani, C. Koch, M. London, and I. Segev, J. Comput. Neurosci. **9**, 133 (2000).
[5] B. Sakmann and E. Neher, *Single-Channel Recording*, 2nd ed. (Plenum, New York, 1995).
[6] R. F. Fox and Y. N. Lu, Phys. Rev. E **49**, 3421 (1994).
[7] C. C. Chow and J. A. White, Biophys. J. **71**, 3013 (1996).
[8] K. Diba, H. A. Lester, and C. Koch, J. Neurosci. **24**, 9723 (2004).
[9] G. A. Jacobson, K. Diba, A. Yaron-Jakoubovitch, Y. Oz, C. Koch, I. Segev, and Y. Yarom, J. Physiol. **564**, 145 (2005).
[10] M. H. Kole, S. Hallermann, and G. J. Stuart, J. Neurosci. **26**, 1677 (2006).
[11] J. H. Goldwyn, N. S. Imennov, M. Famulare, and E. Shea-Brown, Phys. Rev. E **83**, 041908 (2011).
[12] E. Schneidman, B. Freedman, and I. Segev, Neural Comput. **10**, 1679 (1998).
[13] A. D. Dorval, Neuroscientist **12**, 442 (2006).
[14] A. A. Faisal, J. A. White, and S. B. Laughlin, Curr. Biol. **15**, 1143 (2006).

[15] X. J. Wang, Neuroreport **5**, 221 (1993).
[16] A. Alonso and R. R. Llinas, Nature (London) **342**, 175 (1989).
[17] R. R. Llinas, A. A. Grace, and Y. Yarom, Proc. Natl. Acad. Sci. U.S.A. **88**, 897 (1991).
[18] J. A. White, R. Klink, A. Alonso, and A. R. Kay, J. Neurophysiol. **80**, 262 (1998).
[19] R. Amir, C. N. Liu, J. D. Kocsis, and M. Devor, Brain **125**, 421 (2002).
[20] A. Reboreda, E. Sanchez, M. Romero, and J. A. Lamas, J. Physiol. **551**, 191 (2003).
[21] D. T. W. Chik, Y. Wang, and Z. D. Wang, Phys. Rev. E **64**, 021913 (2001).
[22] B. Ermentrout and D. Terman, *Mathematical Foundations of Neuroscience* (Springer, New York, 2010).
[23] C. Morris and H. Lecar, J. Biophys. **35**, 193 (1981).
[24] J. A. White, T. Budde, and A. R. Kay, Biophys. J. **69**, 1203 (1995).
[25] G. D. Smith, in *Modeling the Stochastic Gating of Ion Channels*, edited by C. Fall, E. S. Marland, J. M. Wagner, and J. J. Tyson (Springer, New York, 2002), Chap. 11.
[26] J. P. Keener and J. M. Newby, Phys. Rev. E **84**, 011918 (2011).
[27] J. M. Newby, P. C. Bressloff, and J. P. Keener, Phys. Rev. Lett. **111**, 128101 (2013).
[28] A. D. Dorval and J. A. White, J. Neurosci. **25**, 10025 (2005).
[29] U. Kummer, B. Krajnc, J. Pahle, A. K. Green, C. J. Dixon, and M. Marhl, Biophys. J. **89**, 1603 (2005).
[30] A. J. McKane, J. D. Nagy, T. J. Newman, and M. O. Stefanini, J. Stat. Phys. **128**, 165 (2007).
[31] R. P. Boland, T. Galla, and A. J. McKane, J. Stat. Mech. (2008) P09001.
[32] P. C. Bressloff, Phys. Rev. E **82**, 051903 (2010).
[33] J. Realpe-Gomez, T. Galla, and A. J. McKane, Phys. Rev. E **86**, 011137 (2012).
[34] A. Juel, A. G. Darbyshire, and T. Mullin, Proc. R. Soc. London Ser. A **453**, 2627 (1997).
[35] C. Gardiner, *Handbook of Stochastic Methods*, 4th ed. (Springer, Berlin, 2009).
[36] T. G. Kurtz, Math. Prog. Stud. **5**, 67 (1976).
[37] D. T. Gillespie, J. Phys. Chem. **81**, 2340 (1977).
[38] B. A. Earnshaw and J. P. Keener, SIAM J. Appl. Dyn. Syst. **9**, 220 (2010).
[39] D. Linaro, M. Storace, and M. Giugliano, PLoS Comput. Biol. **7**, e1001102 (2011).
[40] P. Orio and D. Soudry, PLoS ONE **7**, e36670 (2012).
[41] D. Pezo, D. Soudry, and P. Orio, Front. Comput. Neurosci. **8**, 139 (2014).

CHAPTER 7

FUTURE DIRECTIONS

In this chapter, we conclude by describing plans for current and future work that are not direct extensions of the previously discussed projects. In Section 7.1, we describe an ongoing collaboration that explores the effects of grooming and social dynamics on parasite spread in dynamic population networks. In Section 7.2, we discuss a proposed research plan to solve the open problem in applied dynamical systems to prove the existence of snaking bifurcations, which lead to localized patterns on lattices.

7.1 Parasite spread on dynamic social networks

Allogrooming (that is, social grooming between members of the same species) has been observed across a wide variety of social animal populations. One of the potential benefits of allogrooming is the mitigation of ectoparasite infection. While there is a large body of research developing and analyzing mathematical models of the spread of pathogen infection dating as far back as Kermack and McKendrick in 1927 [11], to the best of our knowledge there is little work applying mathematical techniques to the dynamics of ectoparasite spread in a population. In this section, we discuss some simple mathematical models of the impact of allogrooming behavior on dynamic social networks and propose to tackle this problem in future work with a combination of differential equation and agent-based models. The work described in this section is from an ongoing collaborative project with Maryann Hohn, Candice Price, Ami Radunskaya, Suzanne Sindi, Nakeya Williams, Shelby Wilson, and Nina Fefferman.

In previous work, we began our exploration on the spread of parasites in social networks by considering a simple model of ectoparasitic infection in a population network. This initial formulation consisted of a two-compartment model depicting the exchange of ectoparasites among individuals with no social hierarchy (*i.e.* each individual, on average, has the same number of grooming connections, as in Figure 7.1). Rather than model the

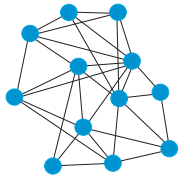

Figure 7.1. A random social network with only periphery nodes (blue).

parasite burden of individual as a node in a network, we considered all individuals that are in either an infected (I) or uninfected (U) state. Individuals may move between states through social contact and allogrooming. As mentioned, we neglected the explicit network structure and modeled the expected movement between compartments by averaging over the expected number of contacts between individuals in the I and U states.

Let P_U represent the number of parasite-free individuals and P_I represent the number of infected individuals. Uninfected individuals can become infected through their interactions with infected individuals, and infected individuals can become uninfected through grooming, with grooming efficiency parameter g (Figure 7.2). Note that the function f represents the likelihood of infection and depends on the individual fitness and the average number of infected connections. We take $n \in \{1, \ldots, N-1\}$ to be the number of grooming connections each individual has. Translating Figure 7.2 into a system of ordinary differential equations yields

$$P'_U(t) = -f(P_I)P_U + ngP_I \tag{7.1}$$

$$P'_I(t) = f(P_I)P_U - ngP_I. \tag{7.2}$$

Because this model neglects population birth and death, the number of individuals remains conserved, namely $N = P_U + P_I$. This conservation allows us to reduce the system

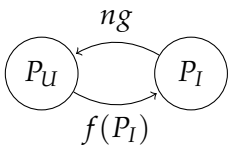

Figure 7.2. Simplified model of ectoparasites in a population lacking social hierarchy consisting of infected (I) and uninfected (U) individuals.

dynamics to a single differential equation, where we track only the number of infected individuals

$$P_I'(t) = f(P_I)(N - P_I) - ngP_I. \tag{7.3}$$

It remains to define the functional form of the infection rate function $f(P_I)$. In a full dynamic network, each node randomly chooses n connections out of $N-1$ possible options, of which $\frac{P_I}{N-1}$ are infected. Thus, the number of infected connections an uninfected individual has can be represented as a hypergeometric random variable X. In order to represent this in a deterministic ordinary differential equation model (*i.e.* with no random variables), we calculate the expected number of infected connections $\mathbb{E}[X] = \overline{X} = n\frac{P_I}{N-1}$. In the spirit of making the analysis as simple as possible for our first model, we define f to be the linear function

$$f(P_I) = \frac{1}{x_0}\overline{X} = n\frac{P_I}{x_0(N-1)}.$$

While this function is purposefully simple, it does have two important properties: (1) $f(0) = 0$, so individuals cannot become infected if they have no infected connections, and (2) it is an increasing function of P_I. The constant x_0 controls the steepness of the function, with larger values of x_0 representing a larger individual defense against parasites (or alternatively, this means the infected connections have a weaker effect). We chose to write the slope as $1/x_0$ instead of x_0 for ease of interpretation of results.

We investigate the long-term dynamics of Equation (7.3). After rescaling the variables by population size such that $p_i = \frac{P_I}{N}$, we show that Equation (7.3) has only two possible steady states:

$$(1)\ p_I^* = 0 \text{ and } (2)\ p_I^* = 1 - gx_0\left(1 - \frac{1}{N}\right).$$

Steady state (1) corresponds to no parasite infection in the population, and (2) indicates a co-existence of the infected and uninfected states in the population. We note this interpretation changes when $g = 0$, that is, there is no grooming effectiveness. In this case, the steady state represents a fully infected population.

The stability of these steady states depends on the term $gx_0\left(1 - \frac{1}{N}\right)$, which serves as the bifurcation parameter for this system. This system undergoes a transcritical bifurcation at $gx_0 = \frac{N}{N-1}$. When $gx_0 < \frac{N}{N-1}$, the uninfected state is unstable and the coexisting state is stable. In this case, we expect to see lasting infection in a proportion of the population.

At the bifurcation point $gx_0 = \frac{N}{N-1}$, the no-infection case is the only steady state, and it is marginally stable (effectively, it is stable in this context because it is stable to positive perturbations). When $gx_0 > \frac{N}{N-1}$, the coexisting state is unstable and the uninfected state is stable. In this case, we expect to see no lasting infection in the population.

This analysis suggests (unsurprisingly) that higher grooming effectiveness contributes to parasite eradication. Without grooming, a parasite-free state is unstable. Similarly, having a strong individual defense contributes positively to parasite eradication. Since the stability of the parasite-free state is determined by the product of grooming and individual defense, this implies there are multiple successful strategies that can be employed by social groups to manage ectoparasite infestation: Being good at grooming allows the individuals to have less individually-derived parasite defense; conversely, if you aren't particularly good at grooming, you need to have more effective individual physiological defenses. Interestingly, the number of grooming connections does not affect the outcome of this system, but if your population is very small, it may be more difficult to manage infections.

We then compared these results with a more complex model depicting social hierarchy arising from a hub-periphery social network, as demonstrated in Figure 7.3. We chose this form of hierarchy to depict the structure of dynamic social networks where individuals chose their connections to maximize a given centrality measure (*e.g.*, degree). In these cases, networks converge to a network topology where a subset of nodes called "hubs" are connected with all other nodes [7]. We model this network structure as follows: Suppose there are N_h hub individuals and N_p periphery individuals such that $N = N_h + N_p$. Let H_U be the uninfected hub individuals and H_I the infected hub individuals; likewise P_U represents the uninfected periphery individuals and P_I the infected periphery individuals.

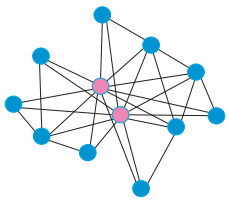

Figure 7.3. A small-world network with $N_p = 10$ periphery nodes (blue) and $N_h = 2$ hub nodes (pink).

A schematic diagram of this model is provided as Figure 7.4.

Once again, the likelihood of infection is determined by the function f, which depends on individual fitness and the average number of infected connections (this time in both hub and periphery categories). The equations for this system are as follows:

$$\begin{aligned} P_U'(t) &= -f_p(P_I, H_I)P_U + ngP_I \\ P_I'(t) &= f_p(P_I, H_I)P_U - ngP_I \\ H_U'(t) &= -f_h(P_I, H_I)H_U + (N-1)gH_I \\ H_I'(t) &= f_h(P_I, H_I)H_U - (N-1)gH_I, \end{aligned}$$

where, as before, we can employ the two conserved quantities $P_U + P_I = N_p$ and $H_U + H_I = N_h$ to reduce our system to

$$\begin{aligned} P_I'(t) &= f_p(P_I, H_I)(N_p - P_I) - ngP_I \\ H_I'(t) &= f_h(P_I, H_I)(N_h - H_I) - (N-1)gH_I. \end{aligned}$$

Notice that, in this case, the infectivity function f is different for hub versus periphery individuals. Now that we have hub individuals, our number of connections is $n = N_h + k$, where we use k to represent the number of periphery-periphery connections. If an individual is in the periphery, then the expected number of infected connections is

$$\overline{X}_P = H_I + k\frac{P_I}{N_p - 1},$$

and if the individual is in the hub, then

$$\overline{X}_H = H_I + P_I.$$

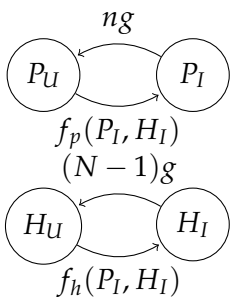

Figure 7.4. Schematic of simplified model of parasite spread in a population with hub-periphery social structure.

If we use the same functional form for infectivity as in the previous case, this implies that

$$f_p(P_I, H_I) = \frac{H_I + k\frac{P_I}{N_p - 1}}{x_0},\ f_h(P_I, H_I) = \frac{H_I + P_I}{x_0}.$$

Using these two functions, and applying the two conserved quantities $P_U + P_I = N_p$ and $H_U + H_I = N_h$, we can reduce our system to the following system of two ODEs:

$$\begin{aligned} p_I'(t) =& \frac{(1 - p_I)}{x_0}(N_h h_I + \frac{kN_p}{N_p - 1} p_I) - (N_h + k) g p_I \\ h_I'(t) =& \frac{(1 - h_I)}{x_0}(N_h h_I + N_p p_I) - (N_p + N_h - 1) g h_I, \end{aligned} \tag{7.4}$$

where, as before, we have rescaled the variables such that $p_I = P_I/N_p$ and $h_I = H_I/N_h$.

For comparison, we want to perform a linear stability analysis on the noninfected steady state $(0, 0)$. The nullclines of the system (shown in Figure 7.5) are given by:

$$\begin{aligned} p_I - \text{null} \quad &: \quad h_I = p_I \left(\left(\frac{N_h + k}{N_h} \right) \frac{g x_0}{1 - p_I} - \frac{kN_p}{N_h(N_p - 1)} \right) \\ h_I - \text{null} \quad &: \quad p_I = h_I \left(\left(\frac{N - 1}{N_p} \right) \frac{g x_0}{1 - h_I} - \frac{N_h}{N_p} \right), \end{aligned}$$

where we have used the fact that $N = N_p + N_h$. Both nullclines are increasing and concave up in the dependent variable, (as written above), and they both go through the origin. Thus, they can have at most one nonzero intersection. This intersection will be in the positive quadrant when the slope of the p_I-nullcline at $(0, 0)$ is strictly less than the slope of the h_I-nullcline at $(0, 0)$, or when:

$$(g x_0)^2 - \left(\frac{N_h}{N - 1} + \frac{k}{n} \frac{N_p}{N_p - 1} \right) g x_0 + \frac{N_p N_h}{n(N - 1)} \left(\frac{k}{N_p - 1} - 1 \right) < 0 \tag{7.5}$$

Here we have used the fact that the total number of connections between nodes, n, satisfies: $n = N_h + k$. The nullclines of this system for two different parameter sets, along with some sample trajectories, are shown in Figure 7.5.

The Jacobian of this system evaluated at the steady state (0,0) is

$$J(0, 0) = \begin{pmatrix} \frac{k}{x_0} \left(1 - \frac{1}{N_p} \right)^{-1} - ng & \frac{N_h}{x_0} \\ \frac{N_p}{x_0} & \frac{N_h}{x_0} - (N - 1) g \end{pmatrix}.$$

The steady state is stable, that is, the eigenvalues of this matrix have negative real part, when $\text{Det}(J) > 0$ and $\text{Trace}(J) < 0$.

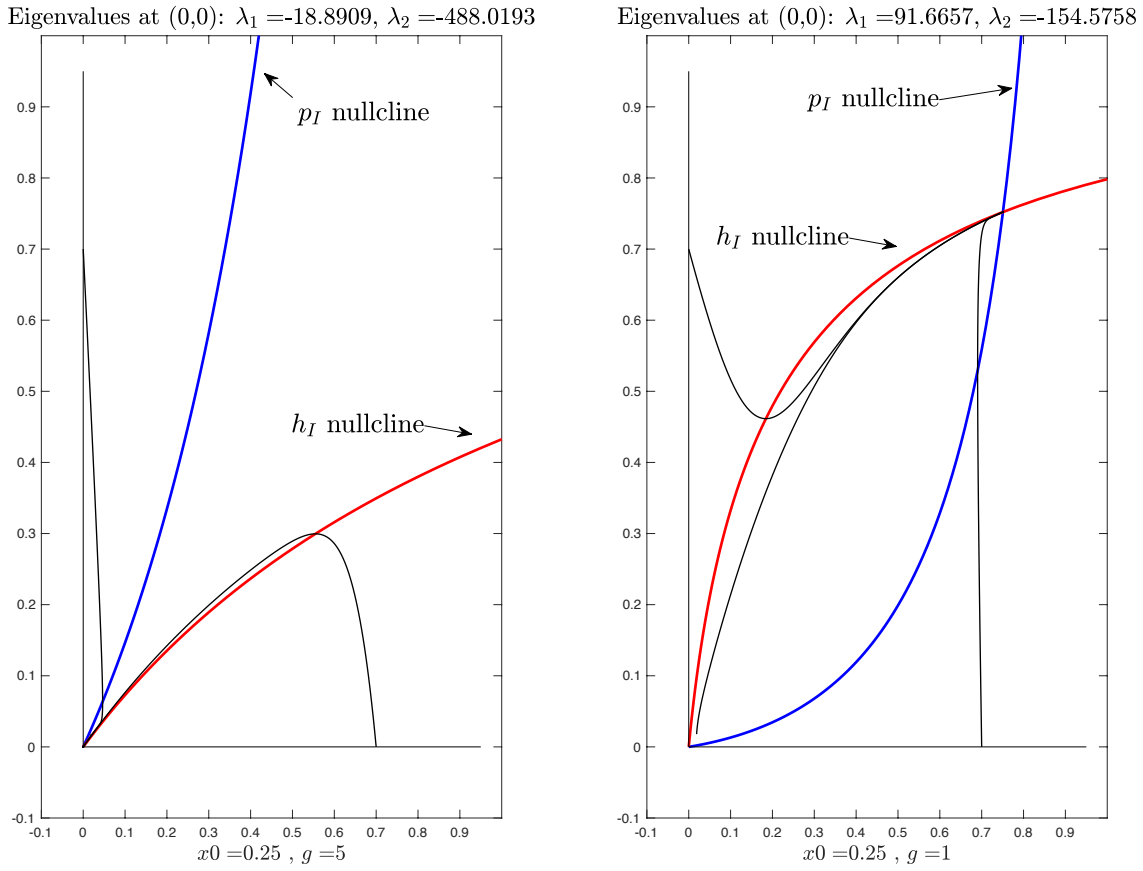

Figure 7.5. There are two qualitatively different phase portraits for the system. (Left): When grooming effectiveness, gx_0, is high, there is one biologically relevant equilibrium at (0,0) which is globally asymptotically stable. (Right): When grooming and individual resistance are less efficient, the nullclines intersect in the positive quadrant at a nonzero stable equilibrium. This equilibrium attracts all trajectories with initial values in $(0,1) \times (0,1)$ in the rescaled coordinates of Equation (7.4).

The first condition is analogous to the condition derived in Equation 7.5. The second condition yields

$$gx_0 > \frac{n + \frac{k}{N_p - 1}}{N + n - 1}.$$

It is clear that this second condition is less strict than in the periphery-only model since $\frac{N}{N-1} > \frac{n + \frac{k}{N_p-1}}{N+n-1}$ for all positive parameter values.

We use numerical simulation to aid in the interpretation of Equation (7.5). Figure 7.6 shows that, for reasonable parameter choices, the bifurcation value for stability of the uninfected state is smaller in the hub-periphery case than in the periphery-only case. Several

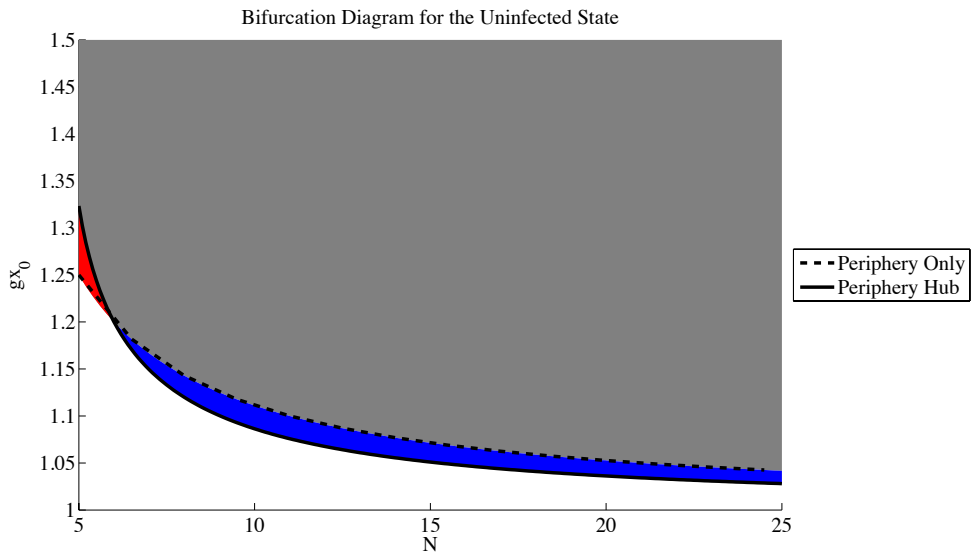

Figure 7.6. Stability conditions in (N, gx_0) parameter space for the uninfected state with $n = 5$ grooming connections. We plot the boundary condition for a population with no hub nodes (dashed) and with $N_h = 3$ hub nodes (solid). The uninfected state is stable above each curve. We see that the range of $(N, gx0)$ parameter space where the uninfected state is stable is smaller for the periphery-only model (gray area) than for the periphery-hub model (both the blue and gray areas).

studies have shown that hubs contribute to increased pathogen spread on networks by acting as super-spreaders of disease [8, 16]. However, in our model of parasite spread, we find a surprising result: the hub-periphery structure increased the basin of attraction for stability of the noninfected steady state as compared to the periphery only model. This means that our models suggests a potential evolutionary benefit from having the hub-periphery social structure frequently observed in animal populations; that is, the hub-periphery social structure reduced burden from ectoparasitic infections. Consideration of the relative intensities of selective pressures from pathogens versus parasites adds an intriguing and important new layer to the ongoing effort to understand what role disease may have played in the evolution of animal social systems.

7.1.1 Proposed problems for future work

Proposed Problem 1. *Explore the effects of varying parasite loads, grooming dynamics, individual fitness, and reproduction by analyzing extensions to the simple continuous model.* An interesting difference that distinguishes parasite infection from pathogen infection is that

different levels of parasite load have varying effects on an individual's fitness, whereas pathogen exposure is typically viewed as a binary (infected/uninfected). It is possible for an individual to have a small number of parasites and see no adverse effects on individual fitness; however, a large number of parasites may affect both individual fitness as well as ability to effectively groom others. In the extension of our ODE model, we will include multiple levels of parasite load, with each group subject to different levels of individual fitness and grooming efficiency. If we consider K possible infection load states, the system reads

$$\begin{aligned}
P_0'(t) &= -f_0(P_1,\ldots,P_K)P_0 + ng(P_0,\ldots,P_K)P_1 \\
&\vdots \\
P_j'(t) &= -f_j(P_{j+1},\ldots,P_K)P_j + f_{j-1}(P_j,\ldots,P_K)P_{j-1} + ng(P_0,\ldots,P_K)\left(P_{j+1}-P_j\right)\big) \\
&\vdots \\
P_K'(t) &= -ng(P_0,\ldots,P_K)P_K + f_{K-1}(P_K)P_{K-1}
\end{aligned}$$

for all $j \in [1, K-1]$. In future work, we will also consider a model where birth and death is included, meaning the population is no longer conserved. In this case, there is a source term for P_0 (healthy individuals can reproduce) and P_K is an absorbing state (individuals in state P_K die and are removed from the population). Developing and analyzing the extended model is important to aid in the understanding of how parasite infection might affect population dynamics on an evolutionary scale.

Additionally, we would like to investigate how the functional form of the fitness- and grooming-dependent transition rates affect the outcome of parasite load in the population. In previous work, we considered the infection transition function f to be a linear function with fitness parameter x_0. A natural question is to explore how and when the functional form of f affects the solutions to this system. We intend to analyze other monotonically increasing functions satisfying $f(0) = 0$, including step functions, piecewise linear functions, and logistic functions.

Furthermore, the transition functions will depend on whether we consider an undirected versus directed network. In the context of grooming, an undirected network indicates that social relationships provide reciprocal grooming, which is not guaranteed in the

directed network. The calculation to find the expected number of grooming connections in the directed network is outlined below.

Without loss of generality, we assume that grooming is represented by outgoing edges, so the *out degree* of each node is n. It's important to note that individuals can be exposed to parasites from any social contact, that is, grooming or being groomed. For this network, the average *in degree* is also n. However, one must be careful to not double count reciprocal grooming relationships. If we define Y to be the random variable that represents the number of reciprocal grooming relationships in a randomly connected population network, then by definition the average number of reciprocal grooms is

$$\mathbb{E}(Y) = \sum_{j=0}^{n} j\mathbb{P}(Y = j), \tag{7.6}$$

where $\mathbb{P}(Y = j)$ is the probability that the population contains j reciprocal grooming relationships.

$\mathbb{P}(Y = j)$ is calculated as follows. There are $\binom{N-1}{n}$ possible options for an individual's grooming connections. The probability of choosing j connections is found by considering that, out of the $N - 1 - k$ that aren't connected to the individual, $n - j$ are chosen. That is, there are $\binom{N-1-k}{n-j}$ ways to do so. Then, with your remaining j choices, there are $\binom{n}{j}$ ways to choose a grooming connection. This implies that

$$\mathbb{P}(Y = j) = \frac{\binom{n}{j} \cdot \binom{N-1-n}{n-j}}{\binom{N-1}{n}}. \tag{7.7}$$

Combining Equation 7.6 with Equation 7.7 yields

$$\mathbb{E}(Y) = \sum_{j=0}^{n} j \frac{\binom{n}{j} \cdot \binom{N-1-n}{n-j}}{\binom{N-1}{n}} = \frac{n^2}{N-1}.$$

Notice this has the desired asymptotic behavior: for $N \to \infty$, you would not expect to choose any reciprocal grooming partners. For $n = N - 1$, you expect all $N - 1$ of them to be reciprocal. Following this logic, the expected number of infected periphery connections is

$$[X] = \frac{P_i}{N-1}\left(2n - \frac{n^2}{N-1}\right) = \frac{nP_i}{N-1}\left(2 - \frac{n}{N-1}\right).$$

Exploration of this question will allow us to better understand the effects of the subtleties of population dynamics on parasite outbreaks.

Proposed Problem 2. *Develop a stochastic agent-based model of the full dynamic network and compare these results to continuous models.* As we are developing extensions to the continuous model we will be concurrently developing a stochastic agent-based simulation of the full dynamic population network. We will then be able to compare the simulation results against our analytic results obtained with the ODE models. This will give us the tools to either (a) validate the use of ODE models in this context, or (b) prove when the ODE models break down in representing dynamic networks. This question will help us inform the direction of future mathematical work comparing population networks and continuous models.

Using MATLAB, we will be developing an agent-based simulation that allows for both static and dynamic network structures. The goal is to explore how grooming effectiveness and parasite reproductive rate effect the parasite load on the entire network. Following a thorough search of the parameter space, we aim to investigate the differences in parasite distribution between dynamic and social networks in an effort to understand which social dynamics are best to minimize parasite load.

7.2 Localized patterns on lattices

It has been observed that systems with Turing instabilities can also support the formation of localized patterns. A localized pattern is a periodic pattern that does not extend throughout the entire domain but is instead surrounded by a spatially uniform background state [12, 6]; this indicates a coexistence of the spatially homogeneous state and the locally patterned state (Figure 7.7). It is important to note that these localized patterns arise despite the system being driven in spatially uniform manner. These patterns have been observed in applications as diverse as reaction-diffusion equations [14], the buckling of elastic beams [10], nonlinear optics [1], hydrodynamics [3], and ferrofluid instability [17]. Indeed, localized patterns are a general phenomenon in dissipative systems whose understanding is central to several areas of applied mathematics.

A well-studied example of a system that admits localized patterns is the Swift-Hohenberg equation

$$u_t = (1 + \partial_x^2)^2 u - \mu u + cu^3 - u^5, \quad x \in \mathbb{R},$$

where c is a positive constant and $\mu > 0$ is the bifurcation parameter. The bifurcation

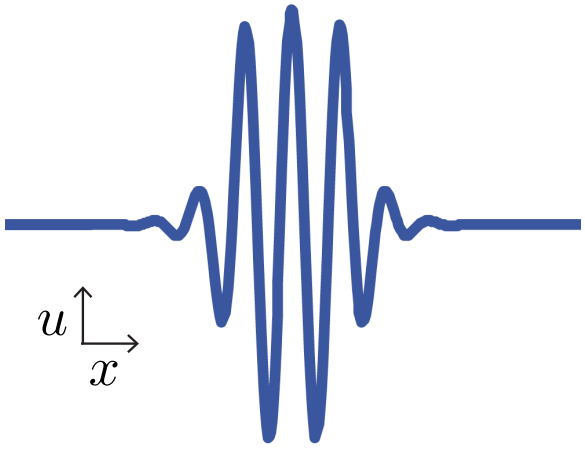

Figure 7.7. An example of a spatially localized pattern for a function $u(x)$. The periodic patterned state is pinned between the homogeneous background state.

structure of localized patterns in this system has been studied only comparatively recently; in 2006, Burke and Knobloch [5] calculated bifurcation diagrams of this equation using numerical continuation methods. When μ is plotted against the pattern size (*i.e.*, the L^2 norm) in the bifurcation diagram, these systems display a characteristic set of winding curves corresponding to the localized patterns. These structures are called *snaking bifurcations*. Since their discovery, some progress has been made in the analytical understanding of snaking bifurcations, notably by Beck and colleagues [4]. In this work, the authors are able to analytically investigate the existence of snaking of symmetric pulse patterns by exploiting the known bifurcation structure of front patterns. Despite this progress, there are still a number of open problems regarding snaking bifurcations of localized patterns in dissipative systems [12]. In particular, a numerical study due to Taylor and Dawes [18] suggested the existence of snaking bifurcations on 1- and 2-dimensional lattices. Furthermore, these localized patterns on lattices have been observed in the light field of an optical medium with periodic optical cavities [19, 20] and in crystallographic pinning [9]. Using analytical methods to prove the existence of snaking bifurcations on lattices remains an open problem, and I detail below some strategies to solve this problem.

7.2.1 Proposed problems for future work

Proposed Problem 1. *Demonstrate the existence of snaking bifurcations in the analog of the Swift-Hohenberg equation on a one-dimensional lattice. That is, examine an equation of the form*

$$\dot{u_n} = \alpha\left(u_{n+1} - 2u_n + u_{n-1}\right) - \mu u_n + 2u_n^3 - u_n^5, \quad (n \in \mathbb{Z}) \tag{7.8}$$

in the anticontinuum limit, and prove that patterns persist and yield a connected smooth snaking branch.

Initially, to make this problem more tractable, we will consider what happens in the anticontinuum limit $\alpha \to 0$ (*i.e.*, no spatial coupling between lattice points). As we take $\alpha \to 0$, then (7.8) satisfies the steady-state problem $\mu u_n - 2u_n^3 + u_n^5 = 0$. Thus, for $0 < \mu < 1$, there exist five possible solutions for each n: $u_n = \{0, \pm b(\mu), \pm a(\mu)\}$, where $b(\mu)$ and $a(\mu)$ are the (nonzero) $\mu-$dependent solution branches with $0 < b(\mu) < a(\mu)$ for all $\mu \in (0,1)$, as in Figure 7.8.

This allow us to construct the lattice version of a front pattern, that is,

$$u_n = \begin{cases} a(\mu) & n < N \\ b(\mu) & n = N \\ 0 & n > N \end{cases}.$$

As μ increases, the value $b(\mu)$ increases and approaches $a(\mu)$. At $\mu = 1$ (the saddle node branch), $u_N = a(\mu)$ and the plateau is broadened. If we continue to follow this solution branch by decreasing μ, the value $a(\mu)$ increases and our front solution has grown by adding an additional lattice point with the value $a(\mu)$. One can then construct the

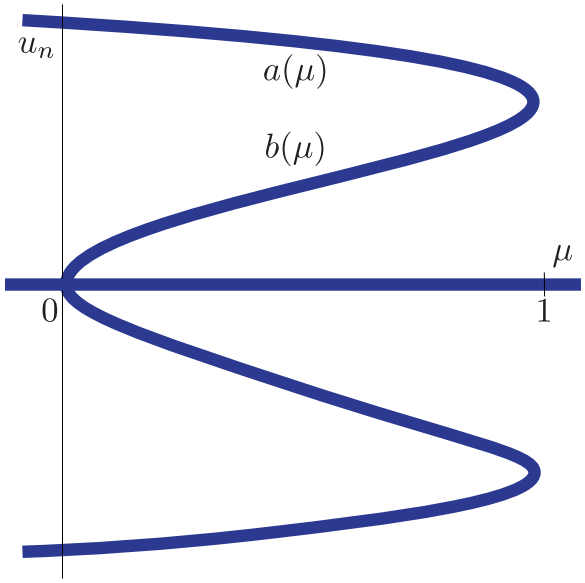

Figure 7.8. The bifurcation plot for the discrete Swift-Hohenberg equation.

bifurcation diagram where μ is plotted against the length of the pattern, here given by the discrete L^1-norm. This gives a snaking branch in the anticontinuum limit $\alpha = 0$.

The next step is to prove that these patterns persist and that they yield a connected smooth snaking branch. Away from $\mu = 0, 1$, persistence of the patterns follows from the implicit function theorem. Near $\mu = 0$ and $\mu = 1$, a Lyapunov-Schmidt reduction is necessary and the resulting lower dimensional system can be analyzed for persistence. Our preliminary calculations suggest that some branches yield snaking, while others do not.

Proposed Problem 2. *Analytically investigate the existence of snaking bifurcations in general one-dimensional discrete maps*

$$u_n = f(u_{n-1}, \mu), \text{ where } u_n \in \mathbb{R}^d \ \forall n.$$

In order to prove the existence of snaking for general maps, we want to find patterns that connect the fixed point $a(\mu)$ of the map to the fixed point 0. We will assume the existence of two saddles for all μ, and note that snaking bifurcations occur with the existence of intersections in the stable and unstable manifolds. This will occur between two values μ_1, μ_2, where the invariant manifolds have quadratic tangencies. Along the snaking branch, $L = L(\mu)$ increases.

The spirit of the proof will follow Beck et al. in [4]. However, in the discrete map setting, many of the techniques used in the continuous case do not apply. For example, one needs to examine the eigenvalues of the Jacobian of the maps instead of relying on Floquet multiplier arguments. We anticipate that one will need to apply a discrete Lin's method as discussed in [13].

Proposed Problem 3. *Carry out analysis in the anticontinuum limit for pattern persistence and stability on two-dimensional lattices*.

The next goal is to investigate localized pattern formation on two-dimensional lattices. Here, as in my previous work, choice of lattice will be important (square vs. hexagonal lattices), and we will study various forms of coupling that respect the D_4 and D_6 symmetries of these two lattices.

This problem contains several interesting mathematical challenges. First, there are many more types of patterns possible than in the one-dimensional case. Studying patterns

on two-dimensional lattices may help shed light on the complicated snaking of hexagon patches observed by [15] in the continuous case. On a related note, when we examine the bifurcation diagrams in these cases, there will likely be many asymmetric branches bifurcating off of the symmetric branch. Numerical continuation studies will help us gain insight here. It would be particularly interesting to investigate symmetry breaking perturbations, as they may lead to isolas as observed in the two-dimensional Swift-Hohenberg system in [2].

Furthermore, it is not clear that a local analysis of individual u_n (n fixed) near $\mu = 0$ or $\mu = 1$ is sufficient for persistence in this case; more investigation will be needed. This is one potential motivation for the following objective.

Proposed Problem 4. *Analysis beyond the anticontinuum limit.* While Objectives 1, 2, and 3 all focus on analysis in the anticontinuum limit, our ultimate goal is to pursue analysis away from the anticontinuum limit. By starting at the continuum limit and numerically exploring the bifurcation structures that emerge away from this limit, we can make connections between discrete and continuous space localized patterns and highlight the differences between them.

Breaking the symmetry $x \mapsto -x$ leads to drift in models with continuous space; however, this feature is not present in these discrete lattice models. We propose to investigate the "pinning" phenomenon in these lattice models, with the goal of understanding the conditions for the patterns to "de-pin" and begin to move.

7.3 References

[1] N. Akhmediev and A. Ankiewicz, *Dissipative solitons in the complex Ginzburg-Landau and Swift-Hohenberg equations*, Dissipative Solitons, (2005), pp. 17–34.

[2] D. Avitabile, D. J. Lloyd, J. Burke, E. Knobloch, and B. Sandstede, *To snake or not to snake in the planar Swift–Hohenberg equation*, SIAM J. Appl. Dyn. Syst., 9 (2010), pp. 704–733.

[3] O. Batiste and E. Knobloch, *Simulations of localized states of stationary convection in He 3- He 4 mixtures*, Phys. Rev. Lett., 95 (2005), p. 244501.

[4] M. Beck, J. Knobloch, D. J. Lloyd, B. Sandstede, and T. Wagenknecht, *Snakes, ladders, and isolas of localized patterns*, SIAM J. Math. Anal., 41 (2009), pp. 936–972.

[5] J. Burke and E. Knobloch, *Localized states in the generalized Swift-Hohenberg equation*, Phys. Rev. E, 73 (2006), p. 056211.

[6] J. H. Dawes, *The emergence of a coherent structure for coherent structures: Localized states in nonlinear systems*, Philos. Trans. R. Soc. Lond. Ser. A Math. Phys. Eng. Sci., 368 (2010), pp. 3519–3534.

[7] N. H. Fefferman and K. L. Ng, *The role of individual choice in the evolution of social complexity*, in Ann. Zool. Fennici, JSTOR, 2007, pp. 58–69.

[8] A. P. Galvani and R. M. May, *Epidemiology: Dimensions of superspreading*, Nature, 438 (2005), pp. 293–295.

[9] A. Hoffman and J. Mallet-Paret, *Universality of crystallographic pinning*, J. Dynam. Differential Equations, 22 (2010), pp. 79–119.

[10] G. W. Hunt, M. A. Peletier, A. R. Champneys, P. D. Woods, M. A. Wadee, C. J. Budd, and G. Lord, *Cellular buckling in long structures*, Nonlinear Dynam., 21 (2000), pp. 3–29.

[11] W. Kermack and A. McKendrick, *A contribution to the mathematical theory of epidemics*, Proc. R. Soc. Lond. Ser. A Math. Phys. Eng. Sci., (1927), pp. 700–721.

[12] E. Knobloch, *Spatially localized structures in dissipative systems: Open problems*, Nonlinearity, 21 (2008), p. T45.

[13] J. Knobloch, *Lin's method for discrete dynamical systems*, J. Difference Equ. Appl., 6 (2000), pp. 577–623.

[14] S. Koga and Y. Kuramoto, *Localized patterns in reaction-diffusion systems*, Progr. Theoret. Phys., 63 (1980), pp. 106–121.

[15] D. J. Lloyd, B. Sandstede, D. Avitabile, and A. R. Champneys, *Localized hexagon patterns of the planar Swift–Hohenberg equation*, SIAM J. Appl. Dyn. Syst., 7 (2008), pp. 1049–1100.

[16] J. O. Lloyd-Smith, S. J. Schreiber, P. E. Kopp, and W. M. Getz, *Superspreading and the effect of individual variation on disease emergence*, Nature, 438 (2005), pp. 355–359.

[17] R. Richter and I. Barashenkov, *Two-dimensional solitons on the surface of magnetic fluids*, Phys. Rev. Lett., 94 (2005), p. 184503.

[18] C. Taylor and J. H. Dawes, *Snaking and isolas of localised states in bistable discrete lattices*, Phys. Lett. A, 375 (2010), pp. 14–22.

[19] A. Yulin and A. R. Champneys, *Discrete snaking: Multiple cavity solitons in saturable media*, SIAM J. Appl. Dyn. Syst., 9 (2010), pp. 391–431.

[20] ——, *Snake-to-isola transition and moving solitons via symmetry-breaking in discrete optical cavities*, Discrete Contin. Dyn. Syst., 4 (2011), pp. 1341–1357.